Water splitting through model surfaces of metal oxides : ferroelectric polarization towards water adsorption processes

Pierre-Marie Deleuze

THESE DE DOCTORAT DE L'ETABLISSEMENT UNIVERSITE BOURGOGNE FRANCHE-COMTE PREPAREE AU LABORATOIRE INTERDISCIPLINAIRE CARNOT DE BOURGOGNE

Ecole doctorale n°553
Carnot-Pasteur

Doctorat de Chimie-Physique

Par
Pierre-Marie DELEUZE

Water splitting through model surfaces of metal oxide: ferroelectric polarization towards water adsorption processes

---

Thèse présentée et soutenue à Dijon, le 03/12/2019

M. Jacek Goniakowski	Directeur de recherche, Institut des Nanosciences de Paris	Rapporteur
M. José Penuelas	Maître de conférences HDR, Ecole Centrale de Lyon	Rapporteur
Mme Hélène Magnan	Chercheur, CEA-Saclay	Examinatrice
M. Grégory Geneste	Chercheur, CEA-DAM Ile de France	Examinateur
M. André Nonat	Directeur de recherche, Université de Bourgogne	Examinateur
M. Bruno Domenichini	Professeur, Université de Bourgogne	Directeur de thèse
Mme Céline Dupont	Chargée de recherche, Université de Bourgogne	Co-directrice de thèse

Abstract

The properties of out-of-plane polarized $BaTiO_3$(001) thin films were investigated from first-principles calculations and photoemission spectroscopy. Firstly, density functional theory calculations (DFT) were used to unravel the nature of the Pt(001)/$BaTiO_3$(001) interface. In particular, the influence of the substrate on the ferroelectric properties of the $BaTiO_3$ overlayer has been studied. Among the results, it can be pointed that platinum tends to increase the ferroelectric domain size of $BaTiO_3$.

Then, the adsorption of water on $BaTiO_3$ was described by means of DFT calculations. The impact of the polarization as well as the influence of the nature of the surface termination on water adsorption were studied. Different adsorption processes depending on the chemical nature of the surface termination were evidenced. Additionally, water was shown to switch the polarization towards the upward direction on the TiO_2 termination while the downward polarization is stabilized in the BaO termination.

Finally, time-resolved photoemission spectroscopy was used to measure the charge dynamics of photogenerated electron-hole pairs in both $BaTiO_3$ and Fe_2O_3. Near ambient pressure conditions allowed to record the charge dynamics in hematite while exposed to water, revealing a significant modification of the band bending induced by water adsorption.

Keywords: *water splitting, ferroelectricity, $BaTiO_3$, heterojunction, DFT, TR-PES, NAP-XPS.*

Résumé

Les propriétés de films minces de $BaTiO_3$(001) polarisés hors-plan ont été étudiées à partir de calculs *ab initio* et par spectroscopie de photoélectrons. Tout d'abord, la théorie de la fonctionnelle de la densité (DFT) a été utilisée pour décrire la nature de l'interface Pt(001)/$BaTiO_3$(001). En particulier, l'influence du substrat sur les propriétés ferroélectriques du film de $BaTiO_3$ a été analysée. Parmi les résultats, il a été montré que le platine tend à accroître la taille des domaines ferroélectriques de $BaTiO_3$.

Ensuite, les mécanismes d'adsorption de l'eau sur $BaTiO_3$ ont été décrits par calculs DFT. L'impact de la polarisation ainsi que l'influence de la terminaison de surface sur l'adsorption de l'eau ont été analysés. Il a pu être montré que les processus d'adsorption dépendent directement de la nature de la terminaison. En outre, il a été observé que l'eau peut induire un renversement de la polarisation dont la direction finale dépend de la terminaison. En effet, l'eau stabilise la polarisation orientée vers le haut sur la terminaison TiO_2 alors qu'elle induit une polarisation orientée vers le bas sur la terminaison BaO.

Enfin, la dynamique de création et de recombinaison des charges photogénérées dans $BaTiO_3$ et Fe_2O_3 a été mesurée par spectroscopie de photoelectrons résolue temporellement. Des mesures dans des conditions de pression proches de l'ambiante ont notamment permis de mesurer la dynamique des charges dans l'hématite lorsque celle-ci est exposée à l'eau, révélant une importante modification de la courbure de bandes du fait de l'adsorption d'eau.

Mots-clés : *photo-électrolyse, ferroélectricité, $BaTiO_3$, hétérojonction, DFT, TR-PES, NAP-XPS.*

Remerciements

Tout d'abord, je remercie sincèrement mes directeurs de thèse Bruno DOMENICHINI et Céline DUPONT pour leur encadrement, leur bienveillance et leur soutien tout au long de ces 3 années. Je vous remercie tous les deux de m'avoir fait confiance dès le début et d'avoir toujours fait en sorte que cette thèse se passe dans les meilleures conditions. Merci à Céline d'avoir réussi à rendre l'apprentissage de la DFT agréable et merci à Bruno pour son optimisme à toute épreuve.

Je tiens à remercier M. Jacek GONIAKOWSKI et M. José PENUELAS pour avoir accepté de rapporter ces travaux de thèse ainsi que Mme Hélène MAGNAN, M. Grégory GENESTE et M. André NONAT pour avoir accepté de faire partie de mon jury de thèse.

Je remercie également chaleureusement les membres de l'équipe SIOM : Valérie, Sylvie, Carmen, Luc et Mike ainsi que nos voisins du rez-de-chaussée, « les ciments » : Sandrine, André, Christophe et Isabelle. Merci pour tous ces bons moments passés dans la salle café et les bonnes rigolades (bon courage à Céline pour continuer à supporter les blagues pourries).

J'ai également une grande pensée pour Agnès, notre gestionnaire, qui nous rend à tous la vie beaucoup plus facile au quotidien et sans qui rien ne serait possible !

Je remercie aussi les parisiens du projet PHOTO-POT avec qui j'ai pu travailler : Hélène, Antoine, Patrick, Mathieu, Julien et Dana. Merci en particulier aux synchrotronistes de m'avoir fait apprécier cet environnement si particulier et pour ces longues discussions en tout genre pendant les runs synchrotrons (et à Antoine pour les gâteaux !).

Une thèse ne serait pas complète sans les rencontres et échanges avec les autres doctorants et post-doc. Je remercie donc toutes les personnes avec qui j'ai pu partager mon bureau : Abdel, Agnes, Houssem et plus récemment Moad, bon courage pour la suite. Bien sûr, je remercie aussi grandement les jeunes qui m'accompagnaient déjà en licence et qui ont réellement permis à cette thèse de se passer dans la bonne humeur. Merci à Bolso (ça fait plus de 8 ans déjà !) de nous avoir tous fait marrer pendant toutes ces années, et bonne chance à toi pour ta soutenance. Merci à Pierre, entre autres, de m'avoir fait suivre la NBA et bon courage à toi pour la fin de ta thèse. Merci aussi à David pour toutes ces discussions et bonne chance à Laëtitia et toi à Denver.

Je remercie également Nicolas et Ludo, anciens doctorant et post-doc de l'équipe, pour m'avoir permis de décompresser autour d'une bière ou sur le vélo. D'ailleurs merci à vous et à Bruno de m'avoir fait me remettre au vélo pour compenser tous les desserts qui sont

régulièrement consommés au rez-de-chaussée. J'espère pour vous que les futurs thésards et stagiaires feront perdurer cette tradition !

Pour finir, j'ai bien entendu une pensée plus particulière pour Estelle qui est devenue tellement plus qu'une collègue de bureau. Je te remercie vraiment de m'avoir toujours soutenu et supporté même dans les moments de doute.

Contents

General introduction

The continuous increase of the global energy consumption is a major concern in today's society. From 13 TW in 2001 to 16 TW today, the world annual energy consumption is expected to grow to *ca.* 30 TW in 2050 if nothing is done to diminish this massive extension [1, 2]. Among this power, 87% is based on fossil fuel burning. This high share is one of the main reasons of the global climate change because of the greenhouse effect. It thus appears essential to develop alternative energy sources with low carbon emissions. Different approaches have been considered over the years. One could cite the use of biomass, wind or hydroelectricity. However the most promising renewable energy source is probably the solar energy. Indeed, the amount of solar radiation reaching the Earth is expected to be more than three orders of magnitude higher than the annual global energy use [3, 4]. According to these assessments, the world annual energy demands could be met in one hour by the sun light. Yet, the discrepancy of energy needs along the year as well as the intermittence of sunlight requires the use of solar energy storage devices to match supply with demand.

Hydrogen is the most abundant element in the universe but does not exist in the form of H_2 on Earth, but rather mainly in the form of H_2O. H_2 has highly combustible properties which make it a promising energy vector, for instance in fuel cells, which use hydrogen as a clean fuel and release water as by-product, with no greenhouse gas emissions [5]. The scalability of fuel cells makes them suitable for a wide range of applications from laptops or small electronic devices (10-100 W) to power plants (1-200 MW). However, it is necessary to make further developments to decrease their costs, as well as their durability and sustainability.

Nowadays about 96% of hydrogen is produced from fossil fuels as 48% is made from methane steam reforming, 30% from liquid hydrocarbons reforming and 18% from coal gasification [6]. Methane steam reforming is the most common hydrogen production method because it is a proven industrial process and is very affordable (around 1 \$/kg of H_2) [7]. Nevertheless, this process is not compatible with the low greenhouse gas emissions required to keep global warming below 2°C as 2.5 tons of CO_2 are released to produce one ton of H_2 [8, 9]. Among the clean possible solutions to produce hydrogen, the most developed is water electrolysis, where electricity is used to split water into hydrogen and oxygen. Although water electrolysis is a convenient way to produce hydrogen, it requires four times more energy input than natural gas processes [10]. As a matter of fact, if non renewable energies are used to generate the electricity in water electrolysis, it could result in higher emissions than hydrogen produced through natural gas reforming. It is thus clear that electrolysis based technologies are only sustainable if the electricity used in the process is produced from a carbon-free source. Therefore, a clever way to produce hydrogen through water splitting would be with the use of solar energy as an electricity source. In this spirit, the combination

of photovoltaics and water electrolysis could be an efficient solution as both technologies are mature. However, taking a high efficiency solar cell with a conversion of 25% coupled with an electrolyzer with an efficiency of 85% would only lead to a maximum solar to hydrogen conversion of 21%. Additionally, the generation of intermediates, electricity in this case, inevitably leads to significant energy losses which in turn increases the global cost. Ultimately, these kind of devices have an estimated production cost of 10 \$/kg H_2 [7].

To avoid this issue, a more elegant and potentially efficient way is to convert directly solar energy into hydrogen. This can be done through water photoelectrolysis which uses the photovoltaic effect of semiconductors to absorb photons in order to generate charge carriers to promote the oxido-reduction reaction of water. This is an old idea because such a reaction was first demonstrated by Fujishima and Honda in 1972 where they used TiO_2 as a photoactive catalyst [11].

In this work, we propose to study photoanodes for the photooxidation of water. In particular, we will investigate the ability of ferroelectric materials to display a spontaneous polarization to possibly enhance the reactivity of the photoanode. Indeed, photocatalytic water splitting usually requires the application of an electric bias which could be decreased by the spontaneous electric field inside the ferroelectric material. In this thesis, our approach is to try to combine theoretical results and experimental measurements carried out on single crystalline thin films in order to better understand the role of ferroelectricity in reaction processes, especially the step of water adsorption. Additionally, some results of charge carrier dynamics under close to realistic conditions are presented on hematite, *i.e.* a photocatalyst more suitable to visible light absorption which could be assembled with a ferroelectric to improve its reactivity.

This thesis is divided in six chapters. Chapter 1 gives an introduction to photocatalytic water splitting and in particular the advantages provided by the use of ferroelectric materials through the internal electric polarization. Chapter 2 details the theoretical and experimental techniques used to study the thin films. A particular emphasis is given to the method used to model the out-of-plane polarized surfaces without using electrodes or artificial electric field to screen the depolarizing field. Chapter 3 is mainly dedicated to the theoretical characterization of the $Pt/BaTiO_3$ interface and presents especially the polarization behavior in such interfaces. Chapter 4 exposes both theoretical and experimental results of water adsorption on $BaTiO_3$ by means of Density Functional Theory calculations and synchrotron characterization techniques. In chapter 5, we discuss the charge carrier dynamics in $BaTiO_3$ thin films and in Fe_2O_3, in particular during water adsorption. Finally, chapter 6 gives a general conclusion and provides new perspectives.

Chapter 1

State of the art

1.1 Solar water splitting

Water splitting is an oxido-reduction reaction where water molecules are oxidized into O_2 and reduced in H_2 following:

$$H_2O \rightarrow H_2 + \frac{1}{2}\ O_2 \tag{1.1}$$

It corresponds to the sum of two half reactions: the oxidation of the O_2/OH^- couple as (in basic media):

$$2\ OH^- \rightarrow H_2O + \frac{1}{2}\ O_2 + 2e^- \tag{1.2}$$

and the reduction of the H_2O/H_2 couple:

$$2\ H_2O + 2e^- \rightarrow 2\ OH^- + H_2 \tag{1.3}$$

Water splitting is an endothermic reaction with a Gibbs free energy of $\Delta_r G^0 = 237.2$ kJ.mol^{-1}, which corresponds to an electrochemical potential of 1.23 V [12]. Therefore, energy has to be supplied to the system for the reaction to happen. In the scope of photocatalytic water splitting, this energy is provided to a semiconductor by solar energy through the creation of electron-hole pairs. Indeed, the absorption of photons leads to the promotion of an electron from the valence band to the conduction band, leaving a hole (positive charge carrier) in the valence band. Holes can react at the semiconductor/electrolyte interface with hydroxyl ions to form oxygen while the electrons are transferred to the cathode where they can reduce water into hydrogen (see equations 1.2 and 1.3).

The reaction system, called photoelectrochemical cell (PEC), can be described as follow: two electrodes where the water oxidation and reduction occur are immerged in an aqueous solution (electrolyte). The electrode where the reduction takes place is referred to as cathode

while the other electrode where water is oxidized is named anode. There are several possible configurations to perform direct water splitting using photoelectrodes. Devices where the oxidation and reduction processes take place on a single electrode have been reported. For instance, a single semiconductor can be used to directly split water. Domen *et al.* reported the use of nanoparticles of a solid solution of gallium and zinc nitrogen oxide to split water with an efficiency of 2.5% at a wavelength of 420-440 nm [13]. Additionally, work has been done to develop an electrode where water oxidation takes place on one side of the electrode while the reduction reaction is performed on the other side. An example is the wireless electrode presented by Nocera *et al.* consisting of a triple junction silicon solar cell interfaced to two catalysts for hydrogen and oxygen production [14]. They reported a solar to hydrogen efficiency of 2.5%. However, these types of single electrodes yield several problems. Indeed, the electrode has to be efficient for both water oxidation and reduction which increases the complexity of the system and thus the price. Secondly, in such architectures, the production of oxygen and hydrogen are not physically separated. Consequently, an additional step is required to separate both gases which subsequently increases the energy cost and decreases the efficiency on top of representing a safety issue.

In order to spatially separate the water oxidation and reduction, the electrons generated at the anode can be conveyed through an ohmic contact to the cathode. The first demonstration of a working PEC by Fujishima and Honda actually used this design with a n-type photoanode connected to a Pt wire as a cathode [11]. However, since two electrodes are necessary, one can imagine replacing the metal wire by a light-absorbing photocathode. In this case, the holes produced by the photoanode oxidize water while the electrons produced by the photocathode reduce it. Several approaches have been presented in this manner. One can cite, for example, the pioneer work of Yoneyama [15] on p-type photocathodes composed of GaP or the work of Sivula *et al.* who demonstrated a working PEC composed of a $BiVO_4$ photoanode and a Cu_2O photocathode [16]. More detailed reviews on these so-called tandem cells have been written by Prévot *et al.* [17], Ager *et al.* [18] or Zhang *et al.* [19].

For the water splitting reaction to take place, both valence band and conduction band of the semiconductor need to straddle the redox potentials of water. In other words, the valence band needs to be at a more positive potential than the oxidation potential of water while the conduction band has to be at a more negative potential than the reduction potential of water. Often, an external bias should be applied in order to drive the half reactions due to insufficient overpotential in the materials. This extra input of energy can be provided through a generator or a solar cell mounted in the external circuit or directly joined with the photoelectrodes. Additionally, the use of an internal electric field directly inside the photoelectrode, using ferroelectric materials for instance, has gained a lot of attention in the past years. This particular aspect will be detailed later. In the following, we will focus on

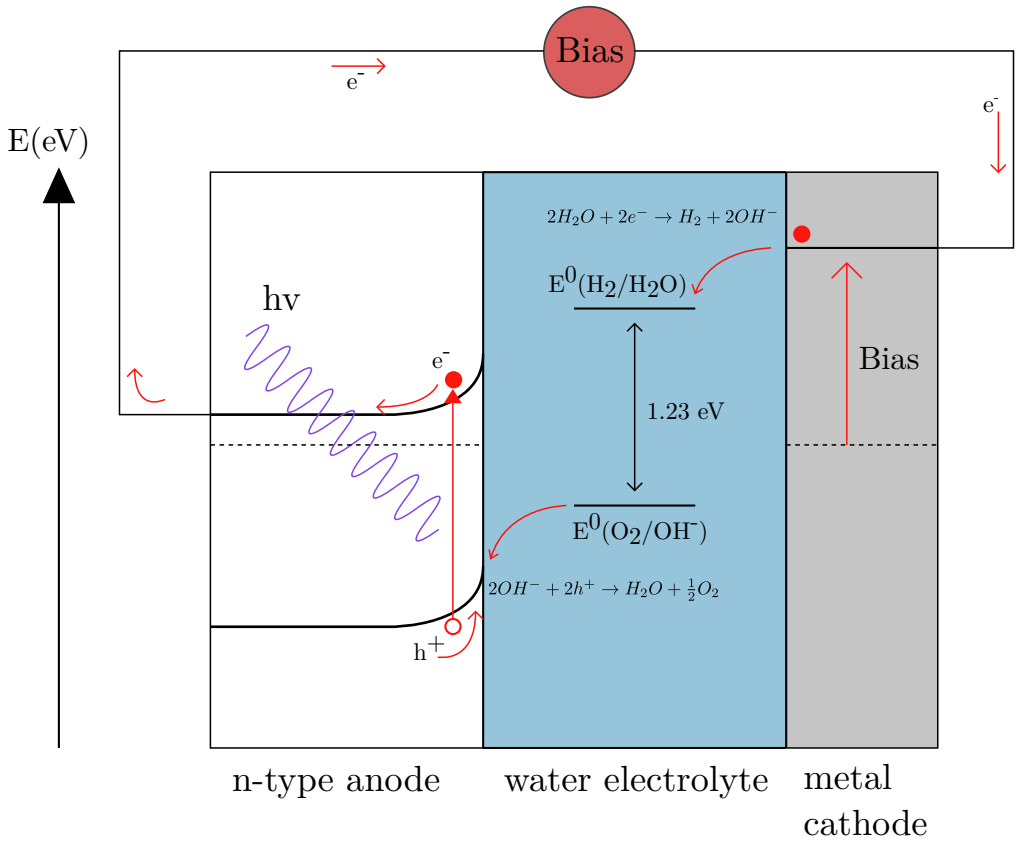

Figure 1.1 – Schematic representation of a solar water splitting system using a photoanode, a metallic cathode and an external anodic bias to assist water oxido-reduction.

systems where the water reduction is realized using a metallic cathode. A representation of such systems can be seen on Figure 1.1. The different steps of the water splitting can be described as follow: (1) a photon is absorbed by the photoanode generating an electron-hole pair in the material, (2) the hole diffuses towards the interface with the electrolyte and (3) oxidizes water into oxygen, (4) the electron is transported to the back-side of the electrode and through the external circuit to the cathode, (5) the electron reduces water in hydrogen at the metallic cathode.

Different parameters will influence the efficiency of the overall reaction, namely: the light absorption (step 1), the charge transport (steps 2 and 4) and the reaction kinetics (steps 3 and 5). The latter can be optimized by depositing a catalyst on the surface and is thus not a limiting parameter for the choice of a semiconductor. On the other hand, the other parameters are intrinsic properties of the material and will be discussed. In the following section, the physics when the semiconductor is brought in contact with the electrolyte is presented.

1.2 Band diagrams

While for an isolated atom electrons occupy discrete energy states, solids develop what is called a band structure. This is due to the Pauli's exclusion principle which prevents two electrons from having the same energy state. Therefore, if two atoms bind together, the energy level splits into two discrete energy levels to satisfy Pauli's exclusion principle. This phenomenon is represented on Figure 1.2. It is understandable that when the number of atoms continues to increase, the energy levels become closer and closer. Consequently, for a large enough number of atoms the resulting orbitals are so close in energy that they form a continuous energy band. It results in a band structure where energy bands accessible to the electrons are separated from each other by a forbidden band, so-called a band gap (E_g). The highest occupied band is referred to as the valence band while the lowest unoccupied band is called the conduction band. The number of electrons that each band can contain is equal to $N \times 2(l+1)$ where N is the number of atoms in the system and l is the azimuthal quantum number of the atomic orbitals forming the band. The conductive or insulative character of a material is directly related to the filling of the bands. If a band is partially filled, the electrons are allowed to freely move inside the band, resulting in a conductive material. This can arise from an overlap between the valence and conduction bands (see Figure 1.3(b)) or an odd number of valence electrons (see Figure 1.3(a)). If the valence electrons fully fill the bands then the crystal will be an insulator (Figure 1.3(d)). In this case, the band gap is too wide for an electron to freely move to the conduction band (usually more than 5 eV). Now, if the band gap is smaller, typically between 0.5 and 4 eV, electrons may be promoted from the valence band to the conduction band, provided that the material is excited with an energy higher than E_g (Figure 1.3(c)).

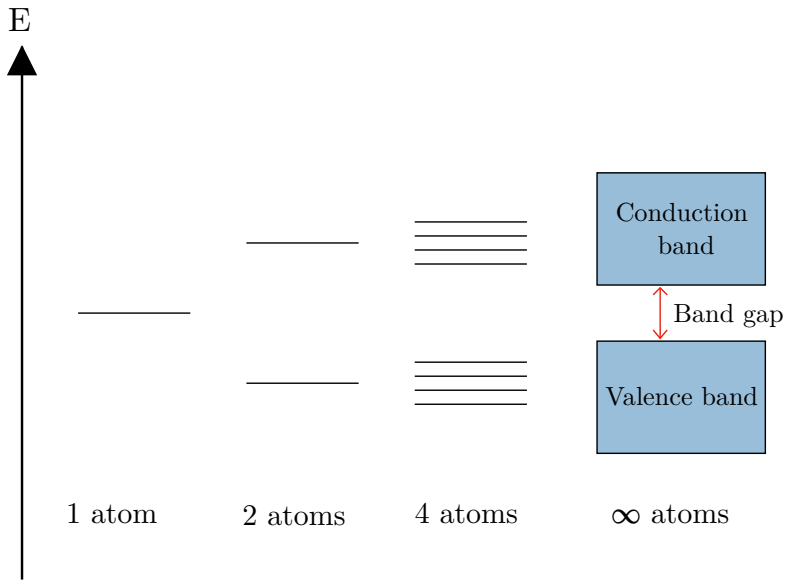

Figure 1.2 – Electronic energy level splitting resulting of atoms bonding.

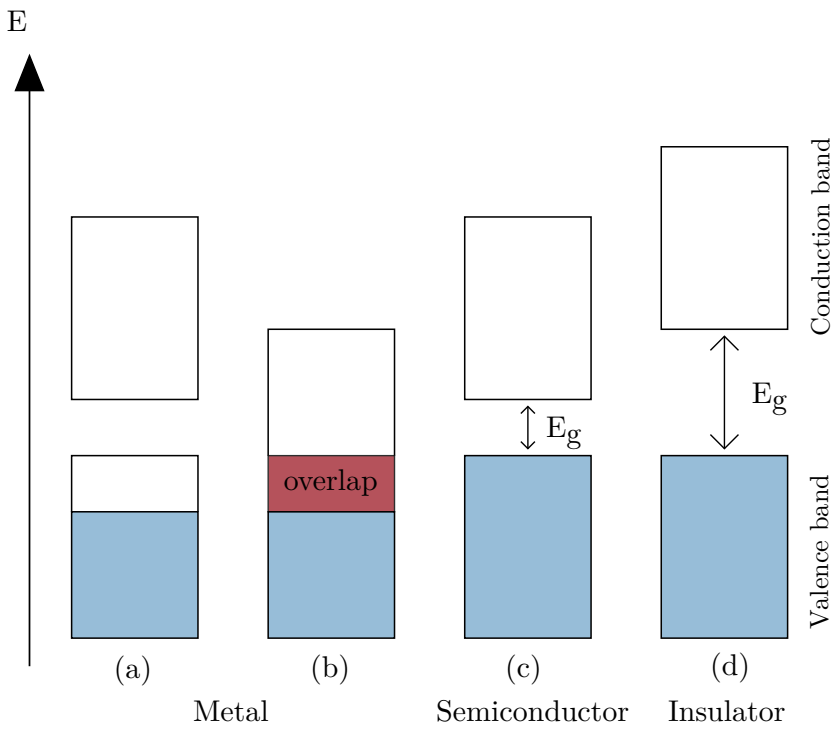

Figure 1.3 – Schematic representation of the band diagrams for (a) a metal with its highest occupied band partially filled, (b) a metal or semimetal because of band overlap, (c) a semiconductor with a small band gap allowing electron excitation to the conduction band and (d) an insulator with a large band gap. The electron filling is represented in blue.

1.2.1 Intrinsic semiconductors

The Fermi level (E_F) corresponds to the energy level where the probability to find an electron is 0.5, and, in solids, it represents the chemical potential of the electrons. It is located in the valence band for metals and in the forbidden gap in the case of semiconductors or insulators. The concentration of electrons in the conduction band (denoted n) is given by [20]:

$$n = \int_{E_C}^{\infty} N(E) f(E) \mathrm{d}E \tag{1.4}$$

where E_C is the conduction band edge, $N(E)$ is the density of states at the energy E and $f(E)$ is the probability to find an electron of energy E. $f(E)$ follows a Fermi-Dirac distribution as:

$$f(E) = \frac{1}{1 + e^{\frac{E-E_F}{k_B T}}} \approx e^{-\frac{E-E_F}{k_B T}} \tag{1.5}$$

where E_F is the Fermi level, k_B the Boltzmann constant and T the temperature. At the temperatures of interest, it can be supposed that $E - E_F \gg k_B T$, so that equation 1.5 can

be simplified as shown. This leads to:

$$n = N_C \; e^{-\frac{E_C - E_F}{k_B T}} \tag{1.6}$$

where N_C is the effective density of states in the conduction band. Similarly, the hole density near the top of the valence band (noted p) can be obtained through the same reasoning:

$$p = \int_{-\infty}^{E_V} N(E)(1 - f(E))\mathrm{d}E \tag{1.7}$$

and considering the same approximations:

$$p = N_V \; e^{-\frac{E_F - E_V}{k_B T}} \tag{1.8}$$

where N_V is the effective density of states in the valence band. The combination of equations 1.6 and 1.8 can lead to the determination of the Fermi level position if n and p are known as:

$$E_F = E_c - k_B T \; ln\left(\frac{N_C}{n}\right) = E_V + k_B T \; ln\left(\frac{N_V}{p}\right) \tag{1.9}$$

As in an intrinsic semiconductor, in order to conserve charge neutrality, the electronic density must be equal to the hole density ($n = p = n_i$), equation 1.9 leads to:

$$E_F = \frac{E_C + E_V}{2} + \frac{k_B T}{2} \; ln\left(\frac{N_V}{N_C}\right) \tag{1.10}$$

This means that the Fermi level is close to the middle of the band gap as, at room temperature, $k_B T \approx 26$ meV which is negligible compared to the usual band gap values (typically above 1 eV). Finally, the intrinsic carrier density can be obtained according to:

$$np = N_C N_V \; e^{-\frac{E_g}{k_B T}} = n_i^2 \tag{1.11}$$

1.2.2 Doped semiconductors

Impurities can be added to an intrinsic semiconductor which can widely affect its electrical properties. When the addition is deliberate, the process is called doping. If the dopants present an excess of electrons compared to the lattice, they are called donors and create a n-type doping of the semiconductor. On the other hand, dopants presenting a deficit of electrons compared to the lattice are named acceptors because they accept electrons from the valence band to complete the covalent bonds with neighbor atoms, generating holes in the valence band. These dopants induce a p-type doping of the semiconductor. The ionization energy of the dopant is also an important parameter. It should be comparable to $k_B T$ so that thermal agitation promotes the ionization of the dopant at room temperature. Therefore, a donor level should be a few $k_B T$ below the conduction band while an acceptor level should be

a few k_BT above the valence band. Figure 1.4 shows a schematic band diagram and the Fermi level position as a function of the doping. For a n-type semiconductor, an electron donor with an energy level close to the conduction band can promote electrons into the conduction band. For a concentration N_D of donors in the lattice, and if all dopants are ionized at room temperature, the electron density in the conduction band is:

$$n = n_i + N_D \tag{1.12}$$

which, for large doping amounts, can be approximated to $n = N_D$. Therefore, the Fermi level position can be obtained from equation 1.9:

$$E_F = E_C - k_BT\ ln\left(\frac{N_C}{N_D}\right) \tag{1.13}$$

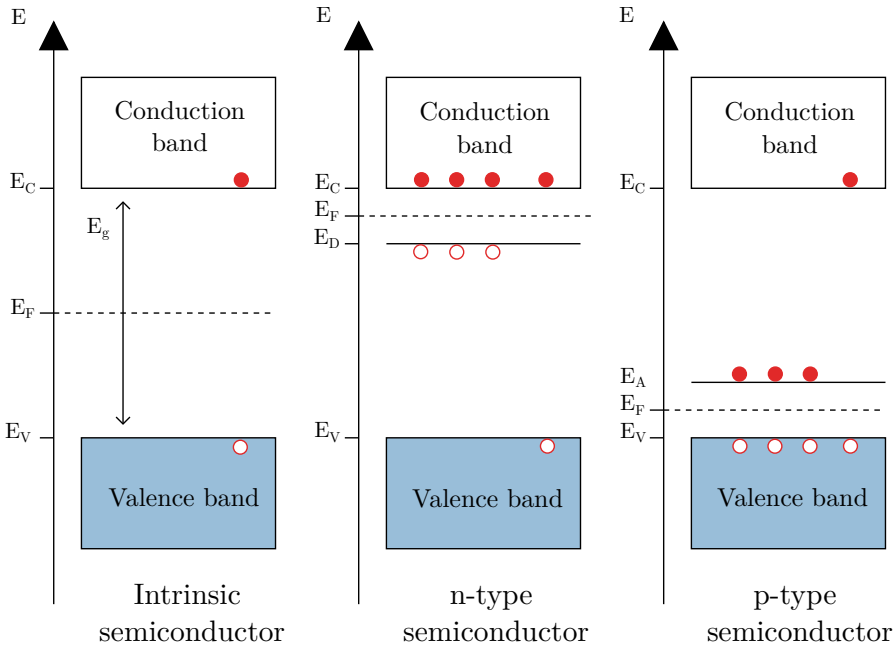

Figure 1.4 – Band diagram representation of an intrinsic, n-type and p-type semiconductor at thermal equilibrium. The dopants levels are represented after ionization. The plain red circles represent the electrons while the hollow circles show the holes. E_D and E_A stand for the donor energy level and the acceptor energy level, respectively.

Likewise, for p-type semiconductors with an acceptor energy level close to the valence band, the ionization of the dopant allows the promotion of electrons from the valence band to the acceptor level, leaving holes in the valence band. For a concentration of acceptors N_A, it leads to:

$$p = p_i + N_A \approx N_A \tag{1.14}$$

$$E_F = E_V + k_B T \; ln\left(\frac{N_V}{N_A}\right) \tag{1.15}$$

Finally, it is worth noting that, although in an intrinsic undoped semiconductor the concentrations of electrons and holes are equal, in a doped semiconductor a discrepancy between both charge carriers arises. Indeed, in a n-type semiconductor, electrons are the majority charge carriers while holes are the minority charge carriers as the electron concentration is higher than the hole concentration. The behavior is reversed in a p-type semiconductor where the holes are the majority charge carriers.

1.2.3 The semiconductor/electrolyte contact

In electrolytes, the equivalent of the Fermi level in solids is the electrochemical potential (labelled E_{redox}). When a semiconductor is brought in contact with an electrolyte, an equilibrium of the chemical potentials in both components is reached by charge transfer at the interface. The majority charge carriers are transferred from the semiconductor to the electrolyte until $E_F = E_{redox}$ which results in the depletion in a certain thickness of the material, called space charge layer. In a n-type semiconductor, electrons flow from the semiconductor surface to the electrolyte resulting in a depletion layer positively charged. This depletion creates a positive potential at the interface with the liquid, which bends the bands upward. This phenomenon is shown on Figure 1.5. Meanwhile, this depletion layer in the semiconductor is screened in the electrolyte by a charged layer of opposite sign called the Helmholtz layer. It consists of a continuous layer of ions (anions in the case of n-type semiconductors) present in the liquid to counter the positive charges at the surface of the semiconductor. Because of the electric field induced in the depletion layer, the electrons in the space charge layer flow towards the bulk of the semiconductor while the holes move towards the semiconductor/electrolyte interface [21]. This behavior means that n-type semiconductors are particularly suited for a photoanode as the water oxidation reaction involves holes to oxidize water. Similarly, p-type semiconductors promote electron transfer to the electrolyte because of a downward band bending, making them good candidates for photocathodes.

It is possible to calculate the potential profile $V(x)$ as a function of the distance from the surface x. In a n-type semiconductor, the volumetric charge density is approximately equal to eN_D. If $x = 0$ at the surface and $x = \infty$ in the bulk and $V(\infty) = 0$, Poisson's equation can be solved assuming that $k_B T$ is negligible compared to the potential drop in the depletion layer:

$$V(x) = -\frac{eN_D}{2\varepsilon_r \varepsilon_0}(x - W_{SC})^2 \tag{1.16}$$

where e is the elementary charge, ε_r is the relative dielectric constant of the semiconductor, ε_0

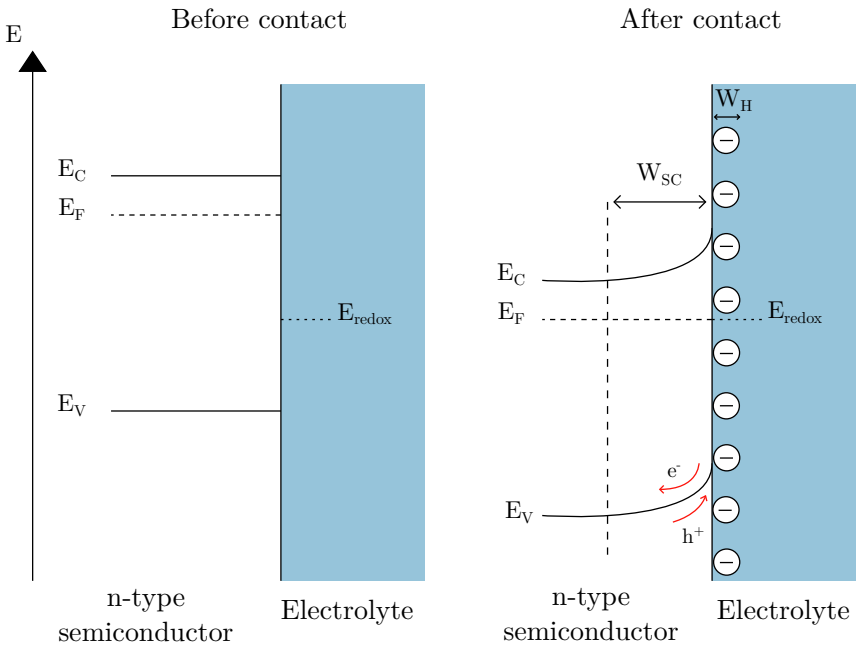

Figure 1.5 – Band diagram representation of a n-type semiconductor before its contact with an electrolyte (left) and after the contact with an electrolyte with a chemical potential E_{redox} (right). W_{SC} and W_H are the width of the space charge layer and of the Helmholtz layer, respectively. The layer of anions balancing the depletion layer are represented in minus circles.

is the vacuum permittivity and W_{SC} is the space charge layer thickness. Under the depletion region approximation, the thickness of the space charge layer is given by [22, 23]:

$$W_{SC} = \sqrt{\frac{2\varepsilon_r\varepsilon_0|V - V_{fb}|}{eN_D}} \tag{1.17}$$

where V_{fb} is the flat band potential corresponding to the potential for which bands are unbent.

When a potential V_{bias} is applied on the semiconductor the band bending is modified. It is usual to call a positive applied potential that decreases E_F compared to E_{redox} an anodic potential while a negative potential that increases E_F with respect to E_{redox} is referred to as a cathodic potential. Figure 1.6 depicts the effects of the applied bias on the band bending. It shows that the application of an anodic (positive) bias induces a decrease of the Fermi level relative to E_{redox}. This leads to an increase of the band bending and an extension of the space charge region which reinforces the electron depletion. The opposite is observed in the case of a cathodic bias as the band bending is decreased.

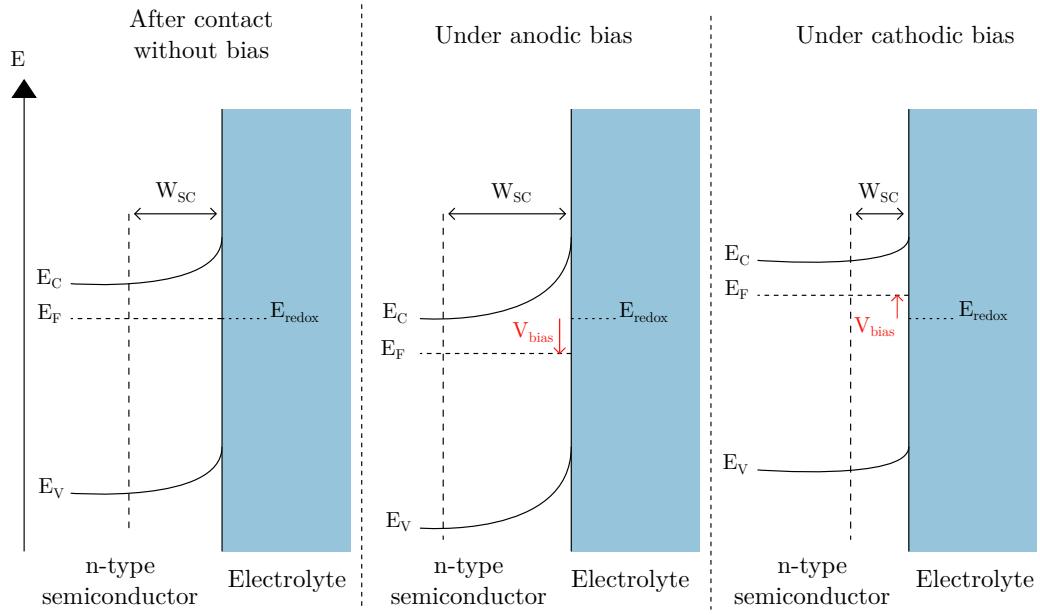

Figure 1.6 – Band diagram of a n-type semiconductor after contact with an electrolyte with a chemical potential E_{redox} with no bias applied (left), with the application of an anodic bias (middle) and with the application of a cathodic bias (right).

Upon illumination, the semiconductor can absorb photons with an energy higher than E_g, leading to the creation of electron-hole pairs. These pairs arise from the promotion of an electron to an energy state in the conduction band, leaving a hole (electron vacancy) in the valence band. If no electric field is present to force the spatial separation of both charge carriers, they will recombine instantaneously. Therefore, it can be considered that any electron-hole pair created outside of the space charge region will recombine immediately. However, illumination can widely modify the band bending as the electron and hole density will increase as a consequence of light absorption, called n^* and p^* respectively. Upon illumination, the system reaches a different steady state and the Fermi level is no longer equal for electrons and holes. It results in the appearance of two quasi Fermi levels for the electrons $E_{F,n}$ and the holes $E_{F,p}$. Their position is given by [21]:

$$E_{F,n} = E_F + k_B T \; ln\left(\frac{n_i + N_D + n^*}{n_i}\right) \approx E_F + k_B T \; ln\left(\frac{N_D}{n_i}\right) \tag{1.18}$$

$$E_{f,p} = E_F - k_B T \; ln\left(\frac{p_i + N_A + p^*}{n_i}\right) \approx E_F - k_B T \; ln\left(\frac{p_i + p^*}{n_i}\right) \tag{1.19}$$

In a n-type semiconductor, the major carrier concentration does not significantly increase under illumination. Thus, the quasi Fermi level of electrons only barely increases compared to its position in the dark. Oppositely, the concentration of holes significantly increases which results in a large decrease of the quasi Fermi level of holes. As shown on Figure 1.7, a reduction of the band bending is induced by the hole transport to the surface which decreases the negative surface charge [24]. The band bending reduction corresponds to the photovoltage V_{ph} and is given by the energy difference between the quasi Fermi level of electrons and the redox potential of the electrolyte E_{redox}. It is worth mentioning that the quasi Fermi level of holes is an important parameter in a material where holes are the reacting charge carrier (such as photoanodes) as it corresponds roughly to the oxidizing power of holes [22]. In Figure 1.7, E_{CL} indicates a core level energy. One can see that the core level follows the same band bending than the valence and conduction bands. Therefore, by measuring the binding energy shift of the core level upon illumination, one can probe its band bending and thus determine the photogenerated charge carrier dynamics using a method such as time resolved photoemission spectroscopy as presented in section 2.2.3.

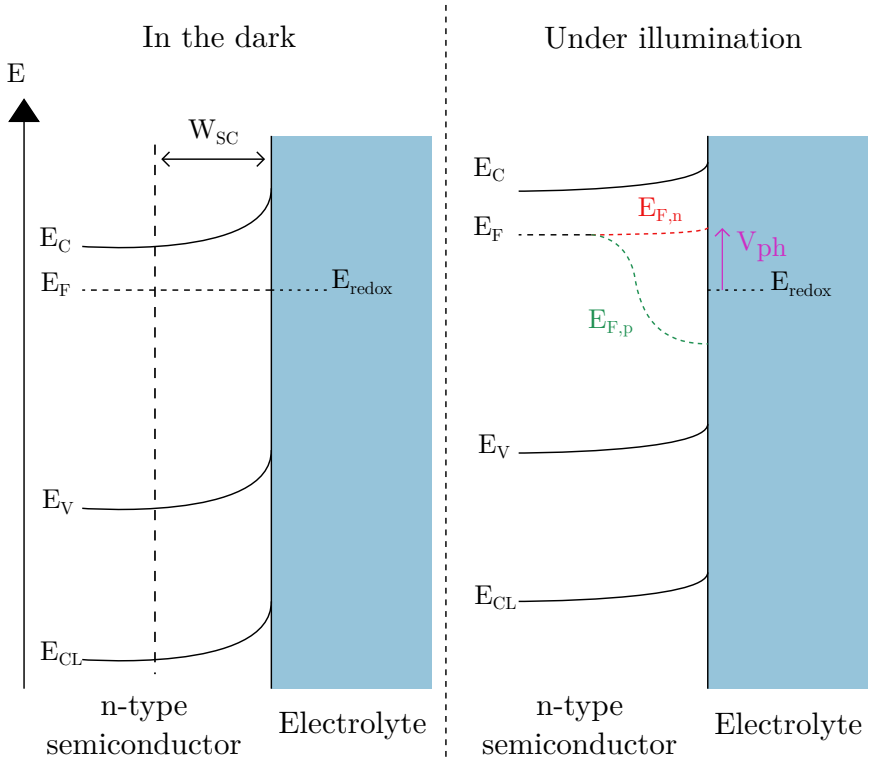

Figure 1.7 – Band diagram of a n-type semiconductor in contact with an electrolyte of chemical potential E_{redox} in the dark (left) and upon illumination (right).

1.3 Choice of the semiconductor

Several parameters have to be taken into account for the determination of a potential candidate as a photoanode for solar water splitting. As mentioned earlier, in order to be competitive against hydrogen production methods used nowadays, solar water splitting has to be competitive from an economical point of view. Therefore, the material should be inexpensive as well as being abundant to meet the requirements of sustainable development. Additionally, the stability of the anode in aqueous environment in oxidation conditions is also of primary importance. Most non-oxide semiconductors may either dissolve or form an oxide layer at their surface which dramatically limits the charge transfer to the electrolyte [12]. For example, it is well known that a Si surface will immediately oxidize to create an insulating SiO_2 layer. Oppositely, metal oxides usually present a good stability in aqueous solutions under oxidative conditions. TiO_2 and Fe_2O_3 are some of the most studied oxides for solar water splitting because they are very stable [25]. Metal oxides are usually low cost, abundant, environmentally friendly and exhibit a good stability in aqueous solutions, so they fulfill these first requirements.

The next primordial criterium is the position of the band edges relative to the oxidation and reduction potentials of water. In the case of a photoanode, water oxidation is driven by the hole transfer from the anode to the electrolyte which is thermodynamically favorable only if the quasi Fermi level of holes is below the energy level of $E^0_{O_2/OH^-}$. Therefore, the top of the valence band E_V should be below the energy level of $E^0_{O_2/OH^-}$. It is also necessary to take into account the kinetic overpotentials which are estimated to *ca.* 0.4 eV for water oxidation and *ca.* 0.05-0.2 eV for water reduction [26–28]. Consequently, for a photoanode the valence band edge should be located well below the oxidation potential of water.

When a metallic cathode is used as a counter electrode, the reduction of water will only occur if the electron energy is higher than the reduction potential of water $E^0_{H_2/H_2O}$. This usually requires the application of an external anodic bias by means of a solar cell or a generator. The anodic bias results in the lowering of the semiconductor Fermi level while the Fermi level of the cathode is increased. Eventually, with a high enough potential, the Fermi level of the cathode will be above the reduction potential of water, activating the reaction. As discussed previously, the metallic cathode could be replaced by a photocathode with its conduction band edge higher than $E^0_{H_2/H_2O}$.

Figure 1.8 shows the valence band and conduction band edges of different semiconductors. Their valence band edge is located well below the O_2/OH^- energy level which indicates that they would favor the water oxidation reaction, thus making them good candidates for photoanodes. Additionally, metal oxides are usually n-type semiconductors due to some oxy-

gen deficiency behaving as electron donors. Some materials like TiO_2 or $SrTiO_3$ also have their conduction band above the O_2/OH^- energy level, implying that they could be used as photocathode as well. Yet, their wide band gap prevents them from absorbing a large portion of the solar spectrum.

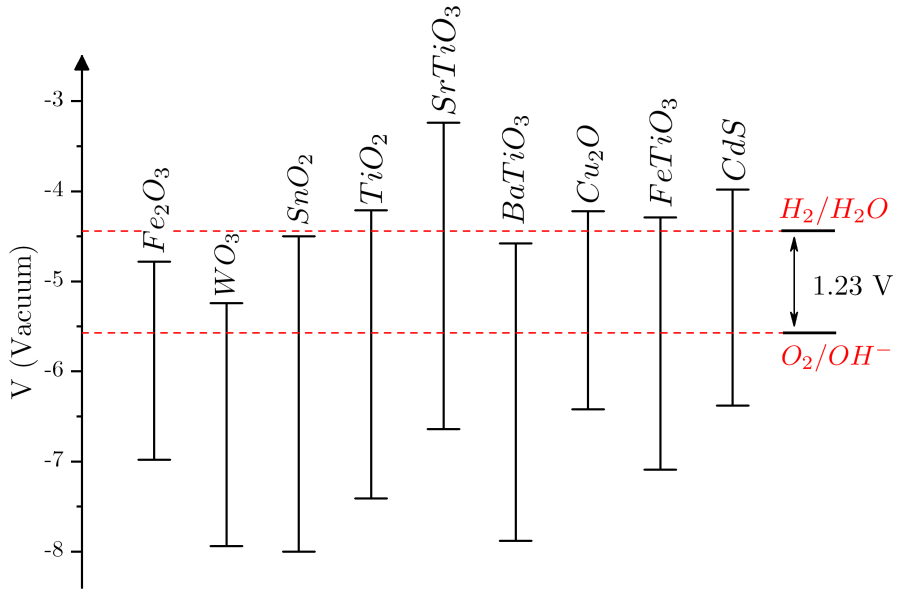

Figure 1.8 – Valence band and conduction band edge potentials of several semiconductors with respect to the Absolute Vacuum Scale (AVS). Adapted with values from [29].

Light absorption is in fact an important aspect to take into account for the choice of a semiconductor. As electron-hole pairs are only created when the energy of the photons exciting the semiconductor is at least equal to the band gap, E_g should be tuned to allow maximum solar absorption. Secondly, the band gap has to be higher than 1.23 eV which is the minimum energy required to split water. As discussed above, kinetic overpotentials have to be taken into account, which leads to an optimal band gap in the range of 1.6-2.4 eV, with an optimal value around 2 eV [28, 30]. A semiconductor with $E_g > 2.1$ eV can absorb light with a wavelength shorter than 600 nm, leaving a valuable part of the solar spectrum unused, which would eventually limits its efficiency to 17.4 % [31]. Tandem cells are one way envisaged to counter this problem. They use several light absorbers with different gaps to maximize the efficiency [31, 32].

A major limitation to the efficiency of photoelectrodes is the electron-hole recombination. Indeed, an electron excited to the conduction band can recover a lower energy state in the valence band, this phenomenon is referred to as recombination. It decreases the charge carrier

density and, consequently, the photocurrent, hence dramatically impacting the efficiency of the reaction. Figure 1.9 illustrates the different recombination pathways in a *n*-type semiconductor in contact with an electrolyte. The charge carriers can recombine in the bulk, in the depletion layer or on the surface. Usually, the recombination in the space charge region can be strongly reduced because the electric field induced by the band bending drives the separation between electrons and holes.

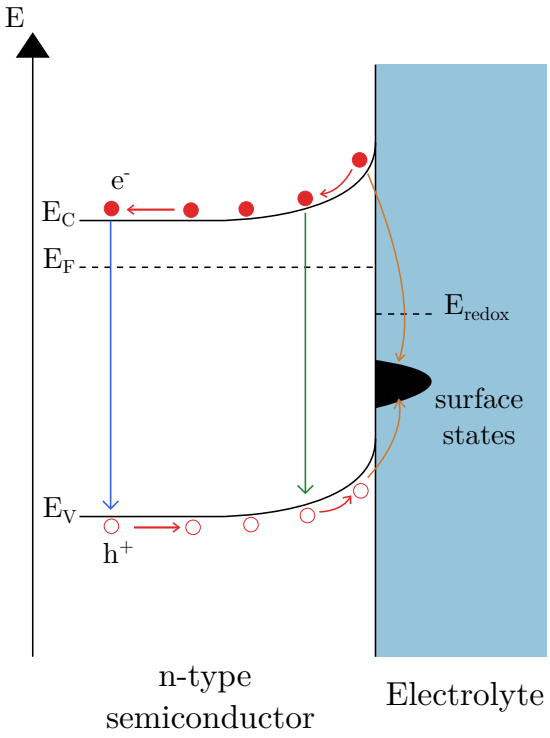

Figure 1.9 – Recombination pathways of electrons (plain red circles) and holes (hollow red circles) in a *n*-type semiconductor in contact with an electrolyte. The blue arrow materializes bulk recombination, the green arrow shows the space charge layer recombination and the orange arrows indicate the surface recombination.

Several solutions have been investigated to overcome this issue. Among them, doping is a widely explored route. It can be an effective way to improve the conductivity of the photoanode as well as bring the Fermi level position closer to the conduction band which should increase the flat band potential and consequently the band bending upon contact with the electrolyte. In the case of hematite, many studies focused on the doping by transition metals such as Ti [33–38], Cr [39], Zn [38], Mo [39], Si [33, 40], Mg [41]. Regarding $BaTiO_3$, doping have been considered to improve light absorption and extend it to the visible part of the solar spectrum. One can, for instance, cite doping with Fe [42, 43], Rh [44, 45], Mo [46], Zn [47], Ni [43] or N [48].

Another way to reduce electron-hole recombination is through the use of an internal electric field. Indeed, the electric field can allow to separate the photogenerated charge carriers and hence reduce the recombination rate. When two semiconductors are brought into contact, an electric field arises due to the equilibration of the Fermi levels. This phenomenon gave rise to numerous devices based on these *p*-*n* junctions such as transistors or solar cells. Many works tried to take advantage of *p*-*n* junction to built photoanodes. Lin *et al.* for example studied the junction of *p*-type Mg-doped α-Fe_2O_3 and α-Fe_2O_3 as a photoanode for solar water splitting [41]. Other reported results include, for example, the junction of amorphous *p*- or *n*-type Si with crystalline intrinsic Si [49], *n*-TiO_2/*p*-Cu_2O [50], *p*-$CaFe_2O_4$/*n*-TaON [51], $BiVO_4/WO_3$ [52, 53], *p*-NiO/α-Fe_2O_3 [54] or Fe_2O_3/TiO_2 [55, 56].

Ferroelectric materials could also be a very convenient alternative to provide an internal electric field. Indeed, they exhibit a spontaneous internal polarization and thus a spontaneous internal electric field which could allow charge separation. These materials already have been investigated in the field of photovoltaics [57–59] or photocatalytic reactions [60–63]. Furthermore, it was suggested that ferroelectric materials can spatially localize the electron and hole half reactions because of the influence of the dipolar field on the charge carrier transport [64–67]. In the following section, the basic physics of ferroelectric materials are presented, considering in particular $BaTiO_3$ which is the focus of this PhD.

1.4 Ferroelectricity

Ferroelectricity is characterized by a spontaneous polarization whose orientation can be switched by the application of an external electric field. The spontaneous polarization stems from atomic distortions induced in a centrosymmetric configuration. Atoms with electric charges of opposite signs are displaced in opposite directions, generating a dipolar moment. The direction of the resulting polarization is therefore directly related to the direction of the movement of the ions. Spontaneous polarization is defined by the value of the dipole moment per unit volume.

$BaTiO_3$ (BTO) is an archetypal ferroelectric perovskite exhibiting a spontaneous polarization at room temperature. The phase transition between the paraelectric and the ferroelectric phase is at about 130 °C in bulk BTO and much higher for strained layers [68]. Above the Curie temperature, BTO has a paraelectric cubic structure where Ba^{2+} ions are located at the corners, O^{2-} ions at the center of the faces and a Ti^{4+} ion at the body center of the cell. Below the Curie temperature, BTO undergoes a phase transition to a tetragonal ferroelectric phase which shows a spontaneous polarization along the [001] direction. The relative displacement of Ti and O atoms induces a dipole moment as the structure is no longer centrosymmetric. The different phases of BTO as a function of temperature and polarization

direction are illustrated on Figure 1.10.

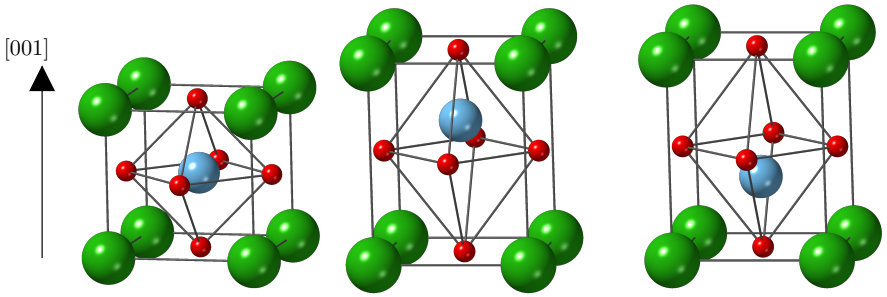

Figure 1.10 – Representation of the (a) cubic paraelectric, (b) tetragonal upward polarized and (c) tetragonal downward polarized $BaTiO_3$ unit cells. The green, blue and red ions stand for Ba^{2+}, Ti^{4+} and O^{2-}, respectively. The displacement of the Ti atom induces a polarization along the [001] direction. The distances are not to scale for sake of clarity.

Upon application of an electric field on the surface, the ions will move as a result of the electric force they are submitted to. If a positive potential difference is applied between the top surface and the back of the sample, Ti^{4+} cations will move towards the back of the sample while O^{2-} anions will be displaced towards the surface. This will generate a downward polarization $\overrightarrow{P_{down}}$. Conversely, for a negative applied electric field, an upward polarization $\overrightarrow{P_{up}}$ will appear. Because of boundary conditions due to the finite character of the surface, the electric field is discontinuous. This leads to the emergence of a surface charge density (σ), so called bound charges, as:

$$\sigma = \vec{P}.\vec{n} \tag{1.20}$$

where $\vec{n}$ is the surface normal vector. These charges in turn generate an electric field opposing the ferroelectric polarization called the depolarizing field, expressed as:

$$\overrightarrow{E_{dep}} = -\frac{1}{\varepsilon_0}\vec{P} \tag{1.21}$$

where ε_0 is the dielectric permittivity of vacuum. $\overrightarrow{E_{dep}}$ tends to destabilize the ferroelectricity, therefore it has to be screened in order for the polarization to subsist. This screening can occur in several ways which are now briefly described.

1.4.1 Screening mechanisms of the depolarizing field

The electric field compensating the depolarizing field can have an external origin. For example, the bound charges can be screened by metallic electrodes grown on the ferroelectric surface in short-circuit conditions. In such configurations, the electrons in the metal tend to screen the bound charges which generates an electric field across the ferroelectric, screening

the depolarizing field. Junquera and Ghosez studied this mechanism in $BaTiO_3$ thin films between two $SrRuO_3$ electrodes in short-circuit conditions using first principle calculations [69]. They showed that the out-of-plane polarization could subsist thanks to the charge compensation induced by the electrodes. However, they calculated that a critical film thickness exists (24 Å) below which the ferroelectricity is unstable. This was attributed to the depolarizing field due to imperfect screening.

Sai *et al.* investigated $PbTiO_3$ and $BaTiO_3$ ultrathin films sandwiched between two electrodes of Pt or $SrRuO_3$ [70]. Their work suggested that $PbTiO_3$ could exhibit ferroelectricity below 10 Å. Additionally, they determined that the nature of the electrode has a crucial influence on the stabilization of the ferroelectricity. It was further demonstrated that ionic relaxations at the interface between the ferroelectric and the electrode have a significant impact on the overall ferroelectricity [71]. Through first principle calculations on $SrRuO_3/BaTiO_3$ interfaces, Gerra *et al.* reported as well that the ionic relaxations are of primary importance in the screening of the ferroelectric bond charges which can lead to a decrease of the critical thickness for ferroelectricity (12 Å in this study) [72].

The influence of the nature of the electrode on the ferroelectricity was investigated in a systematic study with $PbTiO_3$ involved in capacitors between two metallic or metal oxide electrodes [73]. The authors showed that metal oxide electrodes yield a stronger adhesion with the ferroelectric. However, the metallic electrodes provide larger polarization magnitude and ferroelectric stability than oxide electrodes. The ferroelectric termination is also shown to significantly influence the ferroelectric properties of the capacitor.

When the ferroelectric is not involved in a capacitor, screening of the bound charges can arise through adsorption of molecules on the free surface. Scanning probe microscopy techniques such as scanning surface potential microscopy (SSPM), electrostatic force microscopy (EFM) and piezoresponse force microscopy (PFM) have become important tools to image the surface potential of ferroelectric materials. Kalinin and Bonnell published extensive research using these techniques and evidenced complete screening of bound charges, partly from adsorbates [74–76]. It was reported in a joint experimental theoretical investigation that adsorbates can stabilize the out-of-plane polarization in ultrathin $PbTiO_3$ films, the nature of the adsorbate being predicted from DFT calculations to influence the polarization direction [77]. Several other works were conducted to demonstrate that the chemical environment plays a very important role in the stabilization of the ferroelectricity. By means of *in situ* synchrotron x-ray scattering, it was shown that the ferroelectric polarization in $PbTiO_3$ could be switched under varying oxygen partial pressure [78–80], in agreement with a thermodynamic model taking into account ionic species of the chemical environment to compensate surface charge [81].

The screening of the depolarizing field can also arise from intrinsic charge carriers which can appear from defects, such as vacancies, and dopants. Oxygen vacancies are some of the commonly studied defects in oxides. They act as electron donors, as the missing O^{2-} ion leads to the release of two electrons, which are able to compensate the bound charges [82]. It was for example indicated from first-principles calculations that oxygen vacancies favor inward pointing polarization in $BaTiO_3$ [83] as well as in $PbTiO_3$ [78]. Additionally, it was determined from DFT calculations that oxygen vacancies can pin domain walls owing to a lower energy formation in the domain walls than in the bulk [84]. It is interesting to point out that the introduction of free charge carriers, by doping or through oxygen vacancies, screens the Coulomb interactions favoring the ferroelectric displacements and is thus expected to eventually cancel it out. Yet, ferroelectric displacements were observed in conducting reduced $BaTiO_{3-\delta}$ [85] and the critical carrier concentration to maintain ferroelectricity was predicted [82].

Finally, domain organization is another important mechanism of charge screening. Domains are defined as regions inside the material with a uniform polarization. These regions are separated from each other by boundaries called domain walls. The electric field induced by adjacent domains can screen the depolarizing field of a ferroelectric domain. This mechanism is illustrated on Figure 1.11. The black arrows indicate the polarization directions which induce bond charges (+ and - signs) because of discontinuities. These charges generate a depolarizing field (red straight arrows) screened by the macroscopic electric field in each adjacent domains (red curved and straight arrows). The existence of domain organization on the surface of $BaTiO_3$ have been reported at the end of the 1940s [86, 87].

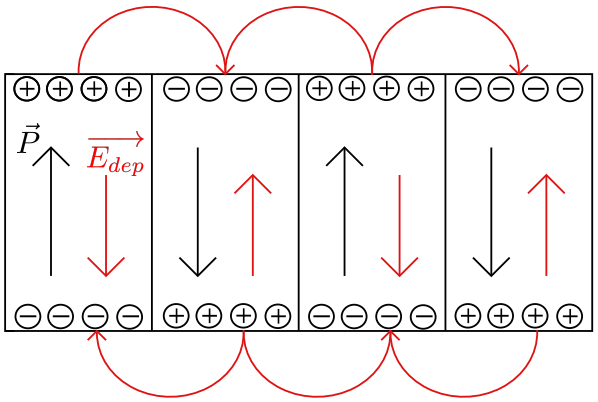

Figure 1.11 – Representation of domain ordering in an out-of-plane polarized ferroelectric. Black arrows show the polarization direction while red arrows are the depolarizing field induced by the surface charge density (+ and - symbols).

Ultrathin films exhibit a very strong depolarizing field which can cause the material to order in thin stripe domains to minimize the depolarizing field. In particular, 180° stripe domains of alternate up and down polarizations have been observed in $PbTiO_3$ [88–90]. A first principles based investigation was conducted by Kornev *et al.* to depict the influence of the residual depolarizing field on the ferroelectricity [91]. They modeled $Pb(Zr_{1-x}Ti_x)O_3$ thin films with an out-of-plane polarization under tensile and compressive in-plane strain. They evidenced that in unstrained systems under high residual depolarizing field, the polarization aligns along an in-plane direction. Additionally, the tensile strain favors the stabilization of parallel polarization while compressive strain induces the apparition of out-of-plane polarization. Interestingly, in compressively strained structures, it was observed that a rotation of the polarization at the junction between two domains appears to minimize the large depolarizing field induced by uncompensated bound charge. After several first-principles calculation studies on ferroelectrics short-circuited between two electrodes accounting only for the electrodes as source of screening [69, 72, 92], Aguado-Puente and Junquera also included domain formation as a possible screening mechanism [93]. They simulated $BaTiO_3$ sandwiched between two electrodes of $SrRuO_3$ and showed that, in this configuration, it is possible to stabilize ferroelectricity at thicknesses lower than the predicted critical value for uniformly polarized films [69]. This result hints that domain formation can help screening the depolarizing field in ferroelectric thin films.

1.4.2 Band bending

The screening of the depolarizing field caused by internal free charge carriers or defects induces band bending at the surface of the ferroelectric. The band bending arising at the interface between a ferroelectric and an electrolyte is depicted on Figure 1.12 in the case of complete screening in the bulk. For a downward polarization (P_{down}), the negative polarization bound charges are screened by accumulation of positively charged species at the surface, such as holes or positive ions, resulting in an upward band bending. Consequently, downward polarization favors hole transfer from the surface of the ferroelectric to the electrolyte which is of primary importance for water oxidation. On the other hand, upward polarization leads to an accumulation of negatively charged species (electrons, negatively charged ions) at the surface to screen the positive bound charges. This results in a downward band bending favoring the transfer of electrons towards the electrolyte which is of great interest for water reduction.

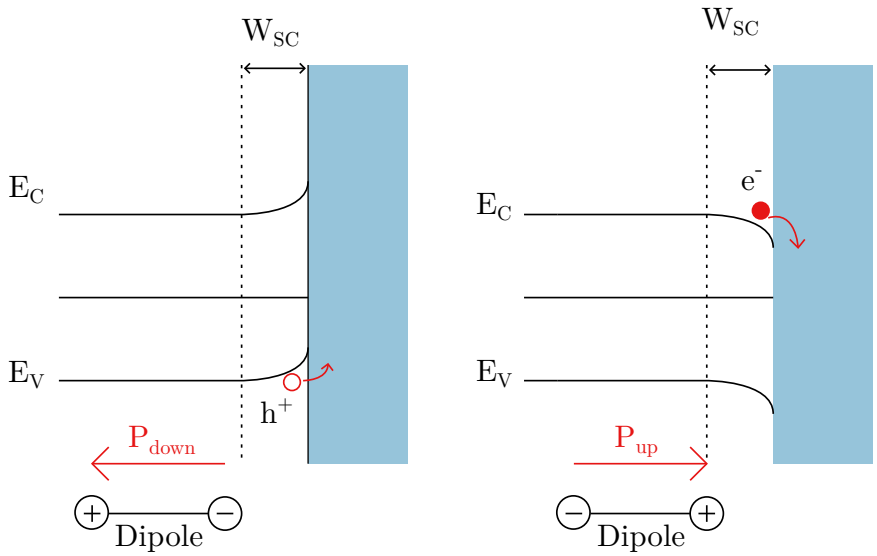

Figure 1.12 – Schematic band diagram in a ferroelectric material in an electrolyte with (left) a downward polarization P_{down} and (right) an upward polarization P_{up}. Reproduced from [61].

Chapter 2

Theoretical and experimental methods

2.1 Theoretical approach

2.1.1 Density Functional Theory (DFT)

The theoretical results presented in this thesis rely on the density functional theory (DFT). The properties of matter are governed by the laws of quantum mechanics. The quantum state of a system is described by the wavefunction Ψ which is the solution of the Schrödinger equation:

$$\widehat{H}\Psi = E\Psi \tag{2.1}$$

where $\widehat{H}$ is the Hamiltonian. For a system with N electrons and M ions, the Hamiltonian is expressed as:

$$\widehat{H} = -\frac{1}{2}\sum_{i}^{N}\nabla_i^2 - \sum_{i}^{N}\sum_{A}^{M}\frac{Z_A}{r_{iA}} + \sum_{i}^{N}\sum_{j>i}^{N}\frac{1}{r_{ij}} + \sum_{i}^{M}\sum_{B>A}^{M}\frac{Z_A Z_B}{R_{AB}} - \frac{1}{2m_A}\sum_{A}^{M}\nabla_A^2 \tag{2.2}$$

where A, B count over the nuclei and i, j count over the electrons. Yet, the Schrödinger equation with this Hamiltonian cannot be solved analytically for more than two bodies (*ie.* the hydrogen atom). Therefore, several approximations need to be introduced. The first one is the Born-Oppenheimer approximation which is based on the fact that the kinetic energy of nuclei is much smaller than the kinetic energy of electrons because of the large difference between their respective masses. Hence, the Hamiltonian can be approximated to the so-called electronic Hamiltonian:

$$\widehat{H} = -\frac{1}{2}\sum_{i}^{N}\nabla_i^2 - \sum_{i}^{N}\sum_{A}^{M}\frac{Z_A}{r_{iA}} + \sum_{i}^{N}\sum_{j>i}^{N}\frac{1}{r_{ij}} \tag{2.3}$$

However, it is still impossible to solve this equation, thus other approximations are required. Hartree proposed the first attempt to calculate the wavefunction, further improved by Hartree-Fock method to accommodate Pauli's principle by determining an antisymmetric wavefunction. Even though this method allows a more accurate description of atoms and molecules, it does not include any electronic correlation term and it is very demanding from a computational point of view for periodic solids.

A more appropriate theory to describe solids is the density functional theory. It was developed in 1964 by Hohenberg and Kohn who proved two theorems that enable to replace the complicated many body wavefunction with a much simpler electronic density $\rho(r)$ [94]. The first theorem states that:

> "The external potential $v(r)$ is (to within a constant) a unique functional of the electronic density $\rho(r)$; since, in turn $v(r)$ fixes $\widehat{H}$ it is seen that the full many particle group state is a unique functional of $\rho(r)$."

This means that all the system properties are completely determined by the electronic density of the system. The second theorem shows that the groundstate energy can be obtained variationally: the density that minimizes the total energy is the exact groundstate density. Nevertheless, these two theorems do not give an expression of the functional. It is only the Kohn-Sham formulation which allowed to evaluate the functional [95]. They considered a non-interacting system of electrons with the same ground state density than the interacting system. The total energy of the electron system can be written as follow:

$$E[\rho] = T_{KS}[\rho] + E_H[\rho] + E_{ext}[\rho] + E_{xc}[\rho] \tag{2.4}$$

where:

$T_{KS}[\rho]$ is the kinetic energy of the electrons without interaction

$E_H[\rho]$ is the classical coulomb electron-electron repulsion

$E_{ext}[\rho]$ is the interaction of the electrons with the external potential created by the nuclei

$E_{xc}[\rho]$ is the exchange-correlation energy

So far the DFT is exact as it does not contain any approximation. Yet, the exchange-correlation term $E_{xc}[\rho]$ is unknown and needs to be approximated. There are two widely used approximations: the Local Density Approximation (LDA) and the Generalized Gradient Approximation (GGA). In this thesis, we only used GGA because it provides a better description when the density varies rapidly giving more reasonable results for adsorption

for example. Within this approximation, the exchange-correlation term is a function of the electron density and its gradient. It is defined as:

$$E_{xc}^{GGA}[\rho] = \int \rho(r)\varepsilon_{xc}[\rho(r)]\,\mathrm{d}r + \int F_{xc}[\rho(r), \nabla\rho(r)]\,\mathrm{d}r \tag{2.5}$$

where ε_{xc} is the exchange-correlation energy density of a homogeneous electron gas with density ρ. Numerous variations of this approximation have been proposed. In this thesis, we use the Perdew-Burke-Ernzerhof (PBE) functional [96]. However, GGA gives a poor description of the electronic structure of strongly correlated materials, such as metal oxides. Therefore, it needs to be further improved.

An additional term needs to be implemented in order to properly describe the highly localized electron orbitals (typically d and f orbitals). This is done in the framework of DFT+U which includes an on-site Coulomb repulsion Hubbard U term. Here, we adopt Dudarev's approach [97] and apply an effective parameter $U_{eff} = 3.5$ eV on the Ti $3d$ electrons.

Finally, in this work we intend to describe the adsorption processes of water on $BaTiO_3$ surfaces. Therefore, it is important to accurately take into account the long-range van der Waals interactions which play an important role in such adsorption processes. It is known that standard DFT functionals fail to properly describe the long-range dispersion interactions [98]. Several methods have been presented to account for London dispersion interactions in DFT calculations. In this work, we used the dispersion corrected density functional theory DFT-D3 for every calculation treating adsorption [99].

2.1.2 Computational details

2.1.2.1 Numerical parameters

The calculations are performed using the Vienna *Ab initio* Simulation Package (VASP) code [100, 101]. It relies on periodic systems to solve the Kohn-Sham equations. The wavefunctions are calculated through plane wave functions in the reciprocal space. In principle the plane wave basis should be infinite. However, such infinite calculations are impossible to process. Thus, the plane wave basis set is truncated to contain only plane waves which have a kinetic energy smaller than a defined cut-off energy. In our calculations, this cut-off energy is set to 500 eV.

The wave functions are supposed to be defined on the whole Brillouin zone. Yet, in practice, the integration is done over the sum of a finite number of selected k-points in the first Brillouin zone. In this work, a Monkhorst-Pack mesh [102] is used to sample the first Brillouin zone. A $7 \times 7 \times 1$ Monkhorst-Pack grid, corresponding to 25 irreducible k-points, is

used to sample the first Brillouin zone of the smallest periodicity. This led to an accuracy of 10^{-4} eV. Then for the different lateral periodicities (N) considered to modify the ferroelectric domain width and in order to tune the water coverage, the k-points mesh is determined accordingly.

Another parameter that needs to be fixed is the vacuum layer implemented to prevent all interactions between two neighboring slabs along the [001] direction which is necessary to create a surface. Its thickness has also been optimized and the convergence is reached for a vacuum layer of 20 Å.

The core electrons are described using projector augmented wave (PAW) pseudopotentials [103, 104]. They explicitly include ten valence electrons for Ba ($5s^2$ $5p^6$ $6s^2$), six for O ($2s^2$ $2p^4$), twelve for Ti ($3s^2$ $3p^6$ $4s^2$ $3d^2$) and ten for Pt ($5d^9$ $6s^1$).

The electronic convergence is considered to be reached when the difference in total energy between two electronic iterations is lower than 10^{-6} eV. A second threshold has to be fixed for the structural optimization. The optimization is stopped when the forces converge below 10^{-2} eV.Å^{-1}.

2.1.2.2 Simulation of the out-of-plane polarization

The objective of this thesis is to study the out-of-plane polarization in $BaTiO_3$ (001) surfaces. From a theoretical point of view, the modeling of a polarization perpendicular to the surface is not straightforward as it generates an accumulation of surface charges. This accumulation induces an electric field, called depolarizing field which counters the macroscopic polarization and destabilizes the ferroelectric state. Ultimately, this depolarizing field would lead to the stabilization of the paraelectric phase. Consequently, to overcome this issue it is compulsory to implement a computational protocol that would allow the polarization to sustain. Three different approaches were already proposed in previous studies. It was suggested to fix the atomic positions inside the slab to the known ferroelectric bulk positions and allow the surface layers to relax [105]. However this method does not screen the depolarizing field in the bulk part of the slab as the atomic positions are fixed. Another way to counter the electric field induced by the polarization is to apply an external electric field opposed to the depolarizing field [83, 106]. The benefit of this approach is that all atoms are free to relax but the value of the external field to apply is not known beforehand. Additionally, when performing water adsorption calculations the artificial electric field could affect the adsorption behavior and lead to spurious results. Thus we use a third method firstly introduced by Migoni *et al.* [107] in a molecular dynamics study of deposited $PbTiO_3$ thin films and then extended by Shimada [108] for periodic DFT calculations of free-standing $PbTiO_3$ thin films. This method consists in dividing the slab in alternating domains with an opposite polarization direction,

thus resulting in a simulation cell with no net dipole moment. A schematic representation of this approach is presented in Figure 2.1. It has the advantage of depicting the reality as it has already been experimentally shown that ferroelectric materials can exhibit polydomains [88, 89, 109]. Contrary to the two previously mentioned methods, this approach allows to completely screen the depolarizing field as well as letting the atoms to fully relax.

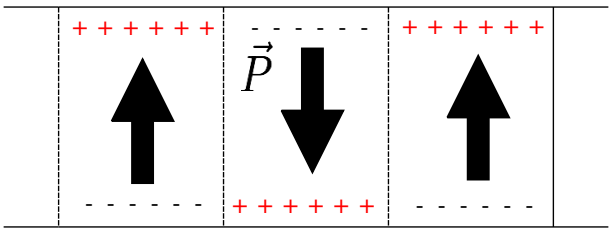

Figure 2.1 – Schematic representation of the polarization pattern used to model the out-of-plane polarization in a slab. The black arrows show the polarization directions.

2.1.2.3 Local polarization

The local polarization discussed in this thesis is defined in each unit cell using the following equation introduced by Vanderbilt [110]:

$$\mathbf{P} = \frac{e}{\Omega_c} \sum_j \omega_j \mathbf{Z}_j^* \mathbf{u}_j \tag{2.6}$$

where e and Ω_c refer to the electron charge and the volume of the unit cell, respectively. The unit cell considered to calculate the local polarization is centered on a Ti atom in the case of the BaO termination whereas for the TiO_2 termination it is centered on an O atom of a BaO layer. The index j of the sum covers all atoms in the unit cell, with ω_j and $\mathbf{u}_j$, the weight of atom j in the unit cell and its atomic displacement vector from the ideal lattice position, respectively. The atomic weight of each atom in the unit cell is displayed in Table 2.1. Finally, $\mathbf{Z}_j^*$ is the Born effective charge tensor of atom j in the optimized cubic bulk of $BaTiO_3$.

Termination	BaO		TiO_2	
ω_j	Volume	Surface	Volume	Surface
Ba	1/8	1/4	1/4	–
Ti	1	–	1/2	1
O_I	1/2	1	1	–
O_{II}	1/2	–	1/4	1/2

Table 2.1 – Atomic weight ω_j of the atoms in the unit cell of $BaTiO_3$ used for the calculation of the local polarization for both BaO and TiO_2 terminations. O_I and O_{II} symbolize the O atoms belonging to the BaO and TiO_2 layers, respectively.

While due to symmetry considerations the Born effective charge is isotropic for Ba and Ti, it is anisotropic in the case of O atoms. Indeed, depending on the O atom position compared to the Ti-O bond it is involved in, two components in the Born effective charge have to be differentiated. Figure 2.2 shows the Ti atom inside the octahedron formed by the O atoms. It is seen that the displacement of the O atoms can be either parallel ($\vec{u}_{\parallel}$) or perpendicular ($\vec{u}_{\perp}$) to the Ti-O bond they participate in. This leads to two different values of the Born effective charge for the oxygen: $Z^*_{O_{\parallel}}$ and $Z^*_{O_{\perp}}$. The values of the computed Born effective charges are reported in Table 2.2. They are in a good agreement with the ones previously calculated by Ghosez *et al.* [111].

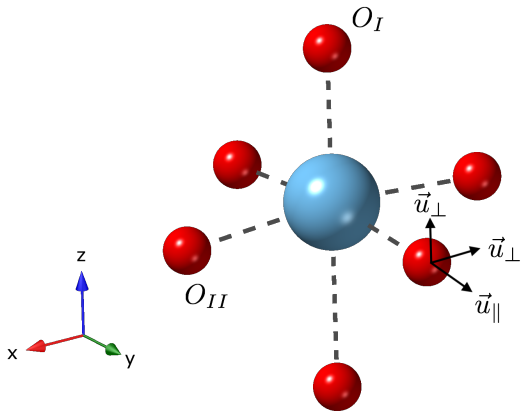

Figure 2.2 – Representation of the Ti (in blue) and O (in red) atoms in a $BaTiO_3$ unit cell. The vectors $\vec{u}$ designate the atomic displacements of the O atoms. O_I and O_{II} symbolize the O atoms belonging to the BaO and TiO_2 layers, respectively.

	Ba	Ti	$O_{\parallel}$	$O_{\perp}$
Z^*_j	2.73	6.82	-5.43	-2.06

Table 2.2 – Born effective charges calculated in the optimized cubic bulk of $BaTiO_3$.

2.2 Experimental techniques

2.2.1 X-ray Photoelectron Spectroscopy (XPS)

X-ray Photoelectron Spectroscopy (XPS) is a commonly used chemical characterization technique performed under Ultra High Vacuum (UHV) conditions which relies on the photoelectric effect. This technique is highly surface sensitive due to the strong inelastic interactions between the electrons and the material. Figure 2.3 illustrates the photoemission process. Photons excite the sample which can lead to the ejection of an electron, called photoelectron, if the energy of the incident photons ($h\nu$) is at least equal to the binding energy (E_b) of

the electron. The photoelectrons extracted from the material are sorted according to their kinetic energy (E_k) by an energy analyzer. The kinetic energy of the electrons is expressed as:

$$E_k = h\nu - E_b - \Phi \tag{2.7}$$

where $h\nu$ is the photon energy and Φ is the work function which represents the minimum energy required to extract an electron from the material. The energy of the electrons is not only dependent on the nature of the material but also gives information on the chemical environment of the atom. A modification of the chemical environment, such as the oxidation state, translates as a chemical shift of the binding energy of the electron.

The standard XPS experiments were conducted at the synchrotron facility ASTRID 2 of ISA laboratory in Aarhus, Denmark. The electrons circulating in the storage ring have an energy of 580 MeV. The experiments presented here were carried out on MATLINE beamline which includes a SX-700 monochromator able to tune the photon energy in a range of 20 to 700 eV. This is particularly useful to optimize the photoionisation cross section as well as the inelastic mean free path of the electrons.

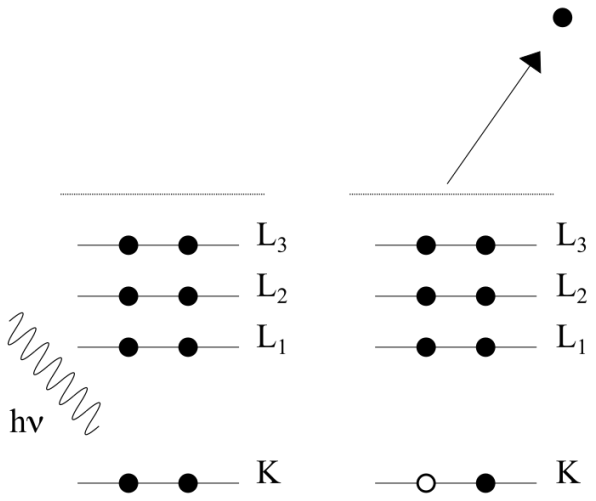

Figure 2.3 – Schematic representation of the photoemission process.

2.2.2 Near Ambient Pressure X-ray Photoelectron Spectroscopy (NAP-XPS)

As mentioned above, photoelectron spectroscopy has to be performed under UHV conditions to maximize the number of electrons reaching the detector as well as preventing the contamination of the sample by the surrounding environment. Though this is a powerful technique, it does not allow to follow reversible chemical reactions at real-world pressure. Hence, new

instrumentation was developed in order to make the acquisition of XPS spectra possible at much higher pressure (up to some hPa). This was done thanks to the introduction of differential pumped analyzers (see Figure 2.4). In this configuration the sample is positioned close to the aperture, or nozzle, of the analyzer at a distance of some hundreds of μm. The pressure is then quickly decreased using a differential pumping separating the analysis chamber from the analyzer. In the analyzer, the photoelectrons are focused into the apertures between the differential pumping stages using electrostatic lenses.

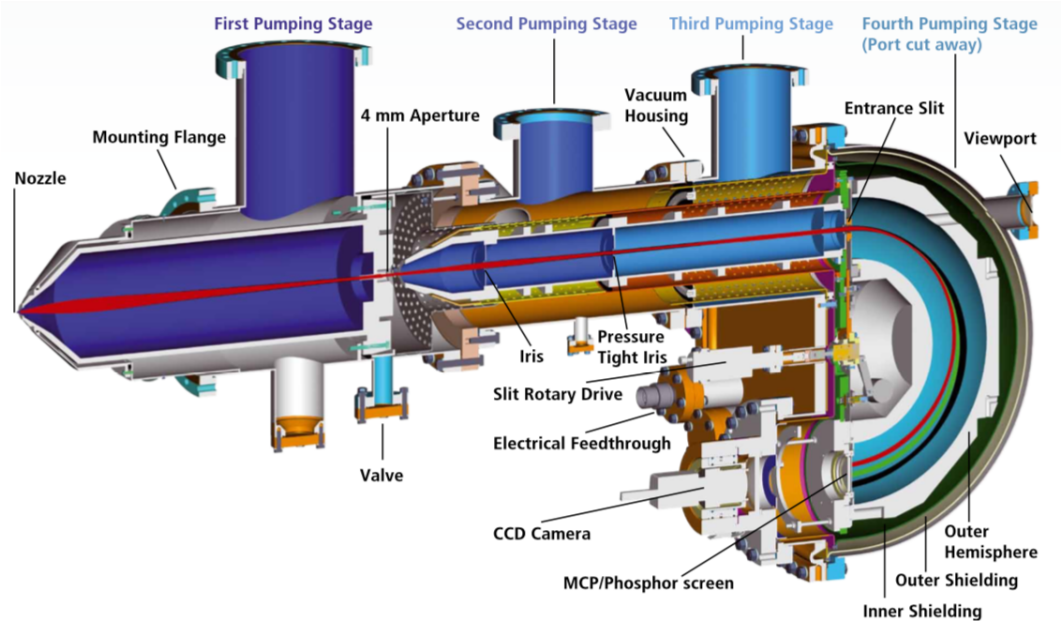

Figure 2.4 – Cross section view of the SPECS PHOIBOS 150 NAP [112].

The experiments presented in this thesis were conducted at the synchrotron SOLEIL on the TEMPO beamline which was adapted to couple the NAP branch of the beamline with the time resolved aspect presented below. A PHOIBOS 150 NAP provided by SPECS was used (see Figure 2.4). This setup allowed us to perform also time resolved photoemission spectroscopy (see section 2.2.3) in near ambient pressure conditions which gives the possibility to measure the charge dynamics of a sample with a monolayer of adsorbed water, getting closer to the photocatalytic reaction conditions.

2.2.3 Time Resolved Photoelectron Spectroscopy (TR-PES)

Time resolved photoelectron spectroscopy is a powerful tool to study the charge dynamics in a semiconductor. The method is based on a pump-probe approach. The general idea is to excite the material (pump) using a laser and to probe the changes induced by the pump using the synchrotron radiation. The principle of the technique is presented in Figure 2.5. In essence, a laser excites the semiconductor which generates electron-hole pairs in the material. These charge carriers migrate either to the surface or to the bulk depending on the

type of semiconductor (n-type or p-type) resulting in a charged surface. In the meantime, the synchrotron radiation is used to probe the system through fast XPS measurements as the laser is turned on and off. If the surface is positively charged after the pump, the extracted photoelectrons will be decelerated leading to a smaller kinetic energy translated into a shift in the recorded photoemission peaks. On the other hand, if the surface is negatively charged, meaning that electrons migrate towards the surface, the measured kinetic energy of the photoelectrons will be higher.

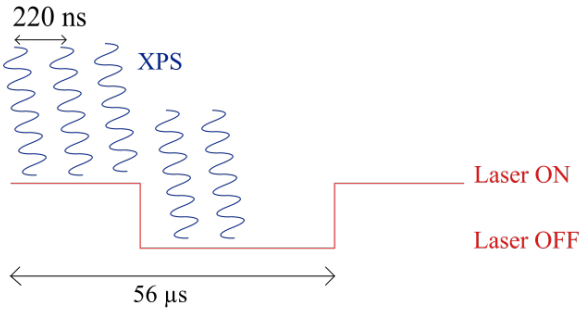

Figure 2.5 – Schematic representation of time-resolved XPS measurement.

The experiments were realized at the synchrotron SOLEIL on TEMPO beamline. The photon energy can be modified between 50 and 1500 eV. The wavelength of the laser is chosen to be as close as possible to the maximum absorption of the material. In our case, for the BTO samples, the laser had a wavelength of 355 nm and was modulated with a 50% duty-cycle at a period ranging from 200 ms to 2s. Regarding the hematite samples, a wavelength of 405 nm was provided by a CUBE laser with a power between 20 and 100 mW. The laser was modulated with a 40% duty-cycle at a period $T = 56\ \mu s$. Fast XPS spectra were captured every 220 ns using a delay-line detector.

Chapter 3

Pt(001)/$BaTiO_3$(001) interface

The bare Pt/$BaTiO_3$ interface is first considered to better understand the role of the platinum substrate in the polarization of BTO thin films. Indeed, the substrate can widely modify the electronic, structural and polarizability properties of the overlayer. Thus, it is important to characterize the properties of the film when grown on top of a realistic substrate. In this chapter, density functional calculations are used to depict the interface. The bulk has to be firstly described in order to understand the effects of the surface on the ferroelectricity. Then, the stability of the interface needs to be unraveled before finally discussing the polarization of the films and in particular determine the influence of the Pt substrate.

3.1 $BaTiO_3$ bulk

The atomic positions after the structural optimization of the bulk tetragonal phase are reported on Table 3.1. The lattice parameters are found to be $a = 4.006$ Å and $c = 4.184$ Å corresponding to a c/a ratio of 1.044. These parameters are very similar to the ones calculated in previous DFT studies [105, 113–116] where a has been calculated between 3.954 and 4.013 Å for a c/a ratio between 1.006 and 1.045, depending on the level of calculation. These results can be compared to the experimental lattice parameters [117] $a = 3.994$ Å and $c = 4.036$ Å showing, as it is well known [114, 118], that GGA tends to overestimate the tetragonality of BTO. Using the Hubbard effective parameter $U_{eff} = 3.5$ eV on the d electrons of Ti improves the description of the band gap which increases from 1.79 eV to 2.23 eV leading to a value closer to the experimental value of 3.2 eV [119]. A spontaneous polarization $P = 31.7$ µC.cm^{-2} was calculated following the Berry phase method [120, 121]. It is slightly higher than the experimental value [122, 123] of 27 µC.cm^{-2} but is in the range of previously calculated ones [113, 115] (from 24.3 to 35.1 µC.cm^{-2}). The higher calculated value in this study is explained by the larger tetragonality induced by the GGA calculation.

Atom	Position
Ba	(0,0,0)
O_1	(0.5, 0.5, 0.467)
O_2	(0.5, 0, 0.480)
O_3	(0, 0.5, 0.480)
Ti	(0.5, 0.5, 0.513)

Table 3.1 – Relative atomic positions in the ferroelectric tetragonal $BaTiO_3$ bulk phase.

3.2 Description of the Pt substrate

In this work, Pt(001) is used as a substrate for the epitaxial growth of BTO(001). To reproduce as faithfully as possible the experimental strain induced by the platinum in the BTO overlayer, the substrate is described using its experimental lattice parameter (a_{Pt} =3.92 Å), corresponding to a compressive strain of 2.1% for BTO. To determine the Pt thickness required to achieve a good accuracy, the convergence is checked using the adhesion energy defined as:

$$E_{adh} = E_{Pt/BTO} - E_{Pt} - E_{BTO} \tag{3.1}$$

where $E_{Pt/BTO}$ is the total energy of the optimized interface Pt/$BaTiO_3$, E_{Pt} is the total energy of the optimized isolated Pt substrate and E_{BTO} is the total energy of the optimized isolated BTO slab. Calculations were done for 5 and 7 layers of Pt. It resulted that the convergence is reached for 5 layers as the adhesion energy difference is lower than 1.5 meV.Å^{-2}. Thus, in the following, the interface is modeled using only 5 layers of Pt where the bottom 2 layers are frozen to their bulk positions and the upper 3 layers are allowed to relax freely.

3.3 Stability of the interface

The stability of the Pt(001)/$BaTiO_3$(001) interface is now discussed. Because of its perovskite structure, BTO can exhibit two different terminations, namely BaO and TiO_2. Both of them have to be considered for each interface: the one between Pt and BTO as well as the interface between BTO and the vacuum. The influence of another structural parameter should be analyzed: the alignment of the first BTO layer which grows on Pt. Two different cases are defined depending on the position of the Ti atom (respectively Ba) with respect to the Pt surface: top and hollow, as shown on Figure 3.1. The stability of the interface is analyzed using the adhesion energy defined above. It can be split into the sum of two components as:

$$E_{adh} = E_{int} + E_{strain} \tag{3.2}$$

where E_{int} represents the interaction energy between BTO and the Pt substrate which is negative and defined as:

$$E_{int} = E_{Pt/BTO} - E_{Pt} - E_{strained\ BTO} \tag{3.3}$$

with $E_{strained\ BTO}$ the energy of isolated BTO constrained to the Pt lattice parameter. E_{strain} is positive and corresponds to the strain induced in BTO by the epitaxy, calculated as the energy difference between the unstrained and the constrained isolated BTO slab.

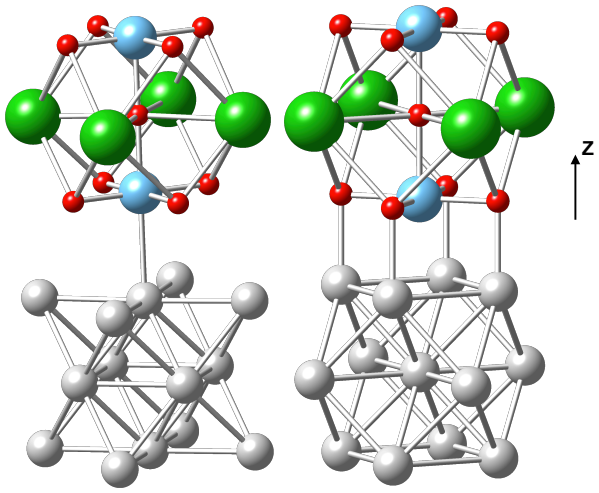

Figure 3.1 – Sideview of the top (left) and hollow (right) adsorption positions of $BaTiO_3$ on Pt(001) in the case on the Pt/TiO_2 interface. The z axes shows the [001] direction. For sake of clarity, only three layers are represented for both the substrate and the overlayer. Pt atoms are represented in gray, Ba in green, Ti in blue and O in red.

To assess its stability, the interface was modeled using a slab with a lateral periodicity of 1 unit cell containing 5 layers of Pt and 11 layers of BTO in the case of the symmetric slabs and 10 layers of BTO for the asymmetric ones. As previously stated, the experimental lattice parameter of Pt ($a_{Pt} = 3.92$ Å) was used and its bottom two layers were fixed to their bulk positions while the upper three layers were allowed to relax. Considering that there are two possible adsorption sites for the cation on Pt (top and hollow), 8 different cases have to be examined. The results are reported on Table 3.2.

The first thing to be noticed is that the first layer of BTO growing on Pt induces a very different behavior in terms of stability. When the growth starts with a first BaO layer, both adsorption sites present a very comparable adhesion energy and thus cannot be distinguished. This equivalence between top and hollow sites can be understood because of the weak interaction between Pt and Ba, introducing a large distance between the substrate and the overlayer. Indeed, as reported in Table 3.2 this distance is 3.4 and 3.8 Å for the top and hollow sites, respectively, which diminishes the impact of the different adsorption sites. The interaction energy (E_{int}) actually confirms it as it is identical regardless of the

On Pt		TiO_2		BaO	
Upper termination		TiO_2	BaO	TiO_2	BaO
E_{strain}		30	32	32	43
Top	E_{adh}	12	17	-15	12
	E_{int}	-19	-15	-47	-32
	$d_{Pt/cat}$	2.79	2.84	3.37	3.35
Hollow	E_{adh}	-31	-30	-17	10
	E_{int}	-62	-62	-50	-33
	$d_{Pt/cat}$	2.19	2.20	3.77	3.78

Table 3.2 – Adhesion energies E_{adh} in meV.Å^{-2}, interaction energies E_{int} in meV.Å^{-2}, strain energies E_{strain} in meV.Å^{-2}, and distances $d_{Pt/cat}$ between the Pt substrate and the cation (Ti or Ba) from the overlayer in Å.

adsorption position. Thus, when the growth begins with a first BaO layer, the only distinction arises from the surface termination. It turns out that the symmetric [BaO/BaO] slabs are slightly unstable ($E_{adh} \approx 15$ meV.Å^{-2}) while the [BaO/TiO_2] asymmetric ones exhibit a small stabilization ($E_{adh} \approx -15$ meV.Å^{-2}). This discrepancy can be explained by the nature (symmetric or asymmetric) of the overlayer which can lead to different sensitivities to interlayer relaxations induced by the presence of the substrate only on one side.

On the other hand, when it comes to the Pt/TiO_2 interface, the top and hollow positions can easily be discriminated. It is clear that the hollow site is favored whereas the top site is unstable. This behavior comes mainly from the strain induced by the substrate on BTO. As a matter of fact, the difference of lattice parameter between both materials constrains BTO with a mismatch of -2.1%. This strain leads to an energy cost of around 30 meV.Å^{-2} for both [TiO_2/TiO_2] and [TiO_2/BaO] slabs. Even though the interaction energies between Pt and TiO_2 are always negative, for the top position it is not large enough to compensate the destabilization introduced by the strain. As a result, the global adhesion energy is positive leading to an unstable structure when the cation is on top position. These results are in agreement with previous studies. Notably, Rappe *et al.* [70] also showed that the Pt/TiO_2 interface with the Ti atom on the hollow site is the most stable structure. Stengel *et al.* [71] demonstrated that this is mainly due to the nature of the Pt-O bond. In fact, in the situation where Ti is on the hollow site, all surrounding O atoms are located directly on top of Pt atoms (see Figure 3.1) creating a strong interaction, able to compensate E_{strain}.

As the results presented above clearly demonstrate that the Pt/TiO_2 interface with the Ti atoms on the hollow sites is the most stable, only this configuration will be considered in the following. Nevertheless, regarding the surface termination, both TiO_2 and BaO terminations need to be envisaged as they both present an equivalent stability.

3.4 Polarization in $BaTiO_3$ deposited on Pt

3.4.1 Stability of the ferroelectric phases

The in-plane compressive strain induced by the platinum substrate on the BTO thin film favors the apparition of an out-of-plane polarization along [001]. It is important to evaluate the critical thickness of BTO required to give rise to a polarization. Hence, the stabilization of the ferroelectric phase over the paraelectric one is now investigated as a function of the thickness of the BTO film. The influence of the substrate on this critical thickness also needs to be established. To this end, the symmetric [TiO_2/TiO_2] slab is considered with a thickness ranging from 7 to 15 layers, either isolated or deposited on Pt. Additionally, it is also interesting to determine the influence of the ferroelectric domain size. The domain width can be tuned by varying the width of the slab. In our conditions, the domain width is infinite along y while it is finite along x. Thus, the size of the domains depends only on the periodicity along x. The width of the slab is denoted as the number of unit cells (N). Domain sizes with $N = 2$, 4 and 6 are investigated.

Let us first discuss the two unit cell periodicity. The electronic influence of Pt is examined by comparing the heterojunction of BTO deposited on Pt and the isolated BTO constrained to the lattice parameter of Pt. The relative stability between the ferroelectric and paraelectric phases is expressed as:

$$\Delta E = \frac{E_{ferro} - E_{para}}{\frac{N}{2}} \tag{3.4}$$

where E_{ferro} is the total energy of the ferroelectric phase, E_{para} is the total energy of the paraelectric phase and N is the number of lateral unit cells. The results are presented on Figure 3.2. They indicate that the ferroelectric phase is stabilized over the paraelectric one as the thickness increases, in particular when BTO is grown on Pt. Yet, the presence of platinum does not modify the critical thickness that stabilizes polarized systems: in both cases symmetric ferroelectric systems are stable for slabs of 11 or more layers, corresponding to a thickness of 23 Å.

The critical thickness has also been determined for the four and six unit cell periodicity. For the isolated BTO the critical thickness is not impacted by the lateral periodicity (see Figure 3.2). However, in the case of the interface with Pt the ferroelectric phase is stabilized as soon as 9 layers of BTO are grown, for both $N = 4$ and $N = 6$, demonstrating a different behavior between free-standing and deposited BTO. This result confirms the role of boundary conditions, already evidenced both theoretically [107] and experimentally [124], in the critical thickness. It is also interesting to determine the most stable ferroelectric domain size when the critical thickness is reached. Therefore, the stability of the ferroelectric phase is carefully

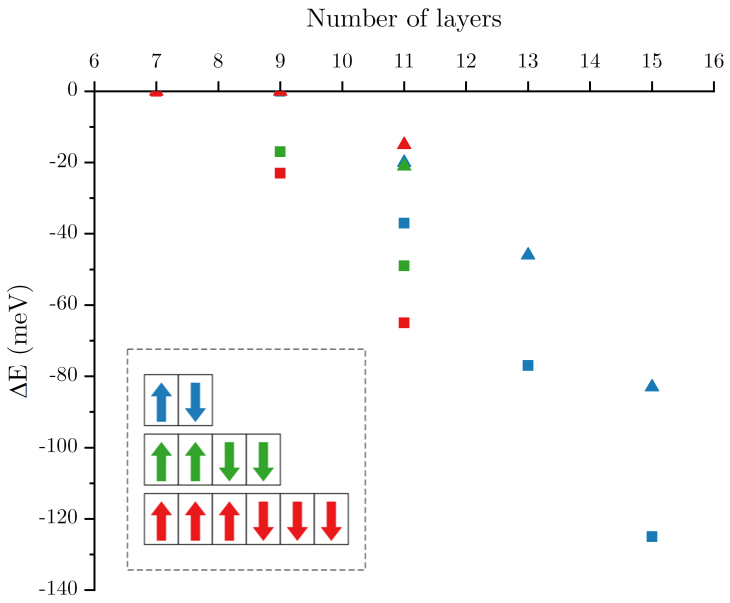

Figure 3.2 – Relative stability between ferroelectric and paraelectric phases in meV, as a function of the number of layers and the number of lateral unit cells N. Triangles correspond to isolated strained BTO and squares correspond to BTO deposited on Pt. Periodicities of two ($N = 2$), four ($N = 4$) and six ($N = 6$) are reported in blue, green and red, respectively. For the sake of clarity, these three periodicities are sketched in the inset.

analyzed for the 11 layer films, both with and without Pt. In the latter case, systems with a width of 2 or 4 unit cells are favored (ΔE around -20 meV), while those with a periodicity of 6 unit cells are less stable with $\Delta E = -15$ meV. These findings are fully consistent with previous results of Dionot *et al.* [125]. The presence of platinum broadly changes this behavior. In this case, the larger stabilization of the ferroelectric phase over the paraelectric phase already observed for the 2 unit cell system is still present, but is even larger as the periodicity increases. It is clear that for BTO deposited on Pt the 6 unit cell slab is favored (in red in Figure 3.2). It thus seems that Pt favors the apparition of larger ferroelectric domains.

3.4.2 Polarization patterns

Now that the stability of the $Pt/BaTiO_3$ interface has been characterized and the stabilization of the ferroelectric phase determined, the polarization of the BTO thin films can be analyzed in details, following the method presented in section 2.1.2.2. Given the previous results, structures of 11 layers or more are studied.

3.4.2.1 Isolated $BaTiO_3$

First, the isolated BTO is considered with a thickness of 11, 13 and 15 layers. The values of the local polarization are presented in Figure 3.3. The left side of the slab corresponds to the P_{up} polarization, with displacement of Ti atoms outwards, while the right side corresponds to the P_{down} polarization with displacement of Ti atoms inwards. The values reported display only the contribution along the z axis. Indeed, in the two unit cell periodicity, the lateral contributions (along x and y) are null. While we showed that the increase of the thickness favors the ferroelectric phase, there is no important change in the polarization behavior with the modification of the thickness. A low polarization (between 5 and 12 µC.cm^{-2}) is systematically observed at the surface regardless of the number of layers. On the other hand, as the thickness of the slab increases, the polarization in central unit cells is enhanced to get closer to the strained bulk polarization. Indeed, the polarization was calculated in the strained BTO bulk with a compressive strain of -2.1 %: it resulted that when BTO is constrained to the Pt lattice parameter, its bulk polarization is enlarged from 31.7 to 37.1 µC.cm^{-2}. This increase corresponds to a 20 % augmentation of the polarization, which is in agreement with previous results: Junquera and Ghosez [69] observed a 29 % increase for BTO involved in capacitors with a comparable constraint. Qualitatively, the behavior fully agrees with what was observed by Dionot *et al.* [125] for a 3.8% constraint.

3.4.2.2 Influence of the Pt substrate

Let us now discuss the electronic influence of the platinum substrate on the polarization of the ferroelectric overlayer in the case of the 2 unit cell periodicity. The first thing to be noted is that obvious dissymmetries of the local polarization are observed despite the use of symmetric initial configurations (see Figure 3.3). This loss of symmetry will be analyzed in the following but it is important to mention that it does not give rise to a depolarizing field as it could have been expected. Indeed, the presence of a metallic substrate allows the accumulation of charges which compensate the ferroelectric surface charge density [69]. In the case of the heterojunction, three ferroelectric regions can be distinguished in BTO. First, the surface unit cells close to the vacuum region present a polarization comparable to the one observed without platinum. Neighboring cells have an opposite polarization with an absolute amplitude between 5 and 15 µC.cm^{-2}. Regarding the central unit cells, the behavior of the polarization is not modified by the presence of the substrate. As for isolated BTO, the polarization increases compared to the surface values. It should be pointed out that when deposited on Pt, the polarization in the overlayer is slightly higher and thus closer to the bulk value. Finally, contrary to what happens in the rest of the slab, a large difference of behavior is observed at the interface between Pt and BTO. In these unit cells, the symmetry is broken as both local polarizations point towards the same direction even if their amplitudes completely differ. This discrepancy can be explained by the chemical bonding of interfacial

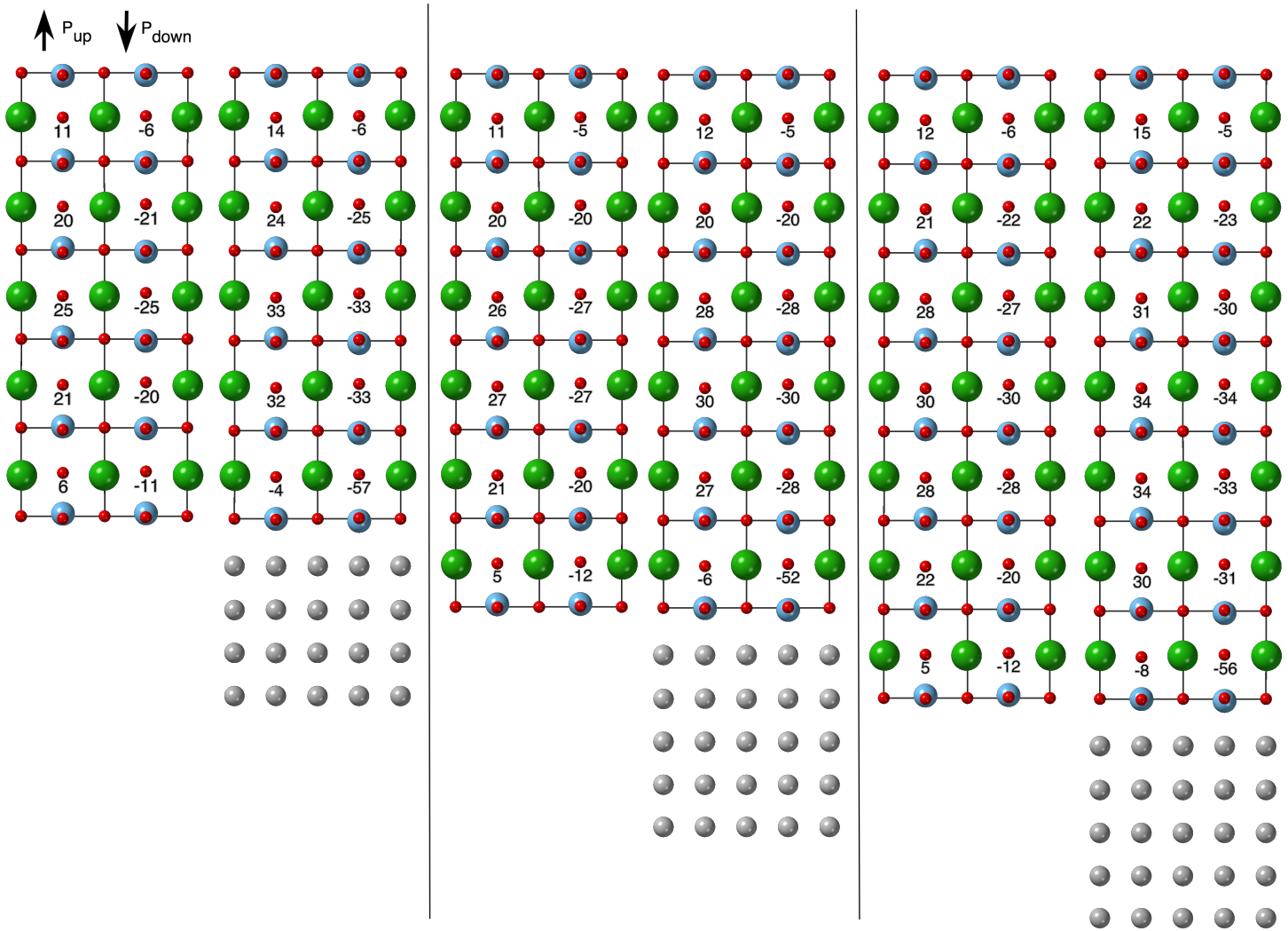

Figure 3.3 – Evolution of the local polarization as a function of BTO thickness for the two unit cell periodicity. From left to right, slabs of 11, 13 and 15 layers are considered. In each case, both strained BTO and BTO deposited on the Pt substrate are reported. Ba atoms are represented in green, Ti atoms in blue, O atoms in red and Pt atoms in gray. Values of local polarization in the out-of-plane direction are reported for each unit cell in $\mu C.cm^{-2}$.

atoms which can strongly modify the local ferroelectricity. It was already exposed for $KNbO_3$ capacitors by Tsymbal *et al.* [92] who showed that the bonds created between the substrate and the perovskite impose some movement restrictions for atoms at the boundaries, inducing a local polarization at the interface even for the paraelectric capacitors. Following these results, the atomic displacements of the first layer in the paraelectric phase were examined. It results that the Ti atoms of the first layer are pushed upwards by 0.06 Å towards the O atoms of the upper BaO layer in the presence of Pt. This displacement sustains in the ferroelectric phase which leads to an increase of the P_{down} polarization and a decrease of the P_{up} one causing neighboring cells to have the same polarization direction. To sum up, the bonding of ferroelectric BTO over the metallic substrate induces some disruptions on the polarization in the first deposited layers. Hence, it results a modification of the global polarization. In the presence of platinum, the global P_{up} is lowered while the global P_{down} is increased. It is also worth mentioning that the global polarization is independent of the slab thickness. As seen on Figure 3.3, in both isolated BTO and deposited BTO cases, as soon as the ferroelectric state becomes stable, the distribution of the polarization along the layers is identical whatever the total size of the slab.

3.4.2.3 Lateral periodicity

As it was demonstrated that Pt tends to stabilize larger polarization domains, it is also interesting to study the influence of the lateral periodicity on the polarization. The 11 layer slab is considered with three different periodicities, namely $N = 2$, 4 and 6. The local polarizations for the 4 and 6 unit cell periodicities are presented on Figure 3.4 and Figure 3.5, respectively, while Figure 3.6 represents qualitatively the same results together with those of $N = 2$ for a more visual comparison. In all cases, whatever the periodicity, platinum has always the same influence on the polarization. The same patterns than the ones previously described for the 2 unit cell periodicity are observed, meaning that there is a large asymmetry at the Pt/BTO interface, then the polarization values are close to the bulk polarization in the middle cells and finally the polarization in the neighboring upper cells is of opposite direction. The second important thing to note is that, contrary to the $N = 2$ case, higher periodicities allow the appearance of closure domains. Indeed, an in-plane component of the polarization along the [100] direction appears, especially in the surface layer and in the first sub-surface layer. The rotation of the local polarization near the surface towards the domain wall creates the formation of closure domains. This behavior is comparable to what Shimada *et al.* observed for $PbTiO_3$ [108]. These closure domains allow the system to decrease the discontinuity in $\vec{P}$ at the surface and thus its surface charge density by lowering the P_z component in favor of the P_x one. However, except at the Pt/BTO interface, the substrate does not have a large influence on the polarization patterns, for a given periodicity. As previously stated (see Figure 3.2), in the isolated BTO only the 2 and 4 unit cell periodicities are observed, whereas when deposited on Pt, larger periodicities are favored, generating larger

domains. The increase of lateral periodicity also leads to an increase of the local polarization (see Figure 3.6). Thus, when BTO is grown on Pt, larger domains with a higher polarization are expected.

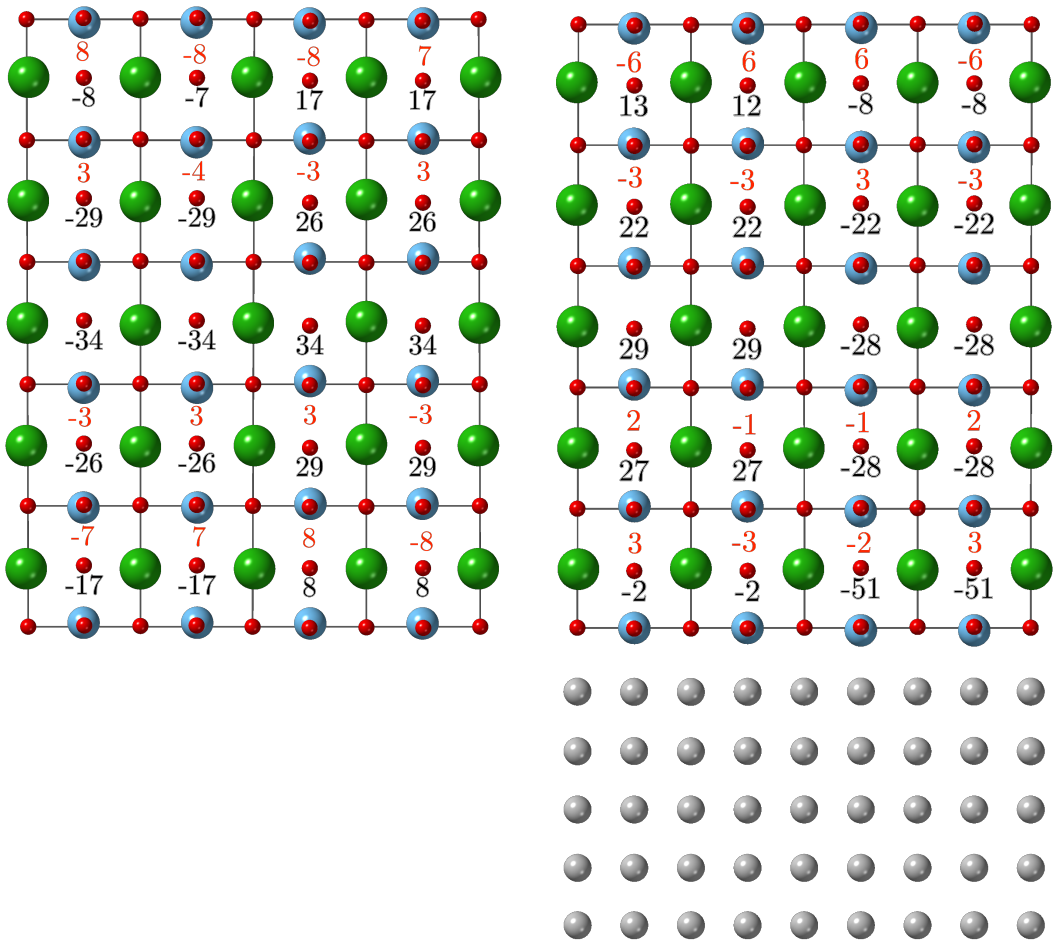

Figure 3.4 – Local polarizations in the case of $N = 4$ for (left) the isolated constrained BTO and (right) BTO deposited on Pt, for the 11 layer slab. Values in black and red represent the local polarization in $\mu C.cm^{-2}$ along [001] and [100], respectively. If no value is indicated, it means that it is null.

3.4.2.4 Influence of the upper termination

We showed in section 3.3 that as soon as the growth of BTO starts with a TiO_2 layer with the Ti atom located on the hollow site of Pt, the upper termination has no influence on the stability of the structure. Consequently, it is easy to imagine that, depending on the experimental conditions, both BaO and TiO_2 terminations can be formed. It thus appears crucial to examine whether the modification of the surface termination has some influence on the behavior of the polarization. To do so, the asymmetric [TiO_2/BaO] slab either isolated or deposited on Pt is compared to the reference [TiO_2/TiO_2] slab. To perform a thorough investigation, the isolated strained [BaO/BaO] slab is also considered even though it cannot

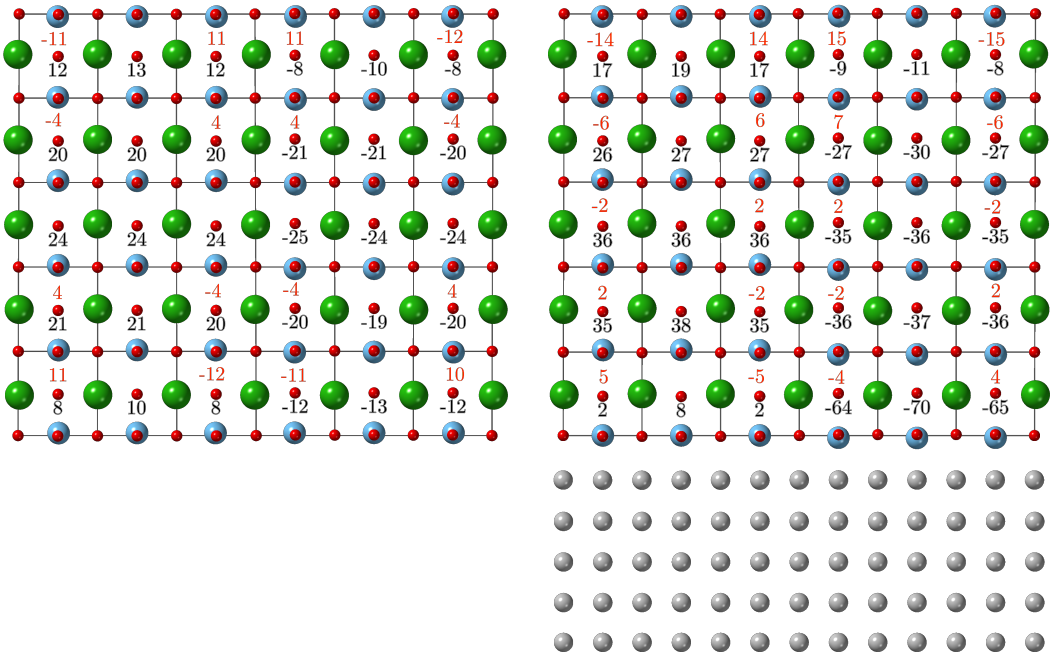

Figure 3.5 – Local polarizations in the case of $N = 6$ for (left) the isolated constrained BTO and (right) BTO deposited on Pt, for the 11 layer slab. Values in black and red represent the local polarization in $\mu C.cm^{-2}$ along [001] and [100], respectively. If no value is indicated, it means that it is null.

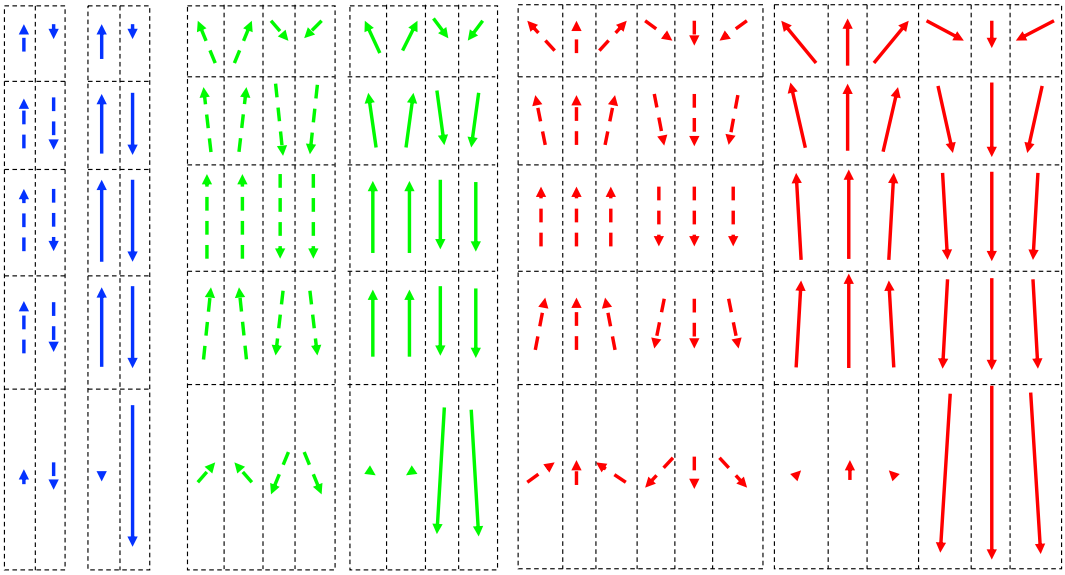

Figure 3.6 – Vectorial representation of the local polarization for two (in blue), four (in green) and six (in red) unit cell periodicities, for the 11 layer slab. Both isolated BTO (dotted arrows) and BTO deposited on Pt (plain line arrows) are reported. Black dotted cells are guidelines and they represent, without respect to the scale, the unit cells centered on an oxygen atom of a BaO layer, used for the calculation of local polarization. Cells in contact with Pt are the ones at the bottom of the picture, while the interface with the vacuum is at the top.

exist on platinum. In the BaO termination, the local polarization is calculated in the unit cell centered on Ti atoms. Regarding the asymmetric [TiO_2/BaO] slabs, this asymmetry prevents the decomposition of the slab in an integer number of unit cells. Thus, the decomposition was started from the top BaO surface layer as the interface vacuum/BTO is the region of interest here. Consequently, the unit cells used to calculate the local polarization were also centered on a Ti atom, as for the symmetric [BaO/BaO] slabs, and eventually the polarization at the Pt/BTO interface was not calculated as shown on Figure 3.7.

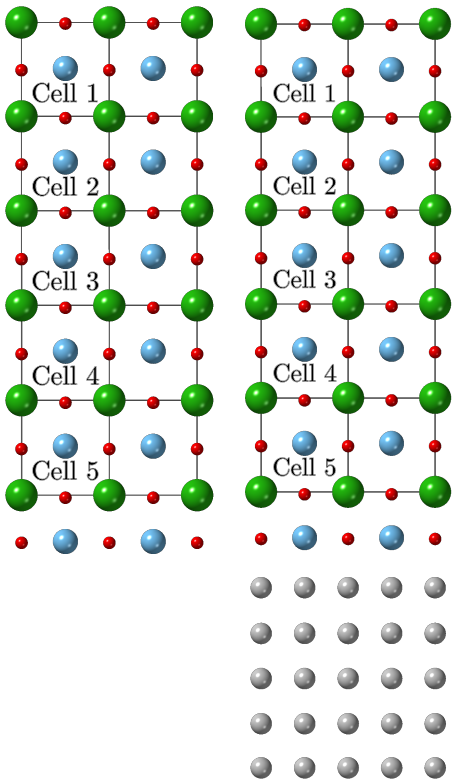

Figure 3.7 – Paraelectric 12 layer asymmetric [BaO/TiO_2] slab either isolated and strained on the left or deposited on platinum on the right. Ba atoms are represented in green, Ti atoms in blue, O atoms in red and Pt atoms in gray. the delimitation as well as the number of the cells used for the discussion are also reported.

The isolated strained systems are first considered. Figure 3.8 represents the local P_{up} and P_{down} polarizations for the first four surface unit cells (Cells 1 to 4 on Figure 3.7) of the 11 layer [TiO_2/TiO_2] and [BaO/BaO] slabs and of the 12 layer [TiO_2/BaO] slab. It shows that the polarization of the symmetric [BaO/BaO] slab is clearly the highest. This phenomenon is directly related to the chemical nature of the termination. In the case of BaO terminated surfaces, the unit cells recover the original nature of bulk BTO unit cells. Thus, the natural movement of the Ti atoms is favored, allowing a better amplitude of displacements. The increase of polarization is particularly true at the surface of the P_{down} side and in the center part of the slab. As for the [BaO/BaO] system, the polarization of

the strained bulk ($P_{strained}$(bulk)= 37 µC.cm^{-2}) is almost reached for the cell 3: P_{up}(cell 3) = $|P_{down}$(cell 3)| = 32 µC.cm^{-2}. These results indicate that the [BaO/BaO] structure has a higher polarization than the [TiO_2/TiO_2] one. Interestingly, this behavior partially remains for the asymmetric systems. Indeed, as seen on Figure 3.8, the [TiO_2/BaO] system exhibits an intermediate polarization between [TiO_2/TiO_2] and [BaO/BaO]. Again, the polarization of the middle cells is increased compared to symmetric TiO_2 systems, as well as the surface polarization of the P_{down} side.

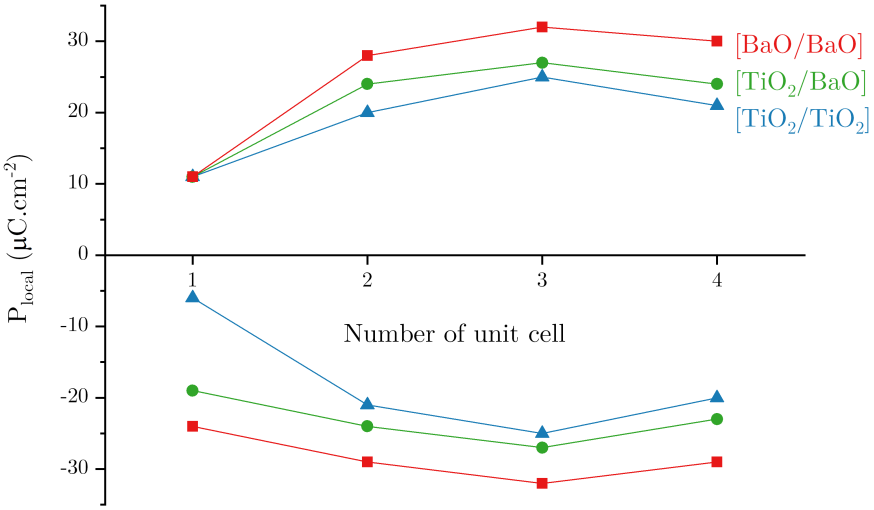

Figure 3.8 – Evolution of the local polarization (in µC.cm^{-2}) in the symmetric slabs of 11 layers with either two TiO_2 terminations (blue curves with triangles) or two BaO terminations (red curves with squares) and in asymmetric [TiO_2/BaO] slabs of 12 layers (green curves with circles). Only values for the first four cells starting from the BaO surface in the case of asymmetric slabs are reported. Positive values refer to the P_{up} side and negative to the P_{down} one.

Finally, the influence of the platinum substrate on the polarization of the asymmetric [TiO_2/BaO] films is evaluated. The results are presented on Figure 3.9. As for the symmetric [TiO_2/TiO_2] slab, Pt increases slightly the local polarization, especially in the bulk part of the slab.

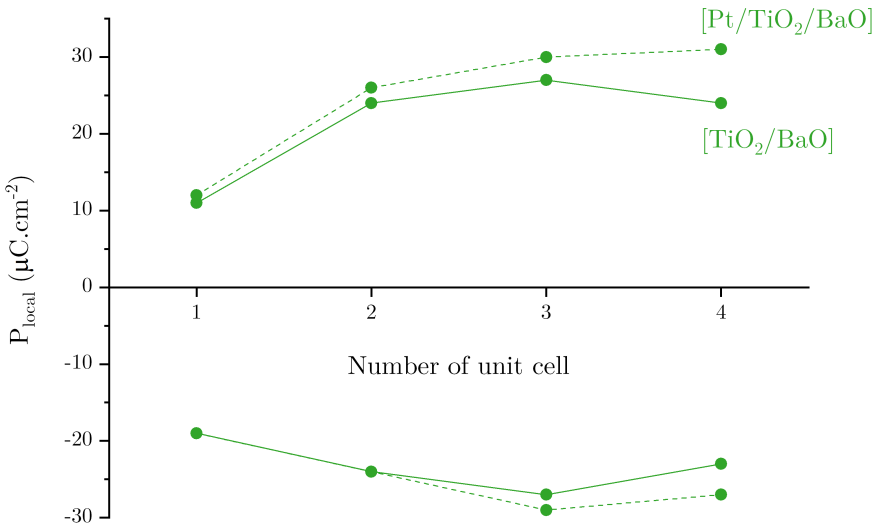

Figure 3.9 – Evolution of the local polarization (in µC.cm^{-2}) in asymmetric 12 layer [TiO_2/BaO] slabs either isolated (plain green curve) or deposited on platinum (dotted green curve). Only the values for the first four unit cells starting from the BaO interface with vacuum are reported. Positive values refer to the P_{up} side and negative to the P_{down} one.

These results indicate that both terminations can exist and suggest that they could have different behavior. It is therefore important to investigate both terminations from an experimental point of view as well. To this end, several samples were prepared with the aim of obtaining both surface terminations. They were further characterized by XPS to assess the surface state of the samples. The results are presented in the following section.

3.5 Experimental measurements

3.5.1 Samples

The samples were elaborated by our partners on this project at the Service de Physique de l'Etat Condensé (SPEC) at CEA-Saclay. They were prepared by oxygen plasma assisted molecular beam epitaxy (OPA-MBE), the detailed description of the apparatus and the deposition method can be found in Maxime Rioult's PhD thesis [21]. In short, OPA-MBE is a thin film growth technique operating in UHV conditions allowing the growth of epitaxial thin films with well controlled chemical and structural properties (stoichiometry, doping level, thickness, ...).

While it was initially planed to realize the experiments on BTO deposited on Pt(001), hence calculations were performed on Pt(001), sample size limitations on the synchrotron beamline prevented us to fit our platinum substrates. Therefore, it was decided to use smaller Nb:$SrTiO_3$ substrates instead. Indeed, this substrate also allows good epitaxy conditions for the growth of BTO as it induces a 2% compressive lattice mismatch (similar to Pt(001)) and possesses the same perovskite structure. Four BTO thin films were prepared on 0.5 at.% Nb:$SrTiO_3$ single crystalline substrates. The influence of the surface BTO termination was of primary concern in this study. Therefore, to tune the surface termination, either the Ba or the Ti Knudsen cell was stopped before the other allowing the deposition of a terminal TiO_2 or BaO layer, respectively. The deposition time of this final layer was set in order to obtain a single monolayer. The references of the samples used in the following with their respective termination and thickness are given in Table 3.3.

Reference	Surface termination	Thickness (nm)
$S_1(TiO_2)$	TiO_2	10
$S_2(TiO_2)$	TiO_2	16
$S_1(BaO)$	BaO	10
$S_2(BaO)$	BaO	16

Table 3.3 – References of the BTO samples with their surface termination and thickness.

3.5.2 Characterization

The thorough characterization of a thin film is a very demanding work. Indeed, one has to determine, for instance, the nature of the substrate/overlayer interface as well as the nature of the surface termination. These features can be monitored by means of X-ray surface diffraction or X-ray Photoelectron Diffraction (XPD) which usually requires the combination of DFT calculations and multiple scattering calculations to refine the obtained structures. However, this implies long time effort and is a full study on its own [126]. In this work, we decided to unravel the nature of the interfaces using DFT calculations. As shown above, both surface terminations could exist as they present a similar stability. Therefore, their existence was checked using XPS in conditions favoring as much as possible the surface sensitivity.

3.5.2.1 Chemistry

The samples were investigated by photoemission spectroscopy on the MATLINE beamline of the synchrotron ASTRID II. The photon energy was 160 eV in order to increase the surface sensitivity of the experiment. Additionally, spectra were recorded both at normal take-off angle and at grazing take-off angle to further increase the surface sensitivity. Indeed, it is well known that the effective sampling depth (z), corresponding to 95% of the signal, is a function of the mean inelastic free path (λ) and the take-off angle (θ) as $z = 3\lambda \times sin\ \theta$. This means

that at lower take-off angle, only the electrons emitted from the region near the surface are detected. Figure 3.10a and Figure 3.10b display typical XPS spectra of barium 4*d* core level acquired at normal angle and at grazing angle, respectively. They exhibit two components for each spin-orbit peak. The low binding energy component (in red) corresponds to the bulk coordinated Ba, referred to as Ba(α). On the other hand, the high binding energy component (in blue) is attributed to under coordinated Ba in the region of the sample surface, referred to as Ba(β) [127–130]. Indeed, it is clear that when the take-off angle is lower, hence the surface sensitivity increased, the Ba(β) intensity increases.

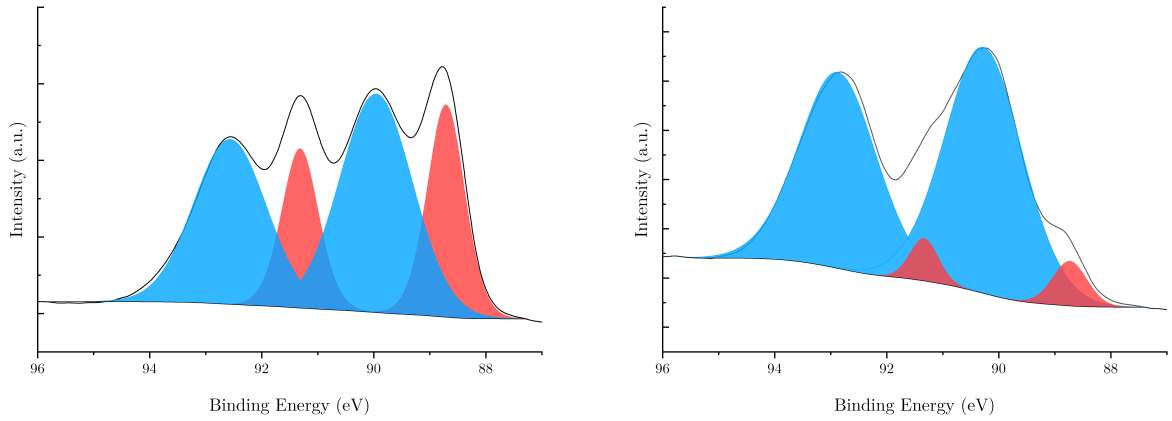

(a) Normal angle (b) Grazing angle

Figure 3.10 – XPS spectra of the Ba 4*d* core level for a 10 nm thick $BaTiO_3$/Nb:$SrTiO_3$ sample acquired with a photon energy of 160 eV at (a) normal take-off angle and (b) grazing take-off angle. Red components are Ba(α) components whereas blue components are Ba(β) components.

The samples were analyzed *in situ* after the growth by Auger Electron Spectroscopy (AES) in order to assess the surface composition of the BTO thin film. They were also characterized by XPS after annealing at 400°C under O_2 pressure of 10^{-6} hPa for 1h. XPS acquisition was performed both at normal angle and grazing angle for each sample. The raw intensity ratios of the Ba 4*d* and Ti 3*p* peaks are reported as a function of the raw intensity ratios of the Ba_{MNN} and Ti_{LMM} Auger transitions on Figure 3.11. It clearly shows that the TiO_2-terminated thin films have a lower Ba/Ti ratios both in AES and XPS, hinting that the surface termination was indeed tuned as expected. Moreover, the Ba(α)/Ti ratio are equivalent for each sample which indicates that they all have a similar bulk composition. When it comes to the Ba(β)/Ti ratios, it is significantly higher in the case of the BaO-terminated films both at normal and grazing angle, suggesting that the last BaO layer was effectively deposited on the surface of the sample.

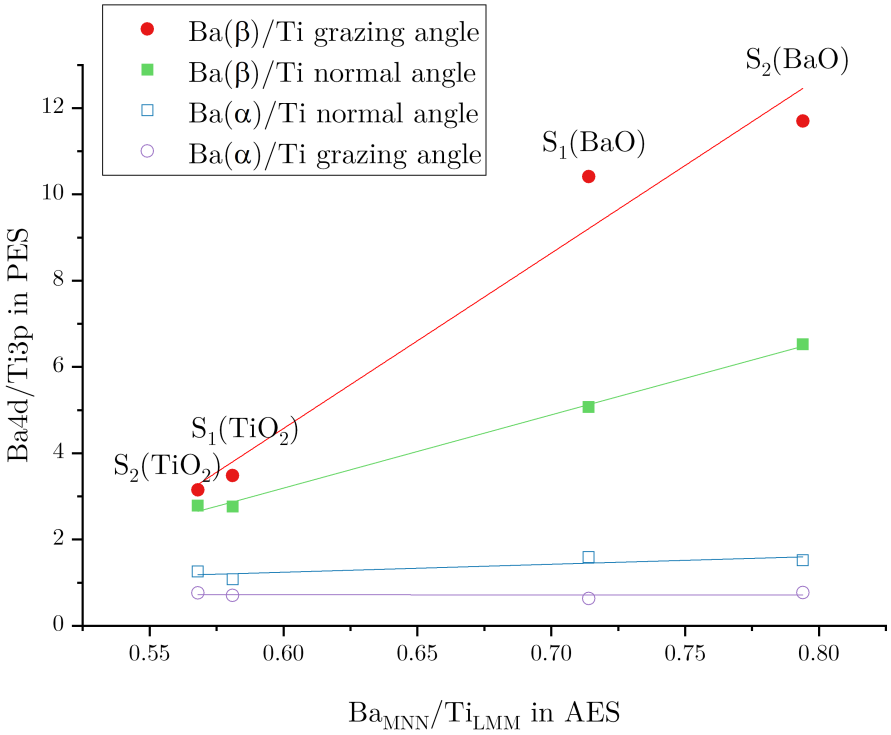

Figure 3.11 – Raw intensity ratios of the Ba $4d$ and Ti $3p$ peaks as a function of the raw intensity ratios of the Ba and Ti Auger transitions for each studied sample. The red and green curves show the Ba(β)/Ti ratios acquired at grazing and normal angle, respectively. The blue and purple curves shows the Ba(α)/Ti ratios acquired at grazing and normal angle, respectively.

Another interesting feature of the XPS spectra comes from the Ba $5s$ peak. It was recorded in the same conditions than the Ba $4d$ spectra. Figure 3.12 shows the Ba $5s$ spectra for the four samples at grazing angle. In the TiO_2-terminated samples, the peak can be fitted with only one component while in the case of the BaO-terminated films, a second component appears. It is worth noting that this second component, probably surface related, appears at a lower binding energy while for the Ba $4d$ core level, the surface related Ba(β) is at a higher binding energy than the bulk related Ba(α). This splitting of the Ba $5s$ line could be characteristic of a BaO-terminated BTO and could therefore be useful to determine the surface termination.

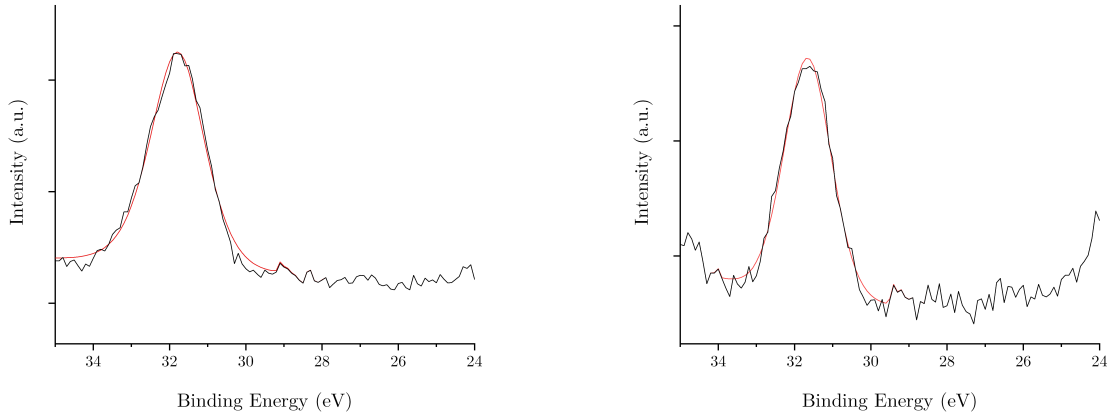

(a) $S_1(TiO_2)$

(b) $S_2(TiO_2)$

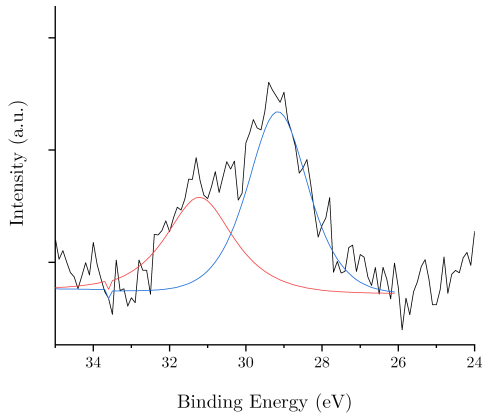

(c) $S_1(BaO)$

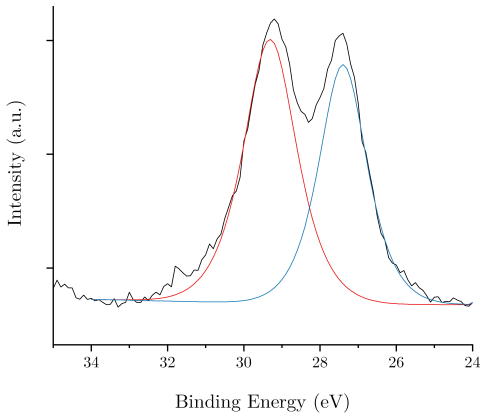

(d) $S_2(BaO)$

Figure 3.12 – XPS spectra of the Ba 5*s* peak recorded at grazing take-off angle with a photon energy of 160 eV for (a) $S_1(TiO_2)$, (b) $S_2(TiO_2)$, (c) $S_1(BaO)$ and (d) $S_2(BaO)$.

3.5.2.2 Polarization

In the case of a ferroelectric material, the polarization in the film should be analyzed. Experimentally, it is very tricky to carefully measure the polarization. One commonly used method to detect or apply polarization states in a ferroelectric material is Piezoelectric Force Microscopy (PFM). It is a scanning probe microscopy technique which records the piezoelectric deformations of the sample when it is submitted to the electric field induced by a tip. However, the measurement is usually performed *ex situ*, meaning that the sample is subject to ambient contamination which can modify the polarization. Additionally, being a scanning probe microscopy technique implies that only a small area (in the order of the μm^2) of the sample can be analyzed. Figure 3.13 shows the ferroelectric state of a typical as grown BTO sample. A pattern (Figure 3.13a) is written on the sample surface by applying different voltages ($\pm$ 8V) on the surface. A positive bias induces a downward polarization

whereas a negative voltage generates an upward polarization. PFM is then used in reading mode (Figure 3.13b) to compare the phase of the written pattern to the background of the sample [131]. In the example shown here, there is very few contrast between the +8V written region and the native region, indicating that, for this sample, BTO initially presents mainly a downward polarization. Even though qualitative results are rather easy to obtain, quantitative measurements require careful calibrations and are heavily dependable on the environment. Hence, DFT calculations are a very useful tool to determine quantitative values of polarization in controlled conditions.

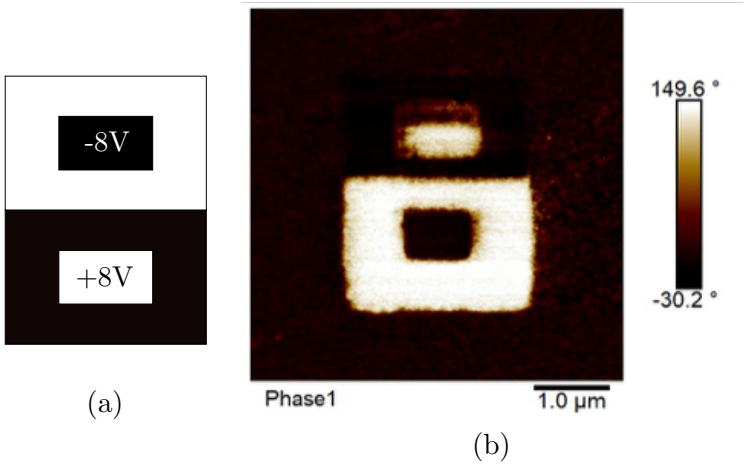

(a) (b)

Figure 3.13 – PFM measurement performed on a 10 nm thick $BaTiO_3$/Nb:$SrTiO_3$ sample. (a) PFM written pattern and (b) PFM phase image in reading mode after writing the pattern pictured in (a).

3.5.3 Effect of the temperature

As discussed previously, temperature is an important factor when considering ferroelectric materials as it induces a phase transition from the ferroelectric to the paraelectric phase. In the case of BTO, this phase transition occurs around 130°C or even higher in thin films. Therefore, we decided to investigate the influence of the temperature on the XPS spectra. To this end, the Ba 4*d* and Ti 3*p* peaks were recorded with a photon energy of 160 eV at grazing take-off angle at a temperature ranging from room temperature to 300°C. The evolution in the XPS spectra is analyzed through the difference between the Ba 4*d* and Ti 3*p* line binding energies (ΔE) compared to the average difference measured for all temperatures, according to:

$$\Delta E = (Ba - Ti)_T - m(Ba - Ti)_{T_n} \tag{3.5}$$

where (Ba-Ti)$_T$ is the difference in binding energy between the Ba 4*d* and Ti 3*p* peaks at the given temperature and $m(Ba - Ti)_{T_n}$ is the average of the difference in binding energy

between the Ba 4*d* and Ti 3*p* peaks at every measured temperature. Figure 3.14a displays the results for the Ba(α) component, thus mainly related to the bulk region of the film, while Figure 3.14b shows the results for the Ba(β) component and is therefore mainly linked to phenomena at the surface region of the sample.

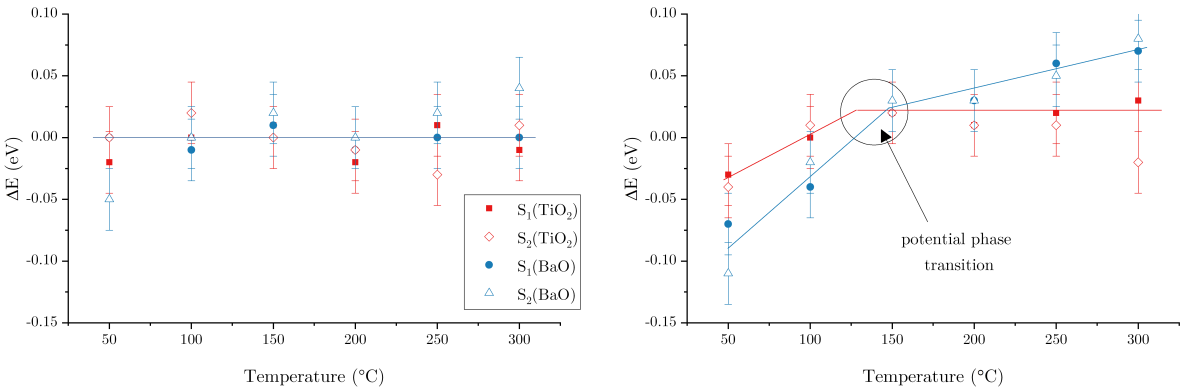

(a) Ba(α)-Ti 3*p* (b) Ba(β)-Ti 3*p*

Figure 3.14 – Evolution of the difference between the Ba 4*d*-Ti 3*p* line binding energies as a function of the temperature for (a) the Ba(α) component and (b) the Ba(β) component. The symbols are the same in both figures. The solid lines are only guides to the eye.

Let's first consider the Ba(α) component. For the four samples, no clear shift in the difference between Ba 4*d* and Ti 3*p* line binding energies is observed in the considered temperature range. On the contrary, regarding the Ba(β) component, clear shift of the energy difference is observed. For the TiO_2 terminated samples, it seems that the Ba(β)-Ti 3*p* binding energy difference is shifted towards higher energies until about 130-150°C and is then constant up to 300°C. The BaO-terminated samples exhibit a similar trend until about 150°C as well. However, in this case, ΔE continues to increase at least until 300°C but with a lower slope. It is interesting to note that for each of the four samples a discontinuity in ΔE evolution appears at a temperature close to the potential ferroelectric to paraelectric phase transition. This result suggests that XPS could potentially be used to evidence a phase transition. As a shift is only measured when considering the Ba(β) component, the phenomenon inducing the shift is probably surface related. It might also originate from the desorption of hydroxyl groups due to the increase of the temperature and therefore modify the chemical environment of the surface atoms, inducing a shift in their core level binding energy. The adsorbed OH groups could as well induce a modification of the polarization of the first surface layers and their desorption would modify the surface polarization which in turn would translate in a shift of the core level binding energies.

3.6 Outline

We showed that the growth of $BaTiO_3$(001) on Pt(001) starts with a TiO_2 layer with Ti atoms in hollow positions, and oxygen atoms on top of platinum. Under the 2.1% compressive strain induced by the lattice mismatch between BTO and the Pt substrate, ferroelectric slabs of BTO are stabilized over paraelectric ones for thicknesses larger than 23 Å, corresponding to 11 layers. Above this thickness, all symmetric [TiO_2/TiO_2] slabs present the same evolution of local polarization. The local polarization at the surface is lower than the one inside the slab, which tends to the strained bulk polarization.

The presence of the platinum substrate induces several modifications on the BTO overlayers. From an energetic point of view, platinum has two consequences. First, it increases the stability of ferroelectric slabs over paraelectric ones and allows the stabilization of the ferroelectric phase at lower thicknesses. When deposited on Pt, the ferroelectric phase is observed from 9 layers for domain widths of two unit cells or more. Secondly, the substrate changes the preferential size of the domains. While for isolated BTO, the smaller 2 or 4 unit cell periodicities are favored over larger ones, in presence of Pt, larger domains will be obtained. Regarding the polarization, at a given periodicity, both deposited and isolated BTO slabs show a similar qualitative behavior. Nevertheless, from a quantitative point of view, three differences have to be noted. Firstly, the stability of ferroelectric slabs over paraelectric ones is increased in presence of platinum. Secondly, the local polarization is modified at the Pt/BTO interface because of Pt-O bonding. Thirdly, the local polarization of central unit cells is increased in the presence of platinum. Another important change due to the presence of platinum is the kind of observed domains. As larger cells are favored for overlayers, larger domains with clearer closure walls will be observed.

Finally, the influence of the upper termination on the polarization was also analyzed through the study of asymmetric [TiO_2/BaO] slabs. It showed that the presence of an upper BaO termination induces an increase of not only the local polarization in the middle cells, but also of the surface polarization of the P_{down} side.

We also demonstrated that it is possible to experimentally tune the surface termination of the BTO overlayer by switching off an evaporation cell before the other. XPS is a suitable technique to characterize the surface of the thin film. Indeed, the splitting of the Ba $4d$ peak into two components characteristic of either the volume (Ba(α)) or surface (Ba(β)) region of the sample is particularly useful. It also seems that a splitting of the Ba $5s$ peak, not discussed in the literature, appears when the sample is terminated by a final BaO layer while this is not the case for the TiO_2 termination. This allowed to show that the volume part of the BTO film is equivalent in all 4 samples whereas the surface differs depending on

the desired termination. Therefore, these samples are suited to study the influence of the termination on water adsorption as presented in the following chapter.

Furthermore, the XPS study of the ferroelectric film as a function of the temperature indicates that XPS could allow to evidence a ferroelectric phase transition. Indeed, a modification in the Ba $4d$-Ti $3p$ binding energy difference, suggesting a modification of the chemical environment of the ions, is observed at a temperature similar to the potential phase transition of BTO.

Chapter 4

Water adsorption on $BaTiO_3$(001)

In the following part, the adsorption of water on $BaTiO_3$ (001) is discussed. First, a theoretical study is presented. It aims at investigating in details both molecular and dissociative adsorption of water on out-of-plane polarized $BaTiO_3$ (001) with different water coverages and different domain widths. The influence of the polarization as well as the surface termination is particularly described. To corroborate the results, experiments were conducted.

4.1 First-principles results

Even though we showed in the previous chapter that the platinum substrate does not extensively modify the surface polarization of BTO, it is mandatory to verify if Pt has to be implemented in the calculation slab to properly describe the water adsorption behavior on the interface Pt/BTO. Hence, water is adsorbed either on the isolated strained BTO or on BTO deposited on Pt. It was demonstrated in section 3.3 that both BaO and TiO_2 surface terminations can co-exist, thus water adsorption is studied for both terminations. Similarly to the previous chapter, the substrate is modeled with 5 layers, the bottom 2 layers being fixed to the experimental lattice parameter of Pt. In the case of isolated BTO, symmetric slabs containing 11 layers are considered. When considering BTO deposited on Pt, 10 and 11 layers of BTO are used to model the asymmetric BaO-terminated and symmetric TiO_2-terminated slabs, respectively. The water coverage is tuned by changing the lateral periodicity N and the number of water molecules adsorbed per unit cell. The surface area of the strained (001) unit cell is approximately 15.4 $Å^2$, while the cross section area of a water molecule is about 7-8 $Å^2$, thus two water molecules are sufficient to form a monolayer. Here, water coverages of $\frac{1}{8}$, $\frac{1}{4}$ and $\frac{1}{2}$ monolayers (ML) are envisaged. In each case, to investigate the behavior of water adsorption as a function of the polarization, water is adsorbed either on the upward polarized domain, on the downward polarized domain or on the paraelectric phase. Moreover, on the isolated BTO structures, water is adsorbed only on one side of the slab.

The adsorption energy is defined as:

$$E_{ads} = E(slab + H_2O) - E(slab) - E(H_2O) \tag{4.1}$$

where $E(slab + H_2O)$ is the total energy of the optimized slab with one water molecule adsorbed, $E(slab)$ is the total energy of the optimized paraelectric slab without water and $E(H_2O)$ is the total energy of the free water molecule. Therefore, a negative value of E_{ads} means that the adsorption is favorable. When two water molecules are adsorbed, if both molecules cannot be distinguished, the average adsorption energy is considered. Oppositely, if the adsorption of the two molecules differs, the adsorption energy of the first water molecule is calculated with equation 4.1 and the value is referred to as E^1_{ads}. The adsorption energy of the second molecule is calculated as:

$$E^2_{ads} = E(slab + 2H_2O) - E(slab + H_2O) - E(H_2O) \tag{4.2}$$

where $E(slab + 2H_2O)$ is the total energy of the optimized slab with two water molecules adsorbed, $E(slab + H_2O)$ is the total energy of the optimized slab with a single water molecule and $E(H_2O)$ is the total energy of the free water molecule.

In the following, the length of the hydrogen bond of the water molecule which is in contact with the surface is called OH_W while the distance between the surface oxygen and the hydrogen of the water molecule is named OH_S (see Figure 4.1).

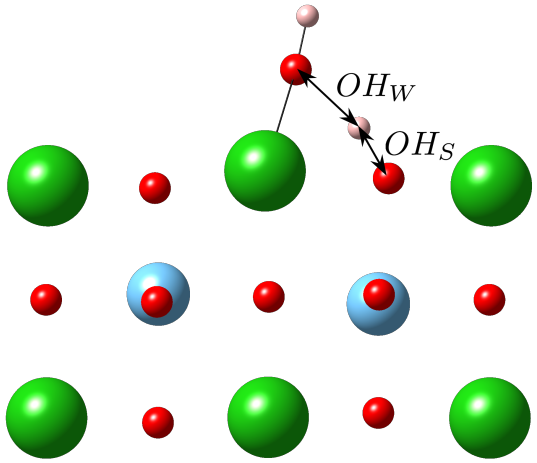

Figure 4.1 – Sideview of the first three layers of a BaO-terminated slab with a water molecule adsorbed showing the characteristic distances OH_W and OH_S as defined in the text.

4.1.1 Adsorption modes

4.1.1.1 BaO termination

First, the adsorption of water on the BaO termination is discussed for coverage ranging from $\frac{1}{8}$ ML to $\frac{1}{2}$ ML. The following nomenclature is used to refer to the stable configurations: X_θ^N where θ indicates to the coverage ($\frac{1}{8}$, $\frac{1}{4}$ or $\frac{1}{2}$ ML), N is the lateral periodicity (2 or 4) and X takes values A, B, C, ... to differentiate configurations with identical θ and N. Different configurations are envisaged as initial states according to the literature [132, 133], each on the three polarization states (paraelectric, P_{up} and P_{down}). The adsorption energies are reported on Table 4.1. It shows that the adsorption energies are not extensively modified by the Pt substrate. The only noticeable difference is observed for the adsorption of the first molecule on the surface with a periodicity of 4 unit cells. The adsorption energy is increased by approximately 0.1 eV in the case of BTO deposited on Pt compared to the isolated BTO. This small discrepancy is partially due to the difference of stabilization of the ferroelectric phase previously observed between isolated BTO and BTO deposited on Pt. Indeed, as the adsorption energy is calculated with the paraelectric phase as a reference, it also includes a ferroelectric stabilization term. However, the geometry of the adsorbed water molecule is not modified by the presence of platinum as the bond lengths and angles are identical in both isolated and deposited BTO. Consequently, in the following, water adsorption will be discussed only in the case of the isolated BTO.

			Isolated BTO		Pt/BTO	
Coverage	Periodicity	Configuration	E_{ads}^1	E_{ads}^2	E_{ads}^1	E_{ads}^2
$\frac{1}{8}$ ML	$N=4$	$A_{1/8}^4$	-1.12	-	-1.24	-
		$B_{1/8}^4$	-1.15	-	-1.25	-
$\frac{1}{4}$ ML	$N=2$	$A_{1/4}^2$	-1.09	-	-1.08	-
		$B_{1/4}^2$	-1.08	-	-1.06	-
	$N=4$	$A_{1/4}^4$	-1.07		-1.13	
		$B_{1/4}^4$	-1.08		-1.13	
		$C_{1/4}^4$	-1.04		-1.10	
		$D_{1/4}^4$	-1.09		-1.14	
		$E_{1/4}^4$	-1.15	-0.95	-1.25	-0.95
		$F_{1/4}^4$	-1.12	-0.96	-1.25	-0.98
		$G_{1/4}^4$	-1.15	-0.97	-1.25	-0.95
$\frac{1}{2}$ ML	$N=2$	$A_{1/2}^2$	-1.09	-0.90	-1.08	-0.86
		$B_{1/2}^2$	-1.08	-0.96		
		$C_{1/2}^2$	-1.09	-0.79	-1.08	-0.75

Table 4.1 – Water adsorption energies in eV on the BaO termination for isolated BTO and BTO deposited on Pt as a function of the water coverage. As defined in the text, E_{ads}^1 refers to the adsorption of the first water molecule and E_{ads}^2 to the second molecule. When both water molecules are equivalent, only the average adsorption energy is given.

First, a single water molecule is adsorbed on the surface with $N = 4$ to model the lowest coverage ($\frac{1}{8}$ ML). Figure 4.2 shows the two most stable structures obtained after optimization. Whatever the initial polarization, the structures converge in these two configurations. It is clear that the adsorption only occurs on the downward polarization regardless of the initial polarization. This phenomenon will be discussed in details later.

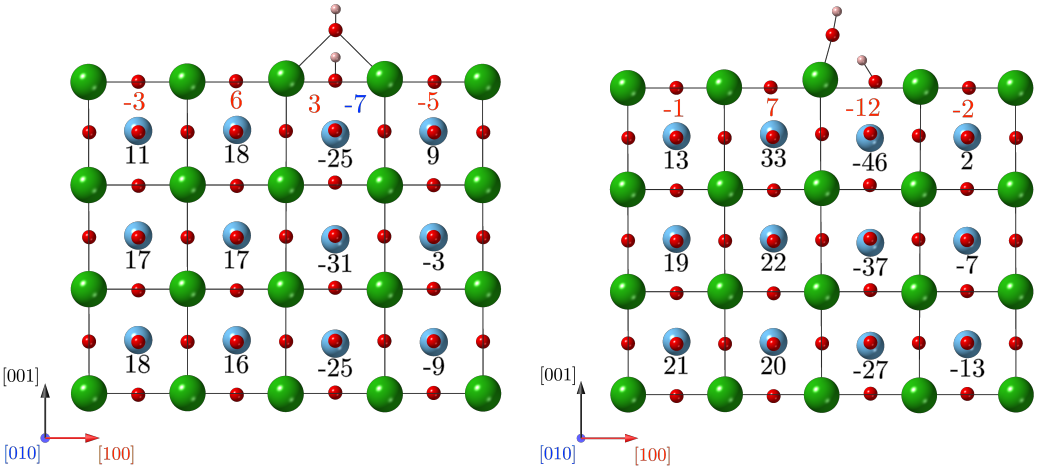

(a) $A^4_{1/8}$ (b) $B^4_{1/8}$

Figure 4.2 – Sideviews of the most stable structures of the BaO-terminated surface with $N = 4$ and $\theta = \frac{1}{8}$ ML. Only the first seven layers are represented for sake of clarity. The values in black, blue and red indicate the polarization in $\mu C.cm^{-2}$ in each unit cell along the [001], [010] and [100] directions, respectively. If no value is mentioned it means that the polarization along the given direction is equal to zero.

Two configurations are found where water spontaneously dissociates into a H^+ which bonds with a surface O ion and a hydroxyl group that binds between two Ba ions either in the (100) or (101) plane, referred to as $A^4_{1/8}$ and $B^4_{1/8}$ with adsorption energies of -1.14 eV and -1.12 eV, respectively. In the following, whatever the coverage, the adsorption with a configuration like the one of $A^4_{1/8}$ will be referred as Mode 1, while adsorption like $B^4_{1/8}$ will be called Mode 2. In $A^4_{1/8}$, OH_S is 1.05 Å and OH_W 1.48 Å while in $B^4_{1/8}$ OH_S and OH_W are 1.02 Å and 1.57 Å. These results are very similar to the ones found in previous studies. Indeed, the $A^4_{1/8}$ configuration discussed here is similar to the dissociative adsorption observed by Geneste *et al.* [132] who investigated water adsorption on in-plane polarized BTO. However, they calculated a lower adsorption energy of -0.77 eV. Though this discrepancy can partially be due to the difference of our level of calculation as we have included dispersion corrections which reinforce hydrogen bonds, it does not fully explain the difference of 0.35 eV. Indeed, without dispersion corrections, the adsorption energy of $A^4_{1/8}$ is lowered from -1.12 to -0.98 eV, which is still 0.21 eV higher than when water is adsorbed on in-plane polarized BTO. Therefore, the out-of-plane polarization in BTO clearly increases the interaction with water. Additionally, this can be the reason why we only observe dissociative adsorption on BaO ter-

mination while previous studies [132, 133], without inclusion of dispersion nor out-of-plane polarization, were able to stabilize molecular water on BaO. With that in mind, the molecular adsorption state found by Geneste *et al.* [132] with an adsorption energy of -0.72 eV can be seen as a precursor of our dissociative $B^4_{1/8}$ configuration.

Then, two different methods are used to increase the water coverage to $\frac{1}{4}$ ML. This is done either by adding a second molecule to the $\frac{1}{8}$ ML case or by considering a single water molecule on a unit cell with a lateral periodicity of 2 unit cells ($N = 2$). Regarding the latter case, the results are very similar to the $\frac{1}{8}$ ML coverage presented above. The optimized configurations are displayed on Figure 4.3 while the corresponding adsorption energies are reported in Table 4.1. The geometries are almost identical to the $\frac{1}{8}$ ML coverage as OH_S and OH_W are not modified over 0.05 Å. The only difference lies in the adsorption energies which are a bit reduced at this higher coverage. It slightly decreases from -1.15 and -1.12 eV at $\theta = \frac{1}{8}$ ML to -1.09 and -1.08 eV at $\theta = \frac{1}{4}$ ML, as a consequence of lateral interactions.

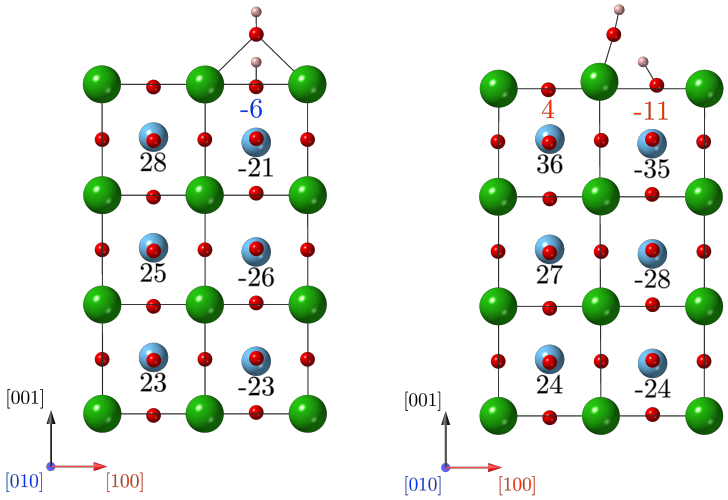

(a) $A^2_{1/4}$ (b) $B^2_{1/4}$

Figure 4.3 – Sideviews of the most stable structures of the BaO-terminated surface with $N = 2$ and $\theta = \frac{1}{4}$ ML.

When the $\frac{1}{4}$ ML coverage is achieved through the adsorption of two water molecules on the surface with a periodicity of $N = 4$, different possibilities arise. The second molecule can either be adsorbed on the same unit cell than the first one or on another unit cell, adjacent or not. The most stable configurations can be split in two categories depending on whether the second molecule dissociates (Figure 4.4) or molecularly adsorbs (Figure 4.5) on the surface. The adsorption energy is slightly more favorable when the second molecule dissociates which suggests that water is more inclined to dissociate on the BaO termination as previously observed [133]. Nevertheless, the adsorption energies in the mixed adsorption structures are very close, so each configuration is likely to exist. If the second molecule adsorbs on

the surface without interacting with the first one, it spontaneously dissociates in the same geometry than the previously observed structures. Regarding the mixed adsorption case (Figure 4.5), the second water molecule maintains its molecular form with its H bonded to the O atom of the first water molecule through a hydrogen bond. The length of the hydrogen bond is 1.59 Å in $E^4_{1/4}$ and 1.52 Å in $F^4_{1/4}$. This interaction causes the first molecule to be even more distorted. Indeed, in $E^4_{1/4}$ OH_W stretches from 1.57 to 1.99 Å and from 1.48 to 1.65 Å in $F^4_{1/4}$. Additionally, in $E^4_{1/4}$ the first water molecule is pulled by the second through the hydrogen bond. This causes the second hydrogen bond (OH_W) to pull the O ion out of the surface by 0.52 Å which leads to a much larger out-of-plane polarization in the first surface layers. In $G^4_{1/4}$, the second water molecule is adsorbed in a configuration similar to Mode 2 but less bonded to the surface, leading to a non dissociated configuration. Therefore, the O of the water is bonded to two Ba atoms at a distance of 3.01 Å instead of 2.71 Å and OH_S is not a real O-H bond as in Mode 2, where $OH_S = 1.02$ Å but a hydrogen bond of 1.47 Å.

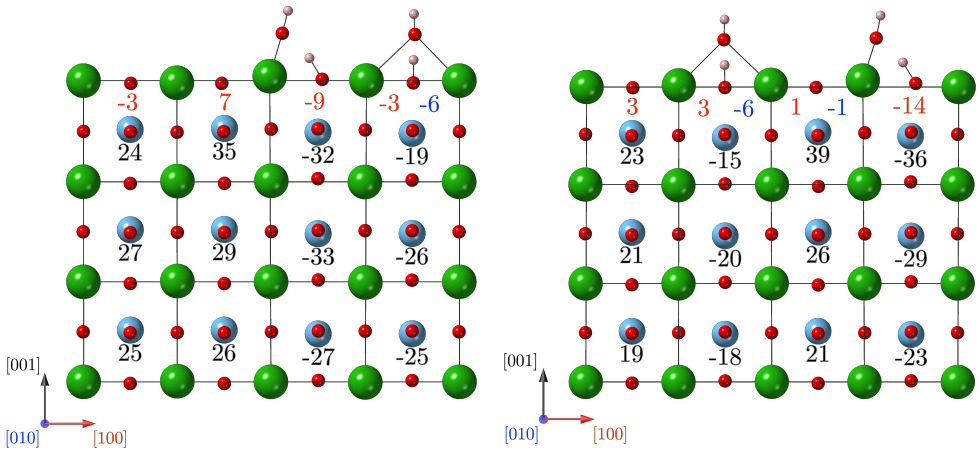

(a) $A^4_{1/4}$

(b) $B^4_{1/4}$

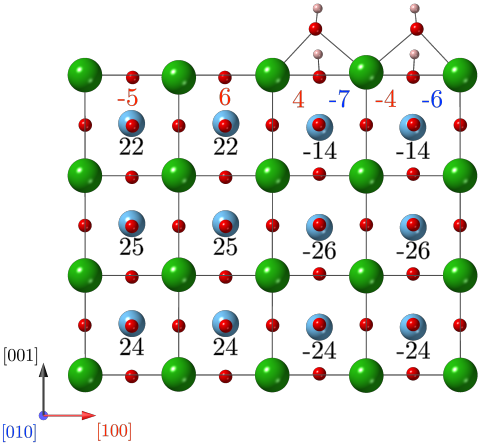

(c) $C^4_{1/4}$

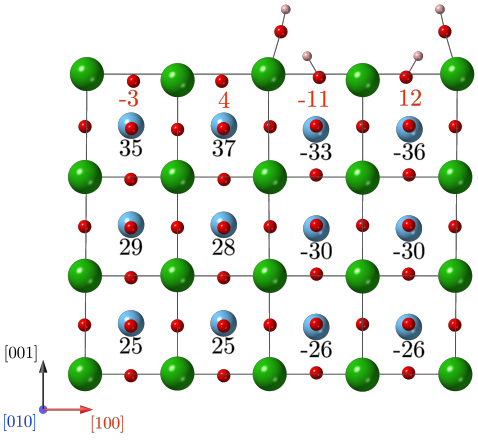

(d) $D^4_{1/4}$

Figure 4.4 – Sideviews of the most stable structures of dissociated water on the BaO-terminated surface with $N = 4$ and $\theta = \frac{1}{4}$ ML.

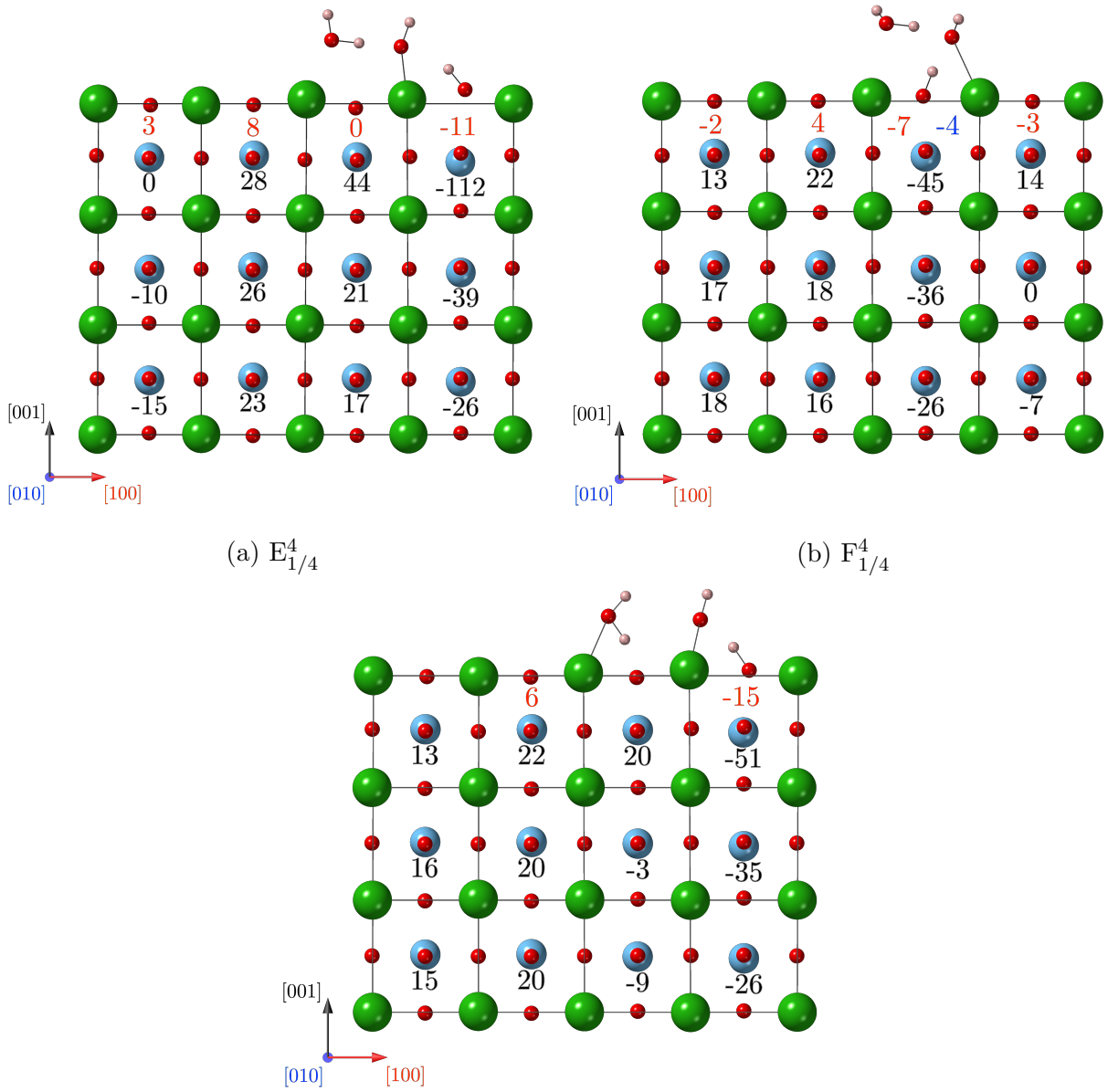

(a) $E^4_{1/4}$

(b) $F^4_{1/4}$

(c) $G^4_{1/4}$

Figure 4.5 – Sideviews of the most stable structures of the mixed adsorption cases on the BaO-terminated surface with $N = 4$ and $\theta = \frac{1}{4}$ ML.

Finally, the highest considered coverage is half a monolayer. To obtain this coverage, a second water molecule is added to the $\frac{1}{4}$ ML coverage with a $N = 2$ periodicity. The most stable structures are shown on Figure 4.6. In all the obtained cases, the second molecule molecularly adsorbs on the surface. However, the adsorption is more favorable when both molecules are on the same downward polarized domain. In such cases, the interaction between both molecules leads to a larger distortion of the first molecule as OH_W stretches from 1.45 to 1.60 Å in $A^2_{1/2}$ and from 1.52 to 1.61 Å in $B^2_{1/2}$. This behavior was already observed by Li *et al.* when studying water adsorption on in-plane polarized BTO [133].

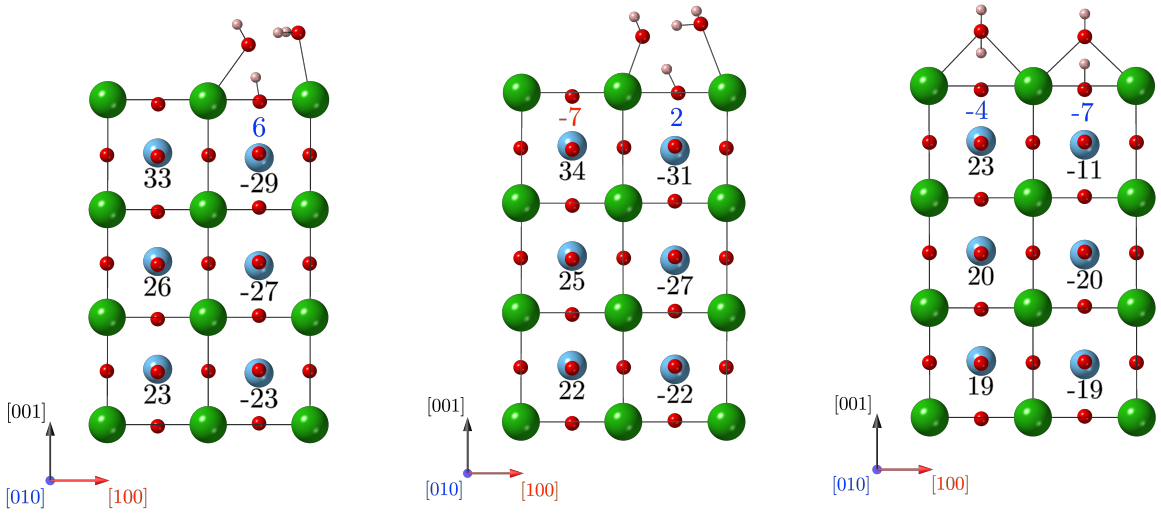

(a) $A^2_{1/2}$ (b) $B^2_{1/2}$ (c) $C^2_{1/2}$

Figure 4.6 – Sideviews of the most stable structures of the BaO-terminated surface with $N = 2$ and $\theta = \frac{1}{2}$ ML.

4.1.1.2 TiO_2 termination

Let us now discuss the behavior of water adsorption on the TiO_2 termination. The same coverages are considered than for the BaO termination. Additionally, water is also initially adsorbed either on the upward or the downward polarized domain as well as on the paraelectric slab. Contrary to the BaO termination, water induces the formation of upward polarized domains on the TiO_2-terminated BTO. The polarization of the obtained configurations will be discussed in details further. The optimized configurations for the two lower coverages, namely $\theta = \frac{1}{8}$ ML and $\theta = \frac{1}{4}$ ML are reported in Figure 4.7 and their corresponding adsorption energies are presented in Table 4.2.

			Isolated BTO		Pt/BTO	
Coverage	Periodicity	Configuration	E^1_{ads}	E^2_{ads}	E^1_{ads}	E^2_{ads}
$\frac{1}{8}$ ML	$N = 4$	$A^4_{1/8}$	-0.98	-	-1.10	-
$\frac{1}{4}$ ML	$N = 2$	$A^2_{1/4}$	-0.97	-	-0.96	-
	$N = 4$	$A^4_{1/4}$	-0.97		-1.03	
$\frac{1}{2}$ ML	$N = 2$	$A^2_{1/2}$	-0.97	-0.99	-0.96	-0.99
		$B^2_{1/2}$	-0.94		-0.94	

Table 4.2 – Water adsorption energies in eV on the TiO_2 termination for isolated BTO and BTO deposited on Pt as a function of the water coverage.

As for the BaO termination, the inclusion of the Pt substrate does not significantly change the adsorption energies except for the first water molecule adsorbed on the $N = 4$ periodicity. In this case, the adsorption energy is also slightly increased by approximately 0.1 eV, in part

due to the larger stabilization of the ferroelectric phase in the case of the interface with Pt. Regarding the geometries, the substrate has no influence on the bond distances and angles, so the isolated BTO will only be discussed in details for the TiO_2 termination as well.

While on the BaO termination water adsorption is dissociative, on the TiO_2 termination water is molecularly adsorbed with an adsorption energy of -0.97 eV. This behavior shows a weaker interaction with the TiO_2 termination, confirmed by the lower adsorption energy of -0.97 eV instead of -1.15 eV which is in agreement with previous findings [132, 133] on BTO, but also on $SrTiO_3$ [134]. Yet, this energy is quite high to be only explained by a physical interaction which indicates that the water molecule chemisorbs on the surface.

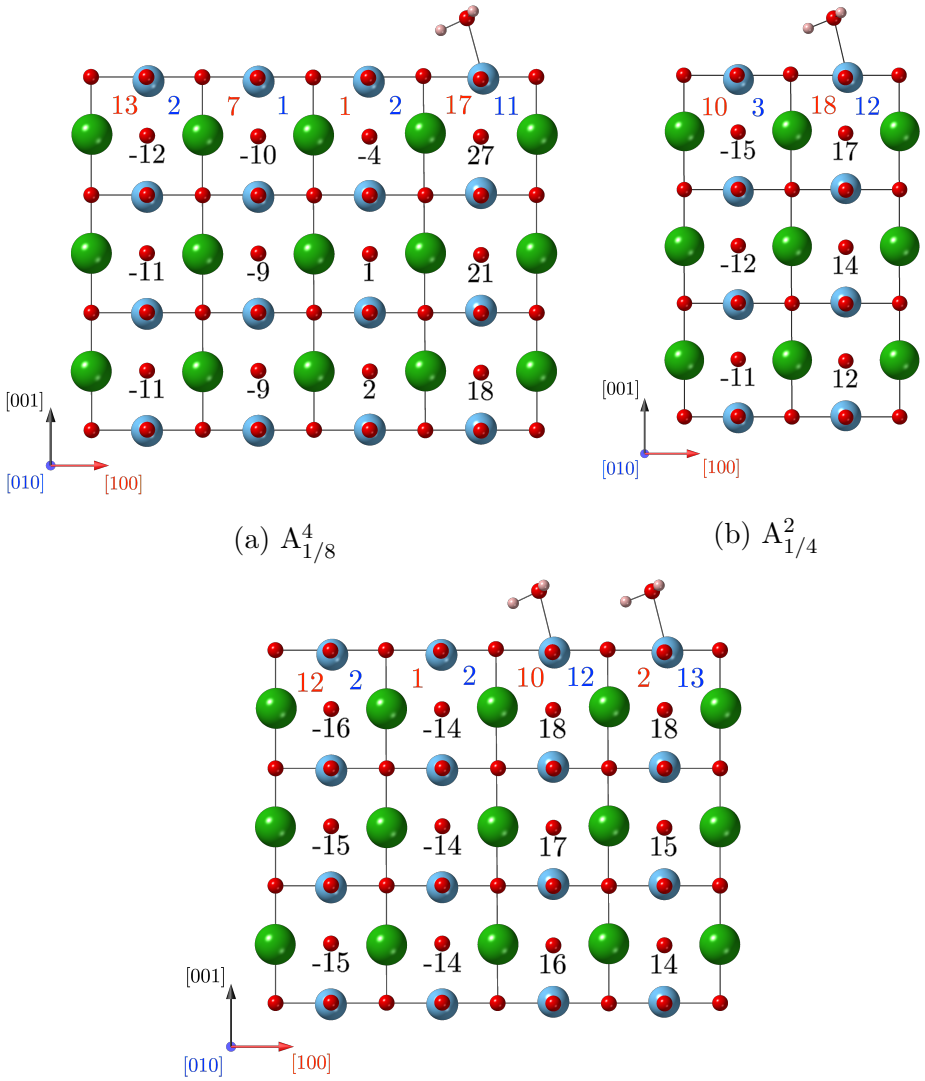

(a) $A^4_{1/8}$ (b) $A^2_{1/4}$

(c) $A^4_{1/4}$

Figure 4.7 – Sideviews of the most stable structure of the TiO_2-terminated surface with $N = 4$ and $\theta = \frac{1}{8}$ ML for $A^4_{1/8}$, $N = 2$ and $\theta = \frac{1}{4}$ ML for $A^2_{1/4}$ and $N = 4$ and $\theta = \frac{1}{4}$ ML for $A^4_{1/4}$.

Figure 4.8 shows the most stable structures at the highest coverage ($\theta = \frac{1}{2}$ ML). The second molecule can either adsorb on the same domain than the first one ($A^2_{1/2}$) or on the oppositely polarized domain ($B^2_{1/2}$). In the former case, the second molecule adsorbs through two hydrogen bonds: one with the first molecule and a second with the surface oxygen at a distance of 1.43 Å and 1.97 Å respectively. The adsorption energy of the second water molecule is -0.99 eV in $A^2_{1/2}$ and the average adsorption energy is -0.97 eV in $B^2_{1/2}$ indicating that both configurations can exist, the only consequences being on the polarization which will be discussed in the following.

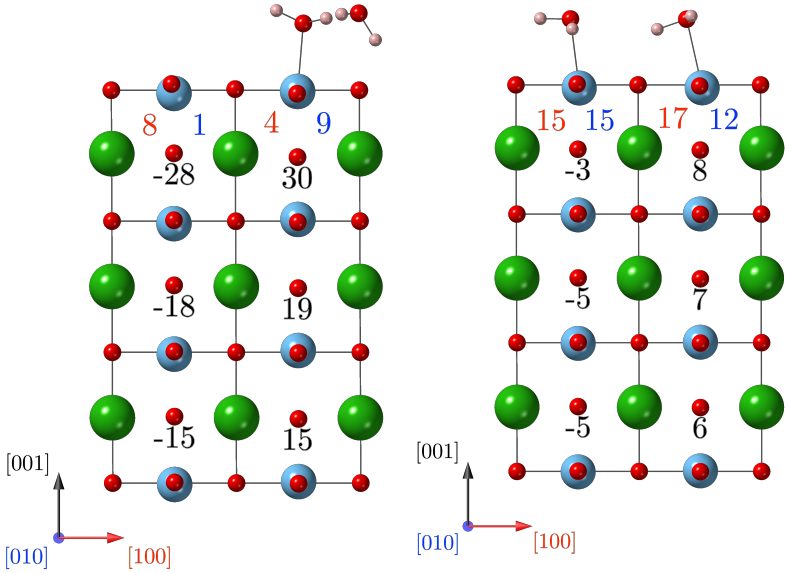

(a) $A^2_{1/2}$ (b) $B^2_{1/2}$

Figure 4.8 – Sideviews of the most stable structures of the TiO_2-terminated surface $N = 2$ and $\theta = \frac{1}{2}$ ML.

Water dissociation

The dissociation of water on the TiO_2 termination is also investigated by adsorbing an OH^- and H^+ ion on the surface with a periodicity of 2 unit cells, leading to a coverage of $\frac{1}{4}$ ML. As for molecular water, the OH^-/H^+ groups are initially adsorbed on both out-of-plane polarization directions and on the paraelectric phase. However, only one optimized structure is found which is displayed on Figure 4.9. The OH^- group binds to the surface Ti while the H^+ binds to a surface O ion. The calculation shows that the surface is very distorted by the water molecule. Indeed, in this case, the Ti atom bonded to the hydroxyl group is extracted from the surface by 0.61 Å while the O atom linked to the H^+ ions is pulled out by 0.38 Å. This configuration is very similar to the one obtained by Geneste *et al.* [132].

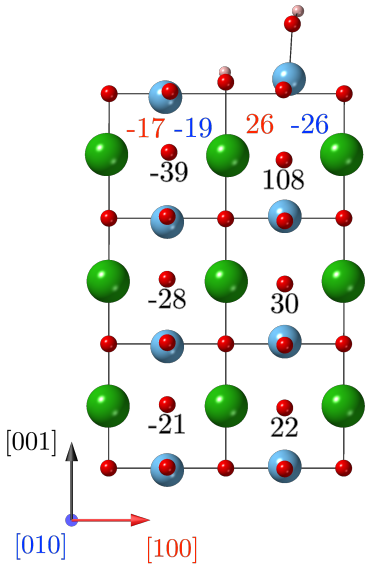

Figure 4.9 – Sideview of the most stable structure of dissociated water OH^-/H^+ adsorbed on the TiO_2-terminated surface with a 2 unit cell lateral periodicity.

4.1.2 Reactivity

The reactivity of water on the TiO_2 termination is also examined in order to determine the energy barrier of the reaction. To this end, the most favorable path of the reaction, usually called the minimum energy path (MEP), has to be found. It represents the lowest energy pathway between a reactant and a product which are both local minima. The transition state (TS) corresponds to a first-order saddle point along the MEP. The search of the TS is important in theoretical catalysis as it allows to find activation energies. In this thesis, the Climbing-Image Nudged Elastic Band (CI-NEB) [135] method is employed to find a first approximation of the geometry and energy of the TS. It consists in creating a set of images by interpolation between the two minima. Here, eight intermediate images are used as an initial guess of the path. These images are connected together with springs, thus forming an elastic band. The energy of each image is then minimized. This procedure gives a first approximation of the TS which is further refined by optimization of its geometry, minimizing the residual forces with a quasi-Newton algorithm [136]. A vibrational analysis is then conducted on the TS to verify if it is a real saddle point with a single imaginary frequency.

The reaction of water dissociation is considered for an initial water coverage of $\theta = \frac{1}{4}$ ML in the case of the slab with a periodicity of 2 unit cells. Therefore, the minimum energy path between the initial state (IS), presented on Figure 4.7, and the final state (FS), shown on Figure 4.9, is explored. The TS is displayed on Figure 4.10 along with the initial and final states for an easier comparison. The Ti-O bond is shortened from 2.23 Å to 2.07 Å. The O-H bond in the water molecule, OH_W, is elongated from 1.00 Å to 1.22 Å as the water

molecule starts to break. Indeed, the H is getting closer to the surface as OH_S is reduced from 1.83 Å to 1.23 Å. The calculated activation barrier to dissociate the water molecule is very small (0.13 eV) while the reaction energy is -0.30 eV. As a consequence, experimentally, water dissociation could occur immediately after the adsorption. The transition state is then characterized by a vibrational analysis. Four imaginary frequencies are found but three of them are negligible with values of 2i, 4i and 5i cm^{-1}. The main imaginary frequency has a value of 717i cm^{-1} and is associated to the cleavage of the O-H bond in the water molecule.

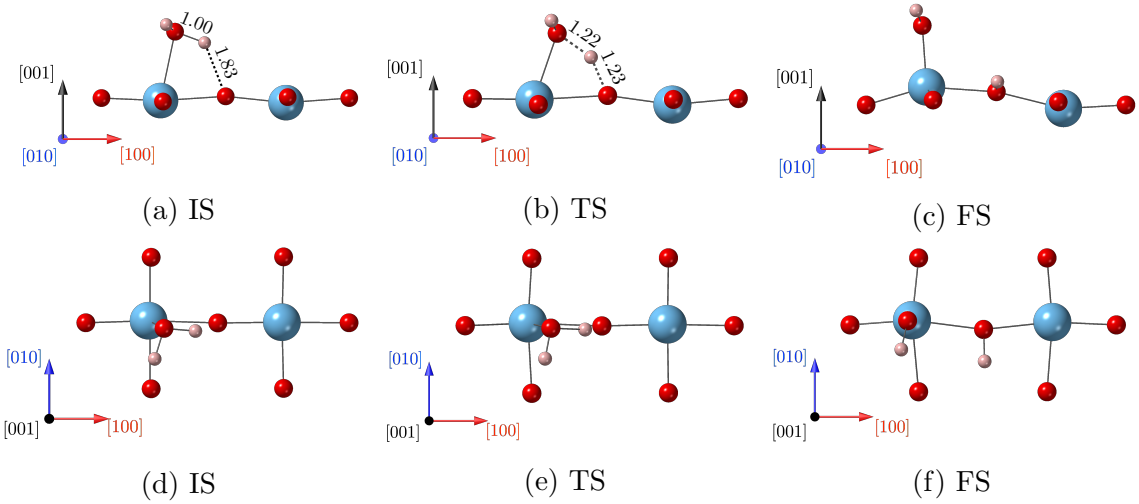

Figure 4.10 – (a), (b), (c) sideviews and (d), (e) and (f) top views of the optimized structures for the initial state (IS), the transition state (TS) and the final state (FS) of water dissociation on TiO_2-terminated $BaTiO_3$ at a coverage of $\theta = \frac{1}{4}$ ML.

4.1.3 Polarization

The influence of water adsorption on the polarization is now discussed in details. The first and the most important conclusion that can be drawn concerns the global polarization. Indeed, whatever the initial polarization state (paraelectric, upward polarization or downward polarization), in presence of water, the final state is always P_{down} for the BaO termination and P_{up} for the TiO_2 one. This result means that water is able to reverse the polarization. More importantly, this indicates that water could be used to control the polarization. In fact, by synthesizing a sample with an excess of Ba, one will obtain the BaO termination and thus, in a humid environment a sample that will be polarized downward, and inversely with an excess of Ti.

Following this important result, the polarization will now be analyzed in details.

4.1.3.1 BaO termination

As previously stated, on the BaO termination water spontaneously dissociates and the structure always stabilizes with the H^+ and OH^- ions adsorbed on the downward polarized domain, regardless of the initial polarization. Therefore, this result seems to indicate that water could switch the polarization to a downward pointing polarization on the BaO termination. Yet, even though the polarization is always downward with water adsorbed on the BaO termination, the different adsorption modes induce specific behavior which have to be discussed. In order to facilitate the discussion, the local out-of-plane polarization of the upper cell for each adsorption modes reported on Figure 4.2 to 4.6 are compiled on Figure 4.11, along with the downward polarized bare BaO termination, used as a reference.

According to Figure 4.11, one can see that Mode 1 and Mode 2 exhibit two distinct behavior. Indeed, regardless of the periodicity and the total number of adsorbed molecules on the slab, adsorption in Mode 2 (green marks) leads to an increase of the polarization in the outermost surface cell compared to bare BTO. Oppositely, when water adsorbs in Mode 1 (blue marks), the local polarization in the surface cell is either kept or lowered compared to BTO without H_2O. This modification of the polarization can be directly related to surface bondings. For $\theta = \frac{1}{4}$ ML with N=2 (Figure 4.3), in Mode 2, the dissociated OH fragment pulls out the Ba atom by 0.26 Å from the surface, while the surface O bound to the H fragment is pulled out by 0.17 Å from the surface. Consequently, the Ti-O bond in cell 1 is elongated which increases the local polarization. On the contrary, in Mode 1, no particular distortion is observed in the first layer and the bare BaO-terminated BTO polarization is kept. Beyond the out-of-plane polarization, water adsorption also induces modifications of the in-plane polarization. Again, Mode 1 and Mode 2 generate different consequences. While the initial structure does not present any in-plane polarization, when water is adsorbed, an in-plane polarization pinned by the orientation of the OH groups, is observed. If the water molecule adsorbs in the (010) plane, corresponding to Mode 2, an in-plane polarization arises along the [100] direction. Conversely, when the adsorption takes place in Mode 1, a small polarization appears along the [010] direction. If one compares the in-plane polarization along [100] for the different periodicities reported on Figures 4.2, 4.3 and 4.6, discrepancies are only observed between the periodicities N=2 and N=4. Indeed, while no component along [100] is calculated in Mode 1 for the 2 unit cell periodicity (Figures 4.3 and 4.6), a component appears for the 4 unit cell periodicity (Figures 4.2, 4.4 and 4.5). The apparition of this in-plane component is due to the enlargement of the domain size as it was already observed [125, 137]. The effect is reinforced when water adsorbs in the [100] direction. Nonetheless, the in-plane polarization is still clearly pinned by the orientation of the OH groups.

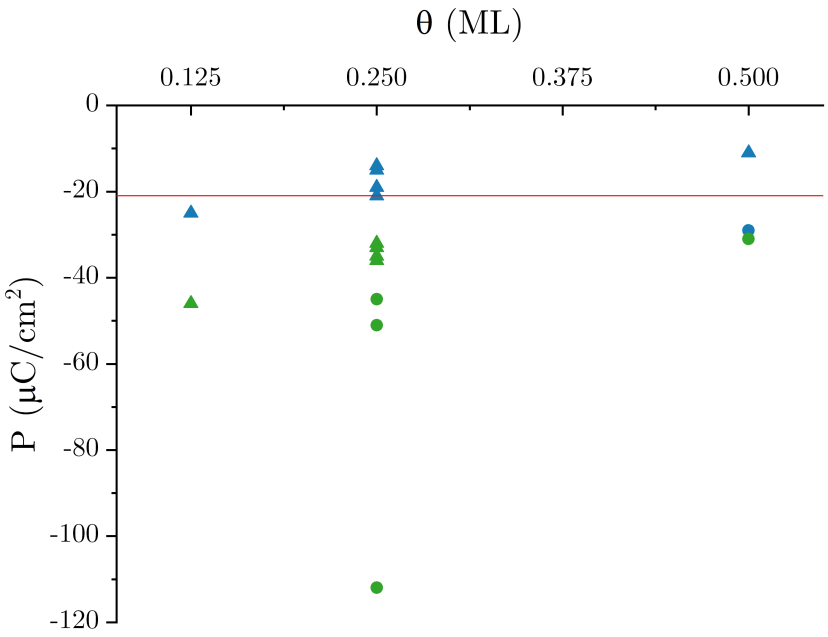

Figure 4.11 – Graphical representation of the local polarization (in $\mu C.cm^{-2}$) in cell 1 where water adsorbs for different coverage ranging from $\frac{1}{8}$ to $\frac{1}{2}$ ML. Blue marks correspond to cases where H_2O is adsorbed in Mode 1, while green marks stand for Mode 2 adsorption. For triangles, only one water molecule is adsorbed per unit cell, while for circles two water molecules are interacting. Corresponding structures are reported in Figures 4.2, 4.3, 4.4, 4.5 and 4.6. The red line corresponds to the reference system BaO polarized downward without H_2O.

Let us now turn to cases with two water molecules interacting (Figures 4.5 and 4.6), corresponding to the circles on Figure 4.11. The presence of two interacting molecules leads to new behavior. The first thing to be noticed is that for a given coverage and adsorption mode, the adsorption of the second molecule leads to an increase of the out-of-plane polarization. Indeed, the second molecule creates a hydrogen bond with the first one which in turn pulls it even more out of the surface, enhancing the polarization. First, the $A^2_{1/2}$ configuration is considered. In this case, the first molecule adsorbs dissociatively but neither in Mode 1 nor in Mode 2, while the second water molecule is chemisorbed molecularly. This leads to an out-of-plane polarization similar to the one observed without H_2O (see Figure 4.11). Additionally, a small polarization arises along [010], but in the opposite direction compared to the one observed with the Mode 1 presented in Figure 4.3. This difference is fully consistent with the orientation of the OH groups, as it is opposite in the two cases.

The $B^2_{1/2}$ configuration corresponds to one dissociated and one non dissociated water molecule as well. The dissociated molecule is almost along the [010] direction as observed for Mode 2. As expected for this orientation, the out-of-plane polarization is increased compared

to the bare surface. Moreover, an in-plane polarization arises along the [100] direction, though it is a bit decreased compared to that in Mode 2, whereas a small polarization emerges along the [010] direction. This is the result of the orientation of the OH group. Indeed, compared to pure Mode 2 with a single water molecule, OH is not perfectly aligned but is slightly deviated from the [010] direction, because of the hydrogen bond with the second molecule.

Finally, the last remaining case to be discussed for a coverage of $\frac{1}{2}$ ML ($B^2_{1/2}$) is composed of two molecules each one being adsorbed on a different unit cell. The neutral polarization of the whole simulation slab is almost preserved with the dissociated molecule adsorbed on a downward polarization domain and the non dissociated physisorbed on an upward polarized cell. This repartition of adsorption configurations is consistent with polarization. Indeed, the larger dissociative adsorption energy leads to downward polarization. The dissociated water molecule presents a Mode 1 configuration, and consequently, a lower out-of-plane polarization is observed compared to bare BTO and an in-plane polarization appears along the [100] direction.

4.1.3.2 TiO_2 termination

The TiO_2 termination is now discussed. As already mentioned, we demonstrate that when the adsorption takes place on out-of-plane polarized TiO_2-terminated BTO, the molecule adsorbs on the upward polarization independently of the initial polarization (see Figure 4.7). This polarization switching on the TiO_2 termination was already suggested by LEED I-V experiments in a previous study [82]. Additionally, Tian *et al.* studied the polarization switching caused by water adsorption on $BiFeO_3$ thin films with a FeO_2 termination [138]. They demonstrated by means of PFM measurements that water shifted the downward polarization to an upward polarization in the whole film. Therefore, both our theoretical results and previous findings demonstrate that the adsorption of water on the TiO_2 termination (or equivalent FeO_2) induces an upward polarized state. Furthermore, in our calculations a polarization along both [100] and [010] directions is found in the first surface layers for all periodicities. This in-plane polarization does not exist in the bare BTO surface whatever the periodicity along [010], and exists only for N=4 along [100], but in a lower extent. Thus, this shows that the in-plane polarization is clearly due to the presence of water. Additionally, this is qualitatively in agreement with previous results obtained by Geneste and Dkhil [132], even if a quantitative comparison is not straightforward given the differences of coverage.

The out-of-plane polarization is now considered. According to Figure 4.12, the presence of water keeps or increases the polarization along [001]. Both the appearance of an in-plane polarization and the evolution of the out-of-plane polarization are directly linked to the way the water molecule adsorbs. In fact, the bonding between the oxygen of the water molecule and the Ti pulls the Ti atom out of the surface up to 0.10 Å, while the highest value ob-

served without H_2O is 0.03 Å for N=4. As a consequence, the Ti-O bond of the first unit cell is elongated which increases the upward polarization in this cell. In addition, the water molecule sets the H_2O orientation and thus the polarization imprint.

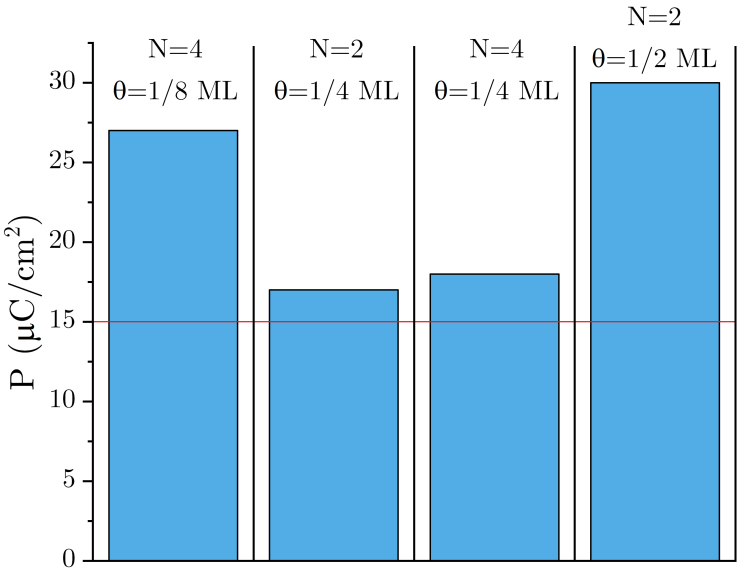

Figure 4.12 – Graphical representation of the local polarization (in $\mu C.cm^{-2}$) in cell 1 where water adsorbs for coverage $\frac{1}{8}$ ML with N=4, for coverage $\frac{1}{4}$ ML with N=2 and N=4 and for coverage $\frac{1}{2}$ ML with N=2 with both molecules on the same unit cell. The red line corresponds to the reference system TiO_2 polarized upward without H_2O.

For the dissociated case on the TiO_2 termination (see Figure 4.9), the surface is broadly modified by the presence of water which induces high distortions. Consequently, the polarization is widely increased, especially in the surface region of the slab bonded to water where the out-of-plane polarization is found to be 108 $\mu C.cm^{-2}$ because of the upward displacement of the Ti atom. It is also worth mentioning that water again induces an upward polarization of the TiO_2 termination regardless of the initial polarization. A rather large in-plane polarization is also observed in the first surface unit cell. The OH fragments are adsorbed along the [010] direction inducing a large polarization of -26 $\mu C.cm^{-2}$ along this direction. Moreover, the large distortions generated by the dissociated water creates a polarization along the [100] direction, even though it is usually null for the bare TiO_2-terminated BTO with N=2.

4.2 Experimental results

The careful experimental study of water adsorption with a particular interest in the influence of the polarization is really not a straightforward process. Indeed, one has first to prepare samples with a controlled polarization which is far from a trivial procedure. Several approaches have been proposed over the years but all have serious limitations. As already mentioned, PFM can be used to pole a sample in the desired direction but this technique is limited to a very narrow area of application, in the order of the μm^2, hence it does not allow the poling of a macroscopic sample [131, 139–141]. Another method consists in depositing an electrode on top of the ferroelectric thin film and applying an electric field to pole it [142–144]. The top electrode can further be removed by etching, however this process possibly involves the contamination of the ferroelectric surface and thus prevents the study of perfect model samples. Finally, it was reported that it is possible to macroscopically pole a sample in an electrochemical cell containing a non-aqueous electrolyte such as $LiClO_4$ [131, 145]. Yet, this method also induces relatively high level of contamination which is not suitable to refined surface experiments. Therefore, in this study, it was decided to analyze the native samples with their spontaneous remanent polarization, allowing the adsorption of water on surfaces with as little contamination as possible.

Then, the remanent polarization should be measured. A usual quantitative method is the measurement of ferroelectric P-E hysteresis loops. However, this method requires the deposition of metallic electrodes on the sample, leading to previously discussed issues. In our case, the direction of the remanent polarization in the samples was qualitatively assessed by PFM measurements.

Finally, water adsorption experiments should be performed on a clean surface to avoid spurious contamination effects. The determination of the polarization during water adsorption is also a very difficult task. Kalinin *et al.* showed that it is possible to perform PFM measurements in a liquid environment allowing to measure directly the polarization of a ferroelectric material in contact with water [146]. This method was recently used by Tian *et al.* to evidence the polarization switching in $BiFeO_3$ in aqueous environment [138]. However, it requires a specific set up which was not available in this project. Hence, we chose to simply follow the spectroscopic parameters evoked in the previous chapter in order to reveal phenomena which might be related to polarization.

S_1(BaO) and S_2(TiO_2) samples presented in section 3.5 were then studied under different water pressure, allowing to investigate the two possible surface terminations in order to compare with theoretical results. Both samples were exposed to a maximum of 50 L corresponding to an exposition of 100 seconds under a water pressure of 5.10^{-7} mbar. In order to

reach as much surface sensitivity as possible, the O 1s core level was measured with a photon energy of 600 eV at grazing take-off angle. Figure 4.13 displays a typical O 1s peak acquired in these conditions. The peak exhibits two components: one at 529.8 eV (in red) and a second at 531.5 eV (in blue). The former is attributed to the O^{2-} of the BTO lattice while the latter is ascribed to the hydroxyl groups OH^- adsorbed on the surface. In the considered water exposure range, no molecular water H_2O, materialized by a third component in the O 1s peak shifted by around 3 eV from the O^{2-} component, was seen to be adsorbed [147, 148].

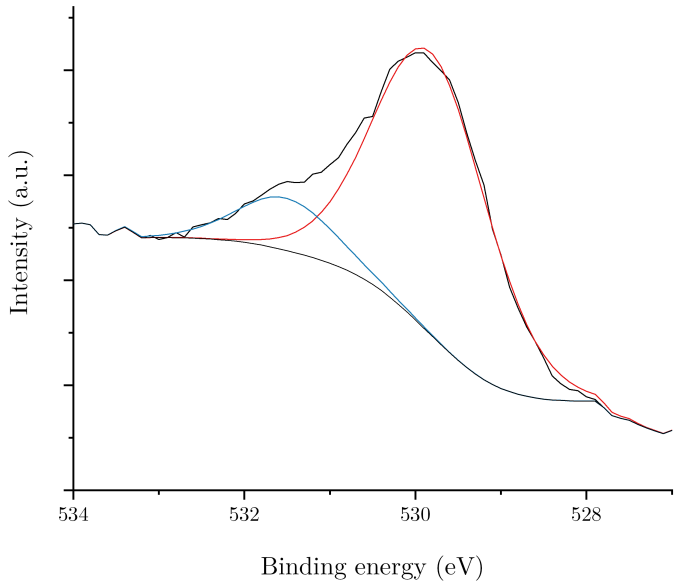

Figure 4.13 – XPS spectrum of the O 1s core level for a 16 nm thick $BaTiO_3$/Nb:$SrTiO_3$ sample acquired with a photon energy of 600 eV at grazing take-off angle.

Figure 4.14 represents the evolution of the Ba 4d-Ti 3p shift, as defined in equation 3.5, in both samples as a function of the amount of hydroxyl groups adsorbed at the surface. The OH^- surface concentration is defined as the OH^- peak area divided by the total O 1s peak area. The first thing that can be observed on Figure 4.14 is that the amount of hydroxyls adsorbed on the surface is higher in the case of the BaO-terminated sample. This can be correlated to the theoretical results showing that water is more favorably dissociated on the BaO termination than on the TiO_2 termination. Indeed, we showed that water is spontaneously dissociated into OH^- on the BaO termination while it requires a small activation energy on the TiO_2 termination. Here, water is dissociated on the TiO_2 termination as well even though it was calculated that water dissociation is not spontaneous on this termination. The rather small activation energy (0.13 eV) required to dissociate water could explain the discrepancy between theoretical predictions and experimental observations. Indeed, the difference in the water coverage reachable by calculations and the experiment could explain the discrepancy of the results. Moreover, calculations are performed at 0 K, therefore thermic

agitation could also allow to overcome such a low energy barrier.

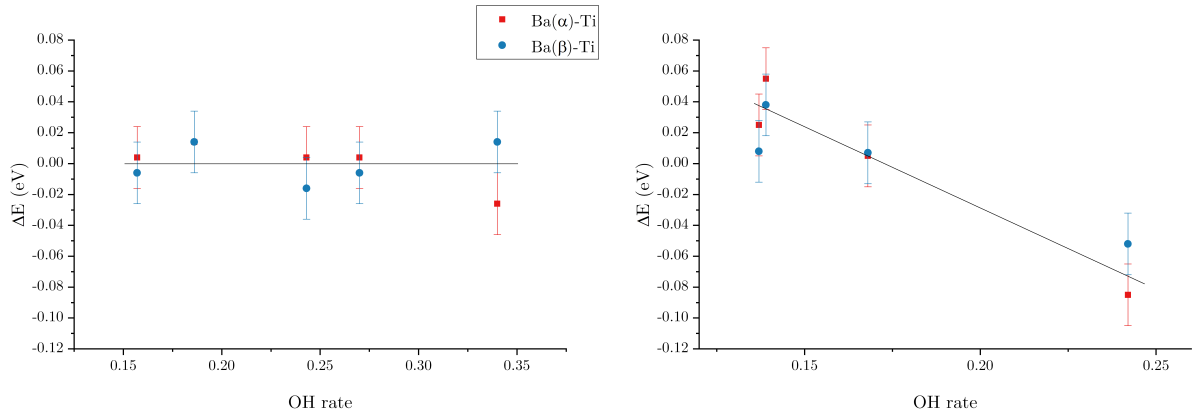

(a) S_1(BaO) (b) S_2(TiO_2)

Figure 4.14 – Evolution of the shift Ba 4*d*-Ti 3*p* as a function of the hydroxyl concentration on the surface for (a) S_1(BaO) and (b) S_2(TiO_2). The symbols are the same in both figures. The solid lines are only guides to the eye.

The second interesting observation on Figure 4.14 concerns the evolution of the Ba 4*d*-Ti 3*p* shift. Contrary to the shift in temperature discussed in the previous chapter, ΔE evolves in the same manner for both Ba(α) and Ba(β) components. This tends to indicate that, in this case, the Ti 3*p* peak could shift rather than the Ba 4*d* ones. For the BaO termination, ΔE is not modified by the adsorption of water. Oppositely, for the TiO_2-terminated sample, it seems that there is a shift towards higher binding energies of the Ti 3*p* peak as the water amount increases. This different behavior could be explained by different modifications of the surface induced by water adsorption on both terminations. Indeed, in the BaO termination, calculations showed that the surface Ba cation is extracted from the surface by 0.26 Å in the most surface distorted case. On the contrary, when water is dissociated on the TiO_2 termination, the Ti surface atom is extracted by 0.61 Å. This rather large surface distortion can induce a modification of the Ti chemical environment and thus result in a change in the Ti binding energy.

4.3 Outline

Water adsorption on out-of-plane polarized $BaTiO_3$(001) surfaces has been investigated. Both BaO and TiO_2 terminations have been envisaged and different water coverages, ranging from $\frac{1}{8}$ ML to $\frac{1}{2}$ ML have been considered. Regarding the BaO-terminated BTO, water systematically dissociates on the surface with a H^+ ion bonded to a surface O^{2-} and the OH^- group bonded to Ba^{2+} ions. Interestingly, the initial polarization (paraelectric, upward or downward polarization) does not impact the final optimized structures. Water is always observed to dissociate on the downward polarization.

A different behavior is seen on the TiO_2 termination. Indeed, in this case, water does not spontaneously dissociate but rather molecularly adsorbs on the surface. This indicates a lower affinity of the TiO_2 termination towards water adsorption than the BaO termination. However, the high adsorption energy shows that the water molecule is chemically bonded to the surface. While water stabilizes downward polarized BaO-terminated BTO, we showed that the opposite happens on the TiO_2 termination, as water adsorbs on the upward polarization. The reactivity of water dissociation of TiO_2-terminated BTO has also been studied. It allows to demonstrate that the activation energy barrier required to break the water molecule is quite low (0.13 eV). This suggests that water could rapidly dissociate after molecular adsorption to lead to a more stable dissociated state. The analysis of the polarization pattern in the dissociated case shows that the polarization is much higher when water is dissociated than when it is molecularly adsorbed. This enhancement of the polarization is particularly observed in the first surface cell as the first TiO_2 layer is widely distorted by the adsorbed OH^- and H^+ ions.

Experimentally, we observed a higher hydroxylation of the surface on the BaO-terminated BTO than on the TiO_2 termination. This tends to confirm the theoretical results showing the stronger interaction of the BaO termination than the TiO_2 one. Additionally, we detected the presence of OH^- groups on the TiO_2 termination surface while DFT calculations predicted molecular H_2O adsorption on this surface. This hints that the small calculated activation energy can indeed be instantaneously overcome in real world conditions.

The shift of the Ti $3p$ photoemission peak as a function of the increasing hydroxyl concentration was also recorded. No shift is observed on the BaO termination while the TiO_2 termination exhibits a shift towards higher binding energies of the Ti $3p$ peak is measured. This could reveal a modification of the Ti chemical environment which could be related to the high surface distortion of the surface in the TiO_2-terminated BTO induced by water adsorption as foreseen by DFT calculations.

Chapter 5

Time-resolved photoelectron spectroscopy results

The charge dynamics in a photocatalyst are very important properties. Indeed, as discussed in section 1.3, the electron-hole recombination can drastically decrease the efficiency of the semiconductor. Therefore, measuring the recombination rate can be useful to improve the photocatalyst efficiency. Additionally, it is important to understand the charge carrier mobility, in particular when in contact with water. In this chapter the charge carrier dynamics in BTO and hematite thin films are measured by means of time resolved photoemission spectroscopy. Hematite thin films are investigated additionally while exposed to water in near ambient pressure conditions.

5.1 $BaTiO_3$ thin films

In a previous study, Rioult *et al.* showed that the efficiency of a $BaTiO_3$ photoanode highly depends on its polarization direction [131]. They showed that the generated photocurrent is significantly higher when BTO exhibits a downward polarization rather than an upward polarization. The internal electric field induced by the downward polarization favors the displacement of holes towards the surface which increases water oxidation. Thus, it can be interesting to measure the charge dynamics in a BTO thin film as a function of its polarization direction.

5.1.1 Samples

For TR-PES experiments, the BTO thin films were deposited on single crystalline Pt(001). Two different samples were elaborated by OA-MBE at CEA-Saclay. In this study, the surface termination of the sample was not controlled during the growth process, therefore it can be assumed that the surface presents both TiO_2 and BaO terminations equally. The polarization was assessed by PFM measurements as described earlier. The results are presented on Figure

5.1. It can be seen that the samples have an opposite out-of-plane polarization. The sample referred to as BTO_{up} shows no contrast between the background and the region written with a negative voltage, indicating that the sample has an overall upward polarization. On the contrary, for the sample referred to as BTO_{down}, the region written with a positive voltage presents a similar phase than the background, suggesting that the sample is globally downward polarized. BTO_{down} has a thickness of 10 nm whereas BTO_{up} has a thickness of 25 nm. This difference in thicknesses could actually be the reason of the opposite polarization orientation.

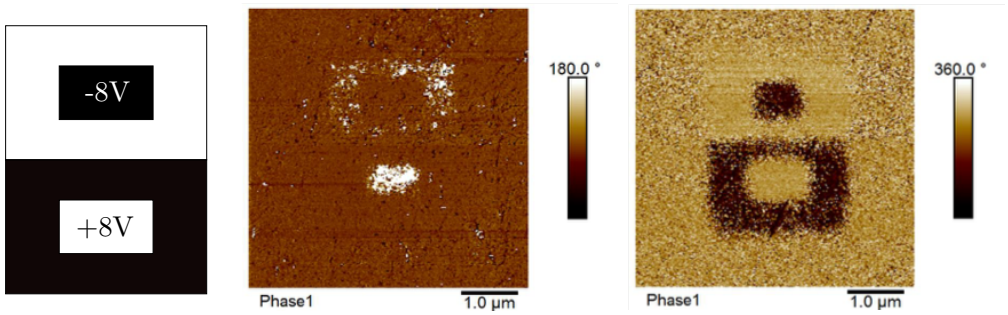

(a) (b) BTO_{up} (c) BTO_{down}

Figure 5.1 – (a) PFM written polarization pattern, polarization measured in reading mode by PFM on (b) BTO_{up} and (c) on BTO_{down}.

5.1.2 TR-PES measurements

Both samples were measured by time-resolved photoemission spectroscopy to investigate their respective charge carrier dynamics. The experiments were conducted on TEMPO beamline at synchrotron SOLEIL. The laser used to pump the samples had a wavelength of 355 nm and was modulated with a 50 % duty-cycle at a period $T = 200$ ms and $T = 2$ s for BTO_{up} and BTO_{down}, respectively. The O $1s$ core level was recorded with a photon energy of 825 eV. The laser-induced O $1s$ core level shift is represented on Figure 5.2. As indicated by the dashed lines, for BTO_{up}, the laser is switched on at $t = 0$ ms and then off at $t = 100$ ms. For BTO_{down}, the laser is turned on at $t = 0$ s and off at $t = 1$ s.

The characteristic lifetimes for both the surface photovoltage (SPV) onset and decay were obtained using the following equation [149]:

$$\Delta V_{SP}(t) = -\alpha kT \ln\left[1 - \exp\left(\frac{-t}{\tau_\infty}\right)\left(1 - \exp\left(\frac{-\Delta V_{SP}^{tot}}{\alpha kT}\right)\right)\right] \tag{5.1}$$

where α is a material parameter ranging from 0.5 to 2, ΔV_{SP}^{tot} is the total surface photovoltage and τ_∞ is the dark carrier lifetime (the lifetime of charge carriers in the absence of a surface photovoltage). Here, α is fixed to 1 and kT to 26 meV. The calculated parameters are shown

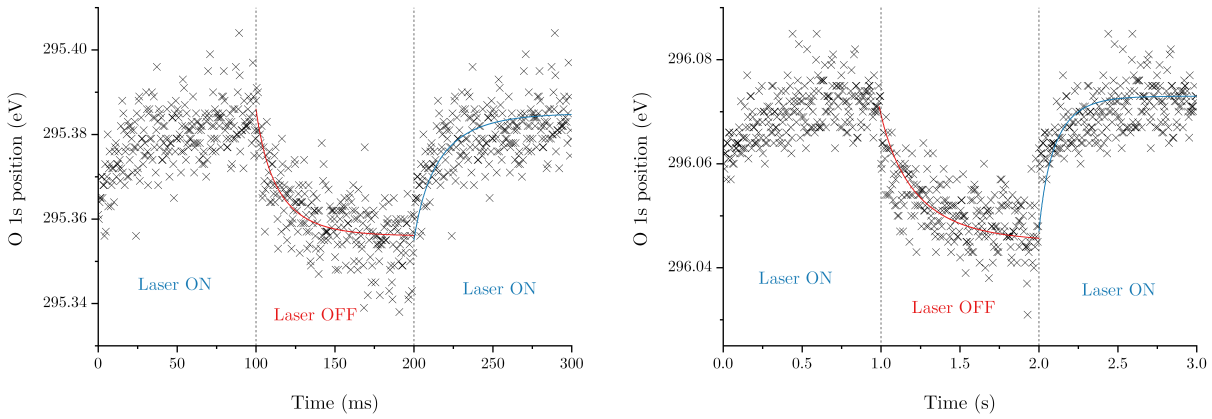

(a) BTO_{up} (b) BTO_{down}

Figure 5.2 – Kinetic energy shift of the O 1s core level of (a) BTO_{up} and (b) BTO_{down} recorded with a photon energy of 825 eV.

on Table 5.1. For both samples, when the laser is turned on, a shift of the O 1s core level is observed towards higher kinetic energies. This is surprising as the SPV shift is related to the band bending at the interface. A photoemission shift to lower kinetic energies is usually related to a surface depletion while a shift towards higher kinetic energies is the sign of a surface accumulation. Therefore, for a n-type semiconductor, an apparent negative SPV (a shift towards lower kinetic energies upon laser excitation) is expected. However, a positive SPV can also be the sign of photoconduction: when the laser is off the sample is charging due to photoelectron emission, the photoemission peaks shift towards lower kinetic energies; when the laser is switched on, the sample is discharging because of photoconduction and the photoemission peaks shift towards higher kinetic energies. In such a case, the SPV decay does not only represent the electron-hole lifetime, but also the photogenerated charge transfer and mobility terms. Here, we observe that the polarization direction seems to highly influence the SPV value and more particularly the time decay. This could be understood as follow. When the sample has an upward polarization, the electric field favors the extraction of electrons during the photoemission process, increasing therefore the charging phenomenon, and thus the SPV. The difference in characteristic lifetimes is not yet understood but could be related to the chemical composition of the surface of the sample, such as the Ti/Ba ratio or the electronic structure of the Ba species.

	BTO_{up}		BTO_{down}	
	Decay	Onset	Decay	Onset
τ_∞ (ms)	21	24	318	142
ΔV_{SP}^{tot} (meV)	30	30	25	25

Table 5.1 – Characteristic lifetimes of the SPV in upward and downward polarized $BaTiO_3$.

We also tried to perform TR-PES during the adsorption of water in UHV on the different samples. Unfortunately, adsorbed water is not stable under the synchrotron beam, preventing the measurement of the surface with water. This issue will be describe later in the case of hematite, showing that only near ambient pressure conditions allows such a study.

5.2 Fe_2O_3 thin films

As previously mentioned the large band gap of BTO (3.2 eV) limits its efficiency due to low visible light absorption. A possible solution to enhance BTO performances as a photoanode could be to combine it with another material in a heterojunction. This approach could allow a better light absorption of the system thanks to different band gaps to maximize the absorption of the incident photons. Additionally, heterostructures may drive better charge separation because of the spontaneous electric field arising at the junction between the two materials as well as possible enhanced kinetics [150].

Hematite (α-Fe_2O_3) is a widely studied semiconductor as a photoanode material. This interest is mainly related to its suitable band gap (2.2 eV) which allows it to absorb 40% of the solar light yielding a theoretical solar-to-hydrogen conversion between 14-17% [151]. Moreover, it is an abundant material and is stable in aqueous environments which could make hematite a good candidate as a photoanode material for solar water splitting. Its valence band edge is located below the OH^-/O_2 potential, however its conduction band edge is below the H_2O/H_2 redox potential (see section 1.3) which means that an electrical bias is required to promote water splitting. Therefore, it could be interesting to combine hematite with a ferroelectric material, such as BTO, which could provide this extra input of energy directly with its internal electric field. In the meantime, hematite could allow better light absorption of the whole system thanks to its more suitable band gap.

5.2.1 Samples

As for the BTO samples, hematite samples were prepared by OPA-MBE at CEA-Saclay. Hematite was grown on Pt(111) single crystal substrates with a diameter around 1 cm and a thickness of 1 mm. Two different samples were studied: a 15 nm thick Fe_2O_3 thin film and a 20 nm thick 2 at.% Ti-doped Fe_2O_3 thin film. Prior to any synchrotron measurement, both samples were annealed in a preparation chamber for 1h at 572 K under an O_2 pressure of around $1.5.10^{-6}$ mbar.

5.2.2 NAP-XPS

Both samples were studied in NAP-XPS under increasing water pressure to investigate the behavior of water adsorption on these surfaces. The samples were exposed to water pressure

ranging between 0 and 1.1 hPa. The O 1s spectra were acquired with a photon energy of 830 eV. The results are presented in Figure 5.3. In both samples a main component at a binding energy of 530.0 eV appears which is attributed to the O^{2-} ions of the hematite lattice. Even before introducing water, the O 1s peak exhibits a second component at a position of 531.3 eV which is representative of the presence of OH^- groups at the surface of the samples. As the water pressure increases, two additional components arise. One, shifted by around 2.8 eV towards higher binding energies, indicates the presence adsorbed H_2O [147, 148] while the second with a binding energy of 535.7 eV is attributed H_2O in the gas phase.

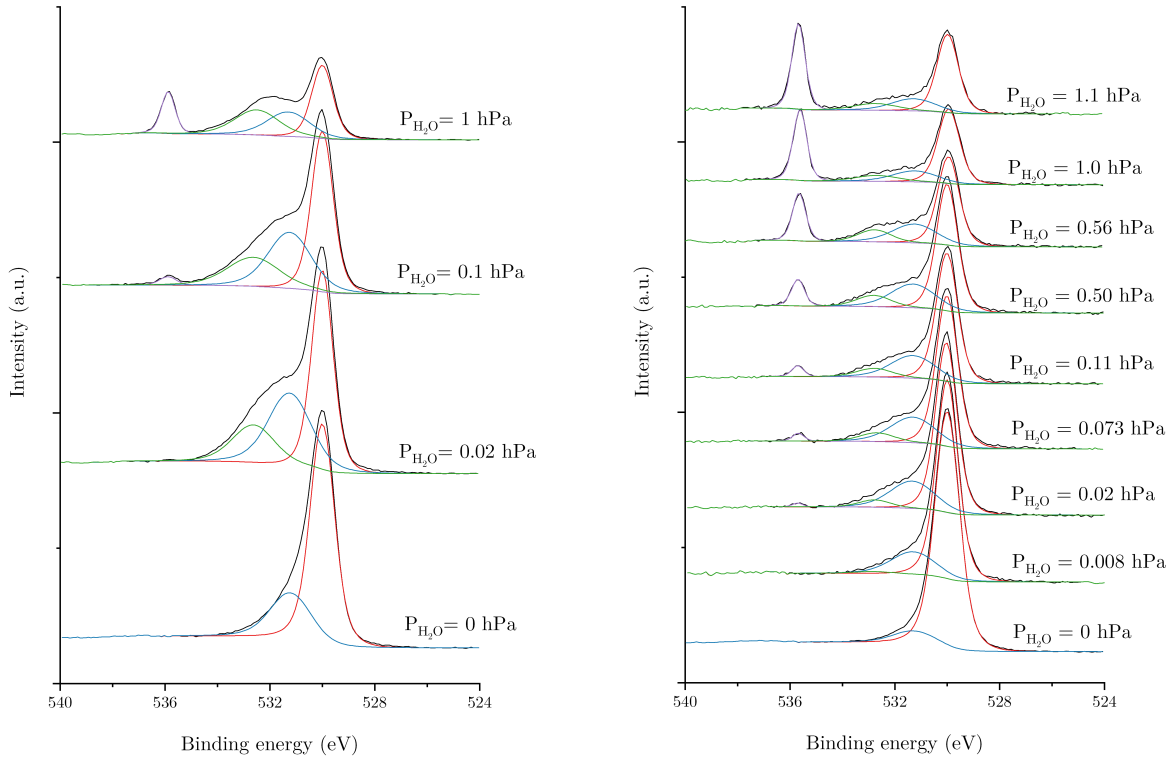

(a) Fe_2O_3 (b) Ti:Fe_2O_3

Figure 5.3 – NAP-XPS spectra of the O 1s peak under increasing water pressure for (a) the Fe_2O_3 sample and (b) the Ti:Fe_2O_3 sample, recorded with a photon energy of 830 eV. The black curve shows the recorded signal. The red, blue, green and purple curves are the O^{2-}, OH^-, H_2O and H_2O in the gas phase components, respectively.

The evolution of the concentration of hydroxyl groups and water molecules on the surface is described with a ratio of the peak areas as:

$$\%OH^- = \frac{A_{OH^-}}{A_{O^{2-}} + A_{OH^-}} \tag{5.2}$$

$$\%H_2O = \frac{A_{H_2O}}{A_{O^{2-}} + A_{OH^-}} \tag{5.3}$$

where A_{OH^-}, $A_{O^{2-}}$ and A_{H_2O} are the peak area of the OH^-, O^{2-} and H_2O components, re-

spectively. The results are shown on Figure 5.4. The first observation is that in both samples hydroxyl groups are first adsorbed and the saturation is reached rapidly. It can be noted that the hydroxylation rate is higher on pure Fe_2O_3 than on Ti doped Fe_2O_3. This difference might be explained by a lower affinity of the Ti cation towards water dissociation, decreasing the number of possible adsorption sites available on the surface. When the saturation is reached, molecular water starts to adsorb. The water coverage is higher in the case of pure Fe_2O_3 than on Ti:Fe_2O_3 which could be related to the difference in hydroxylation rate, as molecular water probably adsorbs on hydroxyl groups via hydrogen bonds. These assessments could be verified by means of DFT calculations which help to determine the modification of the water adsorption behavior induced by Ti doping.

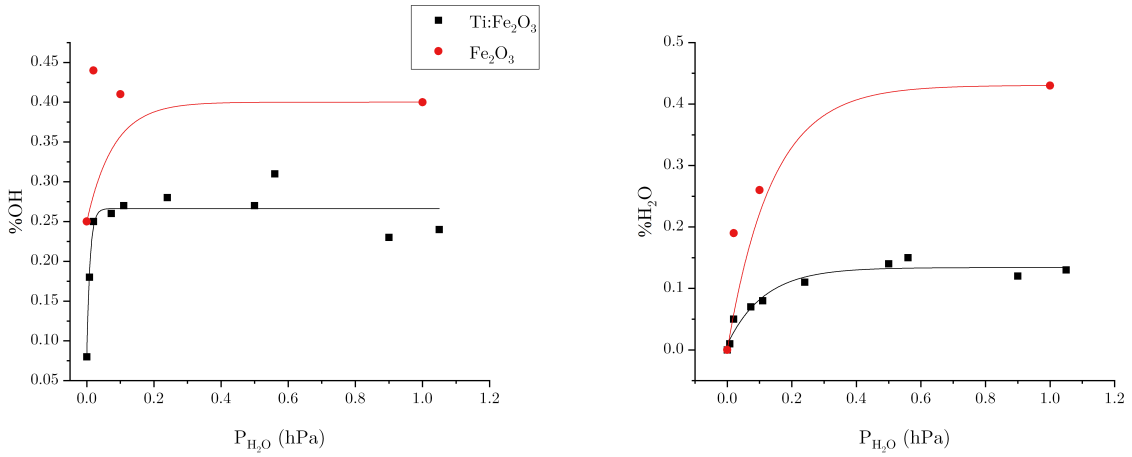

(a) (b)

Figure 5.4 – (a) OH^- and (b) H_2O concentration evolution on the surface of Fe_2O_3 and Ti:Fe_2O_3 as a function of the water pressure. The symbols are the same in both figures.

5.2.3 Evolution of water adsorption during synchrotron measurements

In past experiments not shown in this thesis, TR-PES experiments were conducted on hematite in UHV after exposition to several langmuir of water. Water was indeed evidenced to be adsorbed on the surface but it was also observed that the vacuum environment, the synchrotron radiation and/or the laser irradiation induce a very fast desorption of water (in the order of a few minutes). Time-resolved XPS experiments require the sample to be illuminated by the laser and the synchrotron radiation during several hours. Thus, synchrotron radiation or laser induced desorption processes could lead to spurious results. It is therefore important to check if such phenomena take place in NAP conditions as well.

The evolution of water adsorption in NAP conditions was first assessed without laser irradiation in order to check if adsorption kinetics or synchrotron radiation induced desorption have an impact in the time scale of interest here. To do so, the O 1s core level was measured on the Ti:Fe_2O_3 sample exposed to 0.24 hPa of water while the sample was exposed to the synchrotron beam. The concentration of OH^- groups and H_2O molecules on the surface are shown on Figure 5.5. It is clear that no modification of the hydroxylation of the surface nor in molecular water adsorption is observed in 30 minutes. This tends to indicate that a stationary state is quickly reached in these conditions. Hence, even if synchrotron radiation induces a desorption of water, it does not have an effect on the measured O 1s peak.

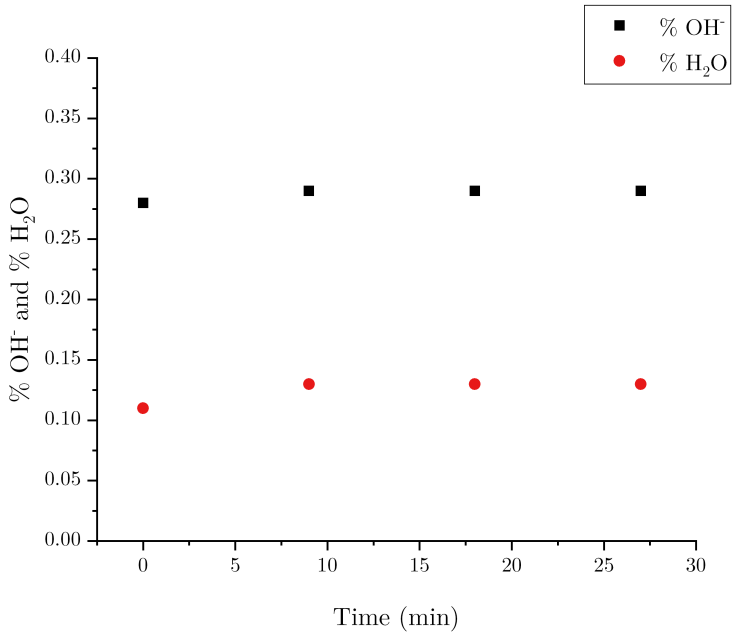

Figure 5.5 – Evolution in time of %OH^- and %H_2O on Ti:Fe_2O_3 exposed to 0.24 hPa of water in NAP conditions.

It is also important to verify if this remains true when the laser is switched on. Figure 5.6 displays the results of a similar experiment with the laser switched on. The first point at $t = 0$ min shows the surface state just before the laser is turned on. In this case, the hydroxylation and molecular water concentration might slightly increase when the surface is irradiated by the laser but such a small increase should not influence TR-PES results.

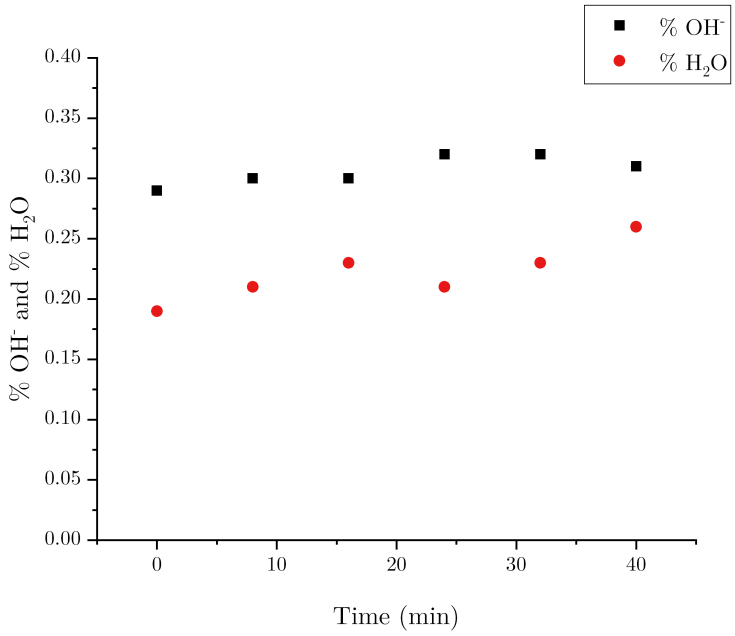

Figure 5.6 – Evolution in time of $\%OH^-$ and $\%H_2O$ on Ti:Fe_2O_3 exposed to 0.24 hPa of water in NAP conditions while illuminated with the laser.

These results tend to indicate that if one wants to measure the influence of water adsorption on charge carrier dynamics by means of time-resolved XPS, experiments should be performed in NAP. Indeed, while water is seen to quickly desorb in UHV, thus preventing from recording time-resolved XPS spectra with water adsorbed on the surface, NAP conditions allow to reach a stationary state towards water adsorption.

5.2.4 Charge carrier dynamics in hematite

5.2.4.1 In vacuum

Time-resolved XPS measurements of the SPV decay following photoexcitation were first conducted on both samples in UHV. The O 1s peak was recorded with a photon energy of 830 eV. The laser pumping the sample had a wavelength of 405 nm and was modulated with a 40% duty-cycle at a period $T = 56$ μs. XPS spectra were recorded every 220 ns using a delay-line detector. The time dependance of the O 1s core level shift induced by the laser is shown on Figure 5.7a for the Fe_2O_3 sample and on Figure 5.7b for the Ti doped Fe_2O_3 sample. In both cases, the laser was turned on at 0 μs and switched off at 22 μs (indicated by the dashed line on Figure 5.7). The onset and the decay of the SPV are fitted using equation 5.1. The results are summarized in Table 5.2. In the case of hematite, α is fixed at 1.5.

	Fe_2O_3		$Ti:Fe_2O_3$	
	Onset	Decay	Onset	Decay
τ_∞ (μs)	20	25	20	25
ΔV_{SP}^{tot}	95	95	110	110

Table 5.2 – Characteristic lifetimes of the SPV in Fe_2O_3 and $Ti:Fe_2O_3$ in UHV conditions.

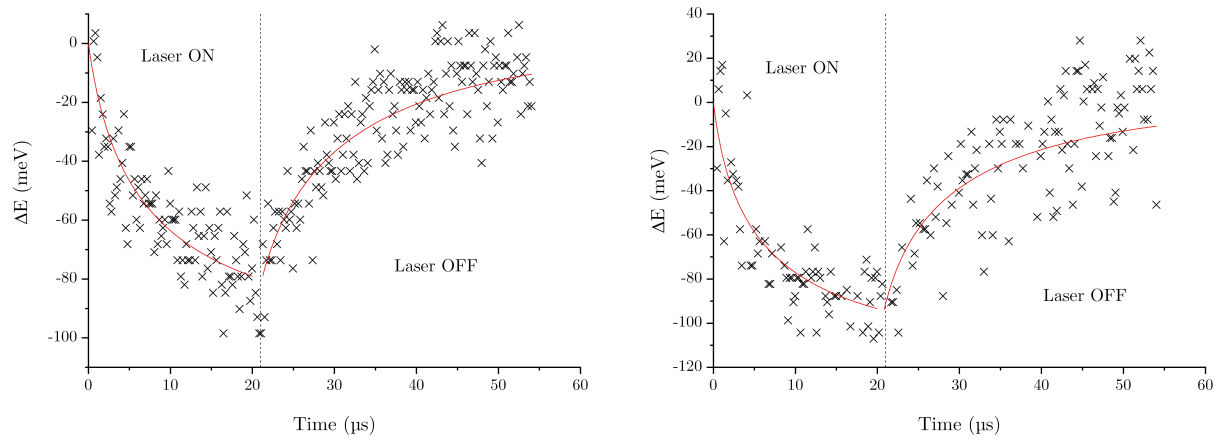

(a) Fe_2O_3 (b) $Ti:Fe_2O_3$

Figure 5.7 – Kinetic energy shift of the O 1s core level of (a) Fe_2O_3 and (b) $Ti:Fe_2O_3$ recorded with a photon energy of 830 eV.

Both samples present a similar charge carrier behavior. When the laser is switched on, the O 1s core level shifts towards lower kinetic energies by 95 meV and 110 meV for Fe_2O_3 and $Ti:Fe_2O_3$, respectively. This indicates that holes are moving towards the surface of the sample which is characteristic of a n-type semiconductor behavior, as it is supposed for hematite. Ti doping is expected to increase n-type doping, and thus upward band bending, which seems to be indeed the case here as the SPV is increased compared to pure hematite. However, upon excitation the charge carrier saturation is not reached in the time scale used here. The SPV onset time is 20 μs in both samples while the dark carrier lifetime is 25 μs in both cases as well. Therefore, it seems that Ti doping allows to increase the band bending in hematite and could thus improve its efficiency as a photoanode. Though it was shown above that Ti doping also decreases water adsorption on hematite, Rioult *et al.* reported an increase of the photocurrent by 2 orders of magnitude in $Ti:Fe_2O_3$ compared to undoped Fe_2O_3, suggesting that the band bending increase due to Ti doping is predominant compared to the reduction of water adsorption favoring [37].

5.2.4.2 Exposed to water in NAP conditions

As water splitting is performed in aqueous environment, it is essential to determine whether or not the charge dynamics are modified in such conditions. We saw that laser irradiation and

synchrotron beam induce the desorption of water, thus UHV conditions are not appropriate to record TR-PES spectra which requires rather long acquisition time (several hours). NAP conditions are the most suited conditions to perform water adsorption while still allowing time-resolved XPS measurements. Indeed, NAP-XPS allows to reach a stationary state regarding water adsorption, diminishing the effect of desorption.

5.2.4.2.1 Effect of surface contamination

The Fe_2O_3 sample was then exposed to 0.1 hPa of water under synchrotron radiation for several hours while recording photoemission spectra. However, no O 1*s* core level shift was observed in these conditions. It was thus decided to pump the chamber to UHV and an overview photoemission spectrum was recorded to control the surface state (see Figure 5.8a). A very intense peak with a binding energy around 287.0 eV was measured. It is associated to adventitious carbon, probably due to the reaction on the surface of carbonated species, such as CO_2, contained in the water. The amount of carbon contamination must be quite important because the Fe 2*p* core level peaks, with a binding energy of around 726.4 eV and 713.2 eV, almost no longer appear due to the thickness of the contamination layer. In order to better understand the origin of this carbon contamination, an XPS spectrum was recorded on a region of the sample which was not exposed to the synchrotron beam. The spectrum is displayed on Figure 5.8b. In this case, the C 1*s* core level peak is much smaller than on the region exposed to the synchrotron radiation. This suggests that the synchrotron radiation promotes the adsorption of carbonated species, possibly through a kind of photolysis of carbon dioxide dissolved in water.

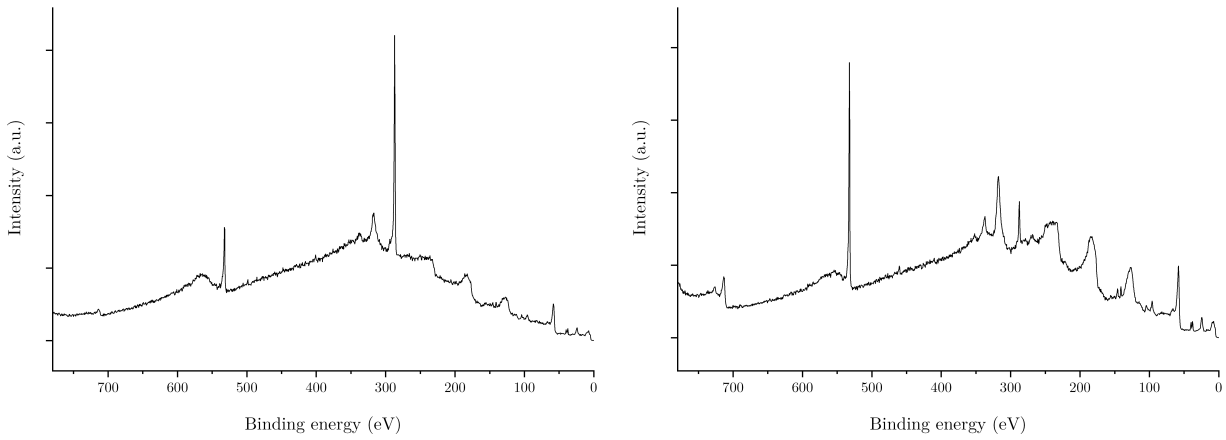

(a) (b)

Figure 5.8 – Overview spectra recorded with a photon energy of 830 eV on the Fe_2O_3 sample after being exposed to 0.1 hPa of water for several hours (a) under synchrotron radiation and (b) without synchrotron radiation exposition.

The time-resolved XPS spectra recorded on the contaminated surface are featured on Figure 5.9. The red circles present the O 1s core level shifts on the contaminated surface recorded in UHV whereas the blue triangles show the spectra measured on the same surface while exposed to 0.5 hPa of water. Black crosses represent the results presented above on the clean surface under UHV. It is clear that when carbon is adsorbed on the surface, no shift is observed, meaning that the SPV cannot be measured or is reduced to zero. Even though we applied a thorough procedure to remove CO_2 from water before injecting it into the reaction chamber, we could not avoid the introduction of CO_2 as well. Therefore, one should be careful when measuring time-resolved XPS in NAP conditions as the sample could easily be contaminated and the measured charge carriers dynamics turn out to be misleading.

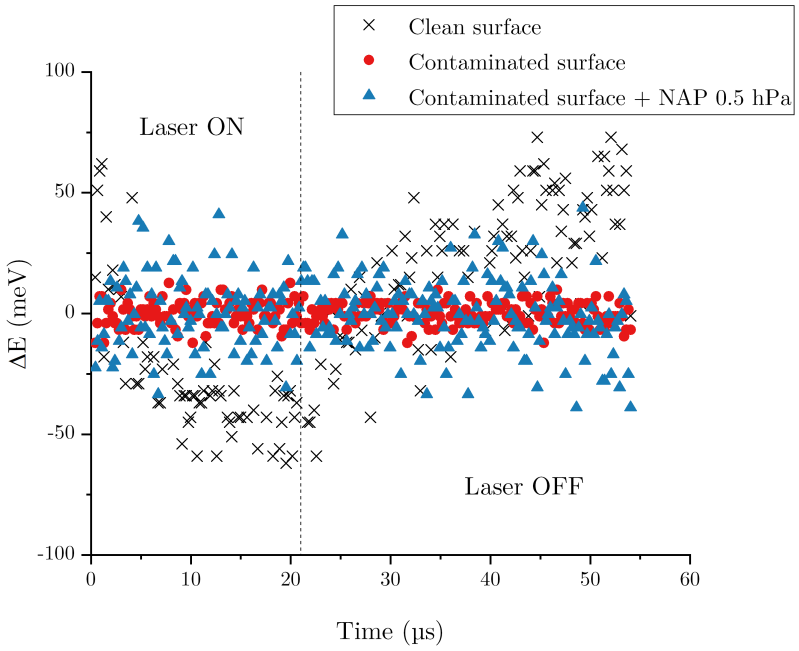

Figure 5.9 – Kinetic energy shift of the O 1s core level in Ti:Fe_2O_3 for the clean surface in UHV (black crosses), the surface contaminated by carbon species in UHV (red circles) and the surface contaminated by carbon species in NAP under exposition to 0.5 hPa (blue triangles).

5.2.4.2.2 On a contamination-free surface

In order to overcome the issues related to the carbon contamination in NAP conditions discussed above, it was decided to acquire time-resolved XPS spectra for 20 minutes on different regions of the sample, thus preventing the formation of a carbonated layer. The data were eventually summed up to reach a reasonable statistic allowing to obtain exploitable data. TR-PES experiments in NAP conditions could only be performed on Fe_2O_3 because of time limitation on the synchrotron beamline. The sample was first exposed to 0.02 hPa

of water and time-resolved XPS spectra were recorded during the exposition using the same laser parameters than above. The results are presented on Figure 5.10. As previously, the laser was switched on at 0 μs and off at 22 μs. The characteristic lifetime and total SPV are gathered in Table 5.3.

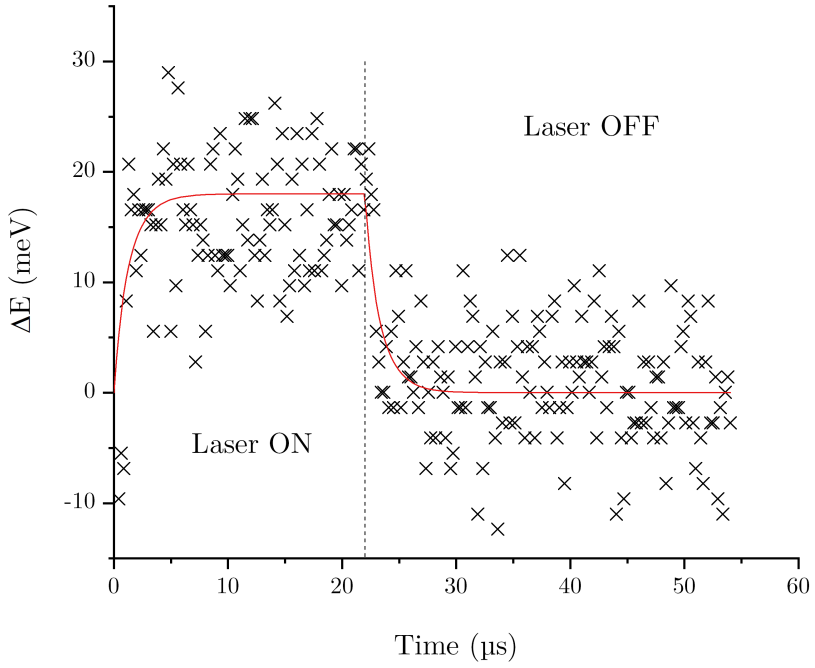

Figure 5.10 – Kinetic energy shift of the O 1s core level in Fe_2O_3 recorded with a photon energy of 830 eV in NAP conduction at a water pressure of 0.02 hPa.

	Onset	Decay
τ_∞ (μs)	1.5	1.5
ΔV_{SP}^{tot}	18	18

Table 5.3 – Characteristic lifetimes of the SPV in Fe_2O_3 in NAP conditions under 0.02 hPa of water.

Surprisingly, in these conditions, the laser induced O 1s shift is of opposite direction compared to the one in UHV. Indeed, when hematite is exposed to water, the laser induces a shift of the O 1s peak towards higher kinetic energies, meaning that electrons are now driven towards the surface. This behavior is usually typical of p-type semiconductors. Therefore, this result tends to indicate that hematite behaves completely differently under vacuum and in contact with water. Very recently, Rietwyk *et al.* published a study of the work function of 18 different metal oxides exposed to air [152]. They evidenced a decrease of the work function and an accumulation of electrons at the surface in all metal oxides after being exposed to air for several days. This electron accumulation can be viewed as a reduction of n-type

doping or even as a p-type doping as observed in our experiment. They directly associate this phenomenon to the water layer that forms on the oxide surface when in contact with air. Indeed, according to the authors, electronic charge transfer arises from the water layer to the oxide surface which induces a downward band bending, and thus p-type doping. One should thus be very careful when investigating hematite in UHV and drawing conclusions which could turn out to be far from accurate in kind of *operando* conditions. When hematite is exposed to water, the SPV is much smaller (18 meV) while the dark carrier lifetime and SPV onset time are both decreased to 1.5 μs. This experiment was reproduced two times and the same results were obtained, as shown on Figure 5.11b.

The water pressure was further increased to 1 hPa. The O 1s core level shift was measured in the above mentioned conditions. The results are displayed on Figure 5.11 alongside with the ones under 0.02 hPa of water for comparison. The increase of the water pressure produces a highly noisy signal (Figure 5.11a), even though one could potentially see a shift with similar characteristics than at 0.02 hPa, this signal can not be fitted because of the noise. To evidence this shift, the average of the O 1s position while the laser was on and off was calculated. The results are shown on Figure 5.11b. The reproducibility of the experiment under water pressure of 0.02 hPa is shown as well. Interestingly, it can be seen that the simple calculation of these averages allows to evidence a similar SPV shift at 1 hPa than at 0.02 hPa.

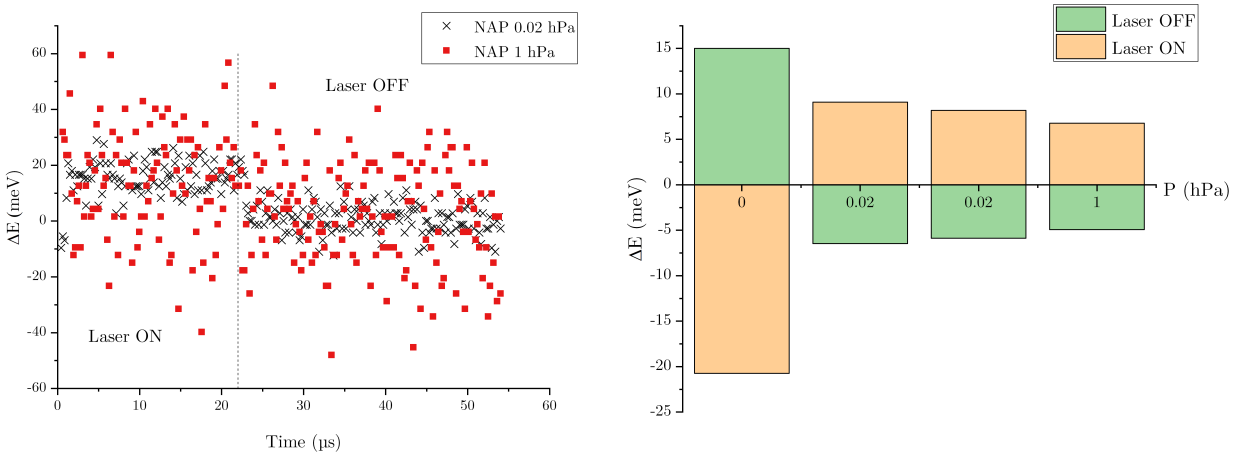

(a) (b)

Figure 5.11 – (a) Kinetic energy shift of the O 1s core level in Fe_2O_3 recorded with a photon energy of 830 eV in NAP conditions at a water pressure of 0.02 hPa (black crosses) and 1 hPa (red squares). (b) Average of the recorded O 1s core level shifts with laser ON (orange) and OFF (green) as a function of the water pressure.

5.3 Outline

The influence of upward and downward polarization in $BaTiO_3$ thin film on the charge carrier dynamics was investigated by TR-PES. In both cases, an O 1*s* laser-induced shift towards higher kinetic energies is observed. While such a shift is usually attributed to downward band bending, we think that here it can be the signature of photoconduction. Therefore, the measured O 1*s* core level shift is not only related to the electron-hole pairs created by the laser but also to the charges induced by the synchrotron excitation. The upward polarized sample favors electron extraction during the photoemission process and hence increases the SPV. It was also envisaged to study the influence of water adsorption on the charge dynamics but it turned out that water is not stable under the synchrotron beam in UHV. Such a study should be performed in NAP to allow to reach a stationary state.

Water adsorption was studied on Fe_2O_3 and Ti:Fe_2O_3 in NAP conditions. The results showed that, in both cases, water is first dissociated on the surface to form OH^- groups. The hydroxylation rate seems higher on the pure hematite than on the Ti-doped hematite sample. After hydroxylation of the surface, molecular water starts to adsorb. Again, water adsorption seems more favorable on Fe_2O_3 than on Ti:Fe_2O_3. This behavior might be explained by a lower affinity of the Ti cation than the Fe cation towards water adsorption. DFT calculations could be performed to better understand this phenomenon.

We showed that in NAP conditions the amount of OH^- groups and H_2O molecules adsorbed on the surface is not modified by the synchrotron beam nor by the laser. This indicates that the system is probably in a stationary state, thus showing that NAP allows to measure charge carrier dynamics in hematite while exposed to water.

Charge carriers dynamics were then measured on both samples under vacuum by means of time-resolved XPS. An increase of the SPV, and hence the upward band bending, was observed when hematite is doped with 2 at.% of Ti. The SPV is indeed higher in Ti:Fe_2O_3 (110 meV) than in Fe_2O_3 (95 meV). Both samples exhibit a typical *n*-type semiconductor behavior, with holes moving towards the surface because of upward band bending induced by the surface depletion layer. The dark carrier lifetime was measured in both samples at 25 μs while the onset time was 20 μs.

TR-PES was also performed on Fe_2O_3 while exposed to water in NAP. The first important observation is that the synchrotron radiation induces a reaction of carbon dioxide traces, introduced with water, on the surface of the sample, leading to the adsorption of a rather important carbon contamination layer. This layer completely modifies the behavior of the surface as no SPV can be recorded in such conditions. When a careful procedure is followed

to avoid carbon contamination during water exposition, characteristic lifetimes and SPV can be measured. Surprisingly, when hematite is exposed to water, the SPV shift is of opposite direction than when the surface is under vacuum. When water is adsorbed on hematite, upon laser excitation, the O 1s core level shifts towards higher kinetic energies, indicating that hematite now behaves like a p-type semiconductor. The SPV is much smaller (18 meV) and both dark carrier lifetime and onset time are much faster (1.5 μs).

Chapter 6

Conclusion

This thesis aimed at studying ferroelectric $BaTiO_3$, with an out-of-plane polarization, in the framework of solar water splitting because the internal electric field could favor charge carrier separation and thus reduce their recombination rate. As the band gap of ferroelectric materials (3.2 eV for BTO) is a limiting factor for their efficiency as a photoanode, they could be implemented in a heterojunction with more suited materials, such as hematite. Nevertheless, before studying such heterojunction, it is mandatory to completely understand the behavior of the ferroelectric system itself. For this purpose, first principle calculations based on the density functional theory were performed. They were completed with experimental characterizations, mainly synchrotron radiation based techniques.

By means of DFT calculations, the $Pt(001)/BaTiO_3(001)$ was first unraveled in chapter 3. We showed that the growth of BTO starts with a TiO_2 layer with Ti atoms located on the hollow sites of Pt. Additionally, the calculations indicated that TiO_2 and BaO surface terminations present a similar stability, and thus should both be considered. Then, the influence of the platinum substrate on the overlayer polarization was investigated. The substrate increases the stability of the ferroelectric phase compared to the paraelectric one and lowers the critical thickness required for the apparition of the ferroelectric phase. Indeed, ferroelectricity is observed from 9 layers when BTO is deposited on Pt while 11 layers are required for isolated BTO. Calculations also showed that Pt favors the stabilization of larger polarization domains.

Experimentally, we showed that OA-MBE is a suitable technique to prepare BTO samples with a controlled surface termination as BaO and TiO_2-terminated BTO samples were elaborated. Low energy photoemission appeared as a useful method to characterize the thin film surface. Indeed, the Ba $4d$ core level exhibits a splitting into two components which are respectively related to the volume and surface region of the sample. Interestingly, our results suggest that a splitting of the Ba $5s$ peak arises when the sample presents a BaO termination

only. This feature could therefore be used as a gauge to determine the surface termination of a BTO thin film.

To improve the efficiency of BTO as a photoanode for solar water splitting, it is important to understand its behavior towards water adsorption. To this end, DFT calculations were conducted to describe the interaction of H_2O with out-of-plane polarized BTO. The results are presented in chapter 4. They showed that the nature of the BTO surface termination has a significant influence on water adsorption. Indeed, water is seen to spontaneously dissociate on the BaO termination while the TiO_2 termination favors molecular adsorption. However, the rather small activation energy required to promote dissociation on the TiO_2 termination (0.13 eV) hints that dissociation could happen immediately at ambient temperature. Moreover, water adsorption also has an impact on the polarization of BTO. When water is adsorbed on the BaO termination, the resulting polarization systematically has a downward direction. The opposite is observed on the TiO_2 termination as water stabilizes the upward polarization. This important result suggests that water could switch the polarization direction in BTO depending on the surface termination. Therefore, the polarization direction in BTO thin films, and thus the charge transfer dynamics, could be controlled by tuning the film termination and its chemical environment.

Water adsorption on BTO was studied from an experimental point of view as well. The measurements showed that the BaO-terminated surface is more easily hydroxylated than the TiO_2-terminated one, in agreement with calculations.

Finally, in chapter 5, time-resolved XPS experiments were conducted on BTO and hematite. Regarding BTO, the aim was to examine the influence of the polarization on the charge dynamics. We showed that, in our experiment, the O $1s$ core level shift is probably dominated by photoconduction.

Concerning hematite, time-resolved XPS experiments could be performed in near ambient pressure conditions. Therefore, the samples were first analyzed under increasing water pressure. We demonstrated that water adsorption is more favorable on pure Fe_2O_3 than on Ti doped Fe_2O_3. It could be interesting to study such surfaces by means of DFT calculations to determine the influence of a Ti atom on the surface on the surrounding Fe atoms towards water adsorption. Yet, such calculations involving rather low doping rates are demanding from a computational point of view as they require to use large simulation slabs to decrease the dopant concentration. We also showed that NAP conditions allow to probe the hematite surface with adsorbed water on long time scale which is not the case in UHV conditions due to synchrotron beam induced desorption. TR-PES experiments performed in UHV showed that Ti doping induces an increase of the SPV which is the consequence of an increase of the

band bending. Both studied hematite samples exhibited a n-type semiconductor behavior as in both cases holes are driven towards the surface of the sample. Surprisingly, when the Fe_2O_3 sample was exposed to water in NAP conditions, the charge dynamics were completely modified. In this case, hematite behaved like a p-type semiconductor with a downward band bending. This phenomenon could arise from electron transfer from adsorbed hydroxyl groups and water molecule into the surface of the sample inducing an electron accumulation and thus a reduction of n-type doping.

It could be interesting to confirm some important theoretical results with experiments. In particular, the water induced polarization switching should be investigated in more details. Though such an experiment is difficult to perform, one could imagine to study the polarization reversal in a perfectly characterized BTO thin film by means of PFM in a liquid environment. Additionally, the study of charge dynamics in BTO as a function of the polarization orientation while exposed to water can give a better understanding of the reactivity of BTO towards water splitting. To this end, TR-PES measurements should be performed in NAP conditions for both possible surface terminations as well as both polarization directions. This would also allow to shed more light on the supposed electronic transfer from water to the metal oxide.

Doping is an envisaged method to improve BTO efficiency as a photoanode, in particular by reducing its band gap. As previously mentioned, a 2 at.% Fe doping has already been shown to reduce the band gap of BTO to 2.8 eV [42]. A smart approach would be to first consider a wide range of dopants and determine their influence on the band gap of BTO using DFT calculations. Yang *et al.* performed a DFT study of transition metals co-doping of BTO [153]. Although their work does not seem to include GGA+U correction, as it would be necessary for a thorough band gap investigation, it allows to give trends. They concluded that V-Cr co-doping significantly decreases the band gap of BTO.

Another interesting path to continue this work could be to investigate heterojunctions between BTO and other metal oxides such as hematite or TiO_2. Indeed, hematite presents a more suitable band gap than BTO for solar water splitting. The hematite layer could thus allow to create more electron-hole pairs while the polarization in BTO could drive the charge separation in the catalyst. The electronic properties and reactivity towards water adsorption could first be investigated by DFT calculations.

Bibliography

[1] N. S. Lewis and D. G. Nocera, Proc. Natl. Acad. Sci. **103**, 15729 (2006).

[2] P. C. K. Vesborg and T. F. Jaramillo, RSC Adv. **2**, 7933 (2012).

[3] United Nations Development Programme, *Am. J. Public Health*, Tech. Rep. (2001).

[4] A. Cho, Science **329**, 786 (2010).

[5] L. Carrette, K. A. Friedrich, and U. Stimming, Fuel Cells **1**, 5 (2001).

[6] B. Ewan and R. Allen, Int. J. Hydrogen Energy **30**, 809 (2005).

[7] K. Sivula, J. Phys. Chem. Lett. **6**, 975 (2015).

[8] IEA, *CO2 Capture Storage A Key Carbon Abat. Option*, Tech. Rep. (2008).

[9] R. Soltani, M. Rosen, and I. Dincer, Int. J. Hydrogen Energy **39**, 20266 (2014).

[10] I. Cerri, F. Lefebvre-Joud, P. Holtappels, K. Honegger, T. Stubos, and P. Millet, *Scientific Assessment in support of the Materials Roadmap enabling Low Carbon Energy Technologies: Hydrogen and Fuel Cells*, Tech. Rep. (European Commission, 2012).

[11] A. Fujishima and K. Honda, Nature **238**, 37 (1972).

[12] R. van de Krol, Y. Liang, and J. Schoonman, J. Mater. Chem. **18**, 2311 (2008).

[13] K. Maeda, K. Teramura, D. Lu, T. Takata, N. Saito, Y. Inoue, and K. Domen, Nature **440**, 295 (2006).

[14] S. Y. Reece, J. A. Hamel, K. Sung, T. D. Jarvi, A. J. Esswein, J. J. H. Pijpers, and D. G. Nocera, Science **334**, 645 (2011).

[15] H. Yoneyama, H. Sakamoto, and H. Tamura, Electrochim. Acta **20**, 341 (1975).

[16] P. Bornoz, F. F. Abdi, S. D. Tilley, B. Dam, R. van de Krol, M. Graetzel, and K. Sivula, J. Phys. Chem. C **118**, 16959 (2014).

[17] M. S. Prévot and K. Sivula, J. Phys. Chem. C **117**, 17879 (2013).

[18] J. W. Ager, M. R. Shaner, K. A. Walczak, I. D. Sharp, and S. Ardo, Energy Environ. Sci. **8**, 2811 (2015).

[19] K. Zhang, M. Ma, P. Li, D. H. Wang, and J. H. Park, Adv. Energy Mater. **6**, 1600602 (2016).

[20] R. Memming, *Semiconductor Electrochemistry* (Wiley-VCH Verlag GmbH & Co. KGaA, Weinheim, Germany, 2015).

[21] M. Rioult, *Hematite-based epitaxial thin lms as photoanodes for solar water splitting*, Ph.D. thesis (2015).

[22] F. Le Formal, *On the Morphology and Interfaces of Nanostructured Hematite Photoanodes for Solar-Driven Water Splitting*, Ph.D. thesis (2011).

[23] P. Cendula, S. D. Tilley, S. Gimenez, J. Bisquert, M. Schmid, M. Grätzel, and J. O. Schumacher, J. Phys. Chem. C **118**, 29599 (2014).

[24] Z. Zhang and J. T. Yates, Chem. Rev. **112**, 5520 (2012).

[25] K. Sivula, F. Le Formal, and M. Grätzel, ChemSusChem **4**, 432 (2011).

[26] M. P. Dare-Edwards, J. B. Goodenough, A. Hamnett, and P. R. Trevellick, J. Chem. Soc. Faraday Trans. 1 Phys. Chem. Condens. Phases **79**, 2027 (1983).

[27] M. F. Weber, J. Electrochem. Soc. **131**, 1258 (1984).

[28] M. G. Walter, E. L. Warren, J. R. McKone, S. W. Boettcher, Q. Mi, E. A. Santori, and N. S. Lewis, Chem. Rev. **110**, 6446 (2010).

[29] Y. Xu and M. A. Schoonen, Am. Mineral. **85**, 543 (2000).

[30] T. Bak, J. Nowotny, M. Rekas, and C. Sorrell, Int. J. Hydrogen Energy **27**, 991 (2002).

[31] K. Sivula, Chim. Int. J. Chem. **67**, 155 (2013).

[32] J. R. Bolton, S. J. Strickler, and J. S. Connolly, Nature **316**, 495 (1985).

[33] J. A. Glasscock, P. R. F. Barnes, I. C. Plumb, and N. Savvides, J. Phys. Chem. C **111**, 16477 (2007).

[34] B. Zhao, T. C. Kaspar, T. C. Droubay, J. McCloy, M. E. Bowden, V. Shutthanandan, S. M. Heald, and S. A. Chambers, Phys. Rev. B **84**, 245325 (2011).

[35] H. Magnan, D. Stanescu, M. Rioult, E. Fonda, and A. Barbier, Appl. Phys. Lett. **101**, 133908 (2012).

[36] J. Deng, J. Zhong, A. Pu, D. Zhang, M. Li, X. Sun, and S.-T. Lee, J. Appl. Phys. **112**, 084312 (2012).

[37] M. Rioult, H. Magnan, D. Stanescu, and A. Barbier, J. Phys. Chem. C **118**, 3007 (2014).

[38] Q. Zhu, C. Yu, and X. Zhang, J. Energy Chem. **35**, 30 (2019).

[39] A. Kleiman-Shwarsctein, Y.-S. Hu, A. J. Forman, G. D. Stucky, and E. W. McFarland, J. Phys. Chem. C **112**, 15900 (2008).

[40] I. Cesar, K. Sivula, A. Kay, R. Zboril, and M. Grätzel, J. Phys. Chem. C **113**, 772 (2009).

[41] Y. Lin, Y. Xu, M. T. Mayer, Z. I. Simpson, G. McMahon, S. Zhou, and D. Wang, J. Am. Chem. Soc. **134**, 5508 (2012).

[42] S. Upadhyay, J. Shrivastava, A. Solanki, S. Choudhary, V. Sharma, P. Kumar, N. Singh, V. R. Satsangi, R. Shrivastav, U. V. Waghmare, and S. Dass, J. Phys. Chem. C **115**, 24373 (2011).

[43] N. Artrith, W. Sailuam, S. Limpijumnong, and A. M. Kolpak, Phys. Chem. Chem. Phys. **18**, 29561 (2016).

[44] K. Maeda, ACS Appl. Mater. Interfaces **6**, 2167 (2014).

[45] S. Nishioka and K. Maeda, RSC Adv. **5**, 100123 (2015).

[46] P. Xie, F. Yang, R. Li, C. Ai, C. Lin, and S. Lin, Int. J. Hydrogen Energy **44**, 11695 (2019).

[47] J. P. Zou, L. Z. Zhang, S. L. Luo, L. H. Leng, X. B. Luo, M. J. Zhang, Y. Luo, and G. C. Guo, Int. J. Hydrogen Energy **37**, 17068 (2012).

[48] J. Cao, Y. Ji, C. Tian, and Z. Yi, J. Alloys Compd. **615**, 243 (2014).

[49] H.-P. Wang, K. Sun, S. Y. Noh, A. Kargar, M.-L. Tsai, M.-Y. Huang, D. Wang, and J.-H. He, Nano Lett. **15**, 2817 (2015).

[50] Z. Liu and L. Yan, Phys. Chem. Chem. Phys. **18**, 31230 (2016).

[51] E. S. Kim, N. Nishimura, G. Magesh, J. Y. Kim, J.-W. Jang, H. Jun, J. Kubota, K. Domen, and J. S. Lee, J. Am. Chem. Soc. **135**, 5375 (2013).

[52] S. J. Hong, S. Lee, J. S. Jang, and J. S. Lee, Energy Environ. Sci. **4**, 1781 (2011).

[53] J. Su, L. Guo, N. Bao, and C. A. Grimes, Nano Lett. **11**, 1928 (2011).

[54] J. Li, F. Meng, S. Suri, W. Ding, F. Huang, and N. Wu, Chem. Commun. **48**, 8213 (2012).

[55] L. Peng, T. Xie, Y. Lu, H. Fan, and D. Wang, Phys. Chem. Chem. Phys. **12**, 8033 (2010).

[56] H. Zhao, W. Fu, H. Yang, Y. Xu, W. Zhao, Y. Zhang, H. Chen, Q. Jing, X. Qi, J. Cao, X. Zhou, and Y. Li, Appl. Surf. Sci. **257**, 8778 (2011).

[57] M. Qin, K. Yao, and Y. C. Liang, Appl. Phys. Lett. **93**, 1 (2008).

[58] I. Grinberg, D. V. West, M. Torres, G. Gou, D. M. Stein, L. Wu, G. Chen, E. M. Gallo, A. R. Akbashev, P. K. Davies, J. E. Spanier, and A. M. Rappe, Nature **503**, 509 (2013).

[59] Y. Yuan, Z. Xiao, B. Yang, and J. Huang, J. Mater. Chem. A **2**, 6027 (2014).

[60] L. Li, P. A. Salvador, and G. S. Rohrer, Nanoscale **6**, 24 (2014).

[61] D. Tiwari and S. Dunn, J. Mater. Sci. **44**, 5063 (2009).

[62] C. R. Bowen, H. A. Kim, P. M. Weaver, and S. Dunn, Energy Environ. Sci. **7**, 25 (2014).

[63] A. Kakekhani, S. Ismail-Beigi, and E. I. Altman, Surf. Sci. **650**, 302 (2016).

[64] J. L. Giocondi and G. S. Rohrer, Chem. Mater. **13**, 241 (2001).

[65] J. L. Giocondi and G. S. Rohrer, J. Phys. Chem. B **105**, 8275 (2001).

[66] N. V. Burbure, P. A. Salvador, and G. S. Rohrer, J. Am. Ceram. Soc. **89**, 2943 (2006).

[67] N. V. Burbure, P. A. Salvador, and G. S. Rohrer, Chem. Mater. **22**, 5831 (2010).

[68] K. J. Choi, Science **306**, 1005 (2004).

[69] J. Junquera and P. Ghosez, Nature **422**, 506 (2003).

[70] N. Sai, A. M. Kolpak, and A. M. Rappe, Phys. Rev. B **72**, 020101 (2005).

[71] M. Stengel, D. Vanderbilt, and N. A. Spaldin, Nat. Mater. **8**, 392 (2009).

[72] G. Gerra, A. K. Tagantsev, N. Setter, and K. Parlinski, Phys. Rev. Lett. **96**, 107603 (2006).

[73] Q. Yang, J. X. Cao, Y. Ma, Y. C. Zhou, X. J. Lou, and J. Yang, J. Appl. Phys. **114**, 034109 (2013).

[74] S. V. Kalinin and D. A. Bonnell, J. Appl. Phys. **87**, 3950 (2000).

[75] S. V. Kalinin and D. A. Bonnell, Phys. Rev. B **63**, 125411 (2001).

[76] S. V. Kalinin and D. A. Bonnell, Nano Lett. **4**, 555 (2004).

[77] D. D. Fong, A. M. Kolpak, J. A. Eastman, S. K. Streiffer, P. H. Fuoss, G. B. Stephenson, C. Thompson, D. M. Kim, K. J. Choi, C. B. Eom, I. Grinberg, and A. M. Rappe, Phys. Rev. Lett. **96**, 127601 (2006).

[78] R. V. Wang, D. D. Fong, F. Jiang, M. J. Highland, P. H. Fuoss, C. Thompson, A. M. Kolpak, J. A. Eastman, S. K. Streiffer, A. M. Rappe, and G. B. Stephenson, Phys. Rev. Lett. **102**, 047601 (2009).

[79] M. J. Highland, T. T. Fister, M.-I. Richard, D. D. Fong, P. H. Fuoss, C. Thompson, J. A. Eastman, S. K. Streiffer, and G. B. Stephenson, Phys. Rev. Lett. **105**, 167601 (2010).

[80] M. J. Highland, T. T. Fister, D. D. Fong, P. H. Fuoss, C. Thompson, J. A. Eastman, S. K. Streiffer, and G. B. Stephenson, Phys. Rev. Lett. **107**, 187602 (2011).

[81] G. B. Stephenson and M. J. Highland, Phys. Rev. B **84**, 064107 (2011).

[82] J. L. Wang, F. Gaillard, A. Pancotti, B. Gautier, G. Niu, B. Vilquin, V. Pillard, G. L. Rodrigues, and N. Barrett, J. Phys. Chem. C **116**, 21802 (2012).

[83] Y. Mi, G. Geneste, J. E. Rault, C. Mathieu, A. Pancotti, and N. Barrett, J. Phys. Condens. Matter **24**, 275901 (2012).

[84] L. He and D. Vanderbilt, Phys. Rev. B **68**, 134103 (2003).

[85] T. Kolodiazhnyi, M. Tachibana, H. Kawaji, J. Hwang, and E. Takayama-Muromachi, Phys. Rev. Lett. **104**, 1 (2010).

[86] B. Matthias and A. von Hippel, Phys. Rev. **73**, 1378 (1948).

[87] J. P. W. Forsbergh, Phys. Rev. **76**, 1187 (1949).

[88] S. K. Streiffer, J. A. Eastman, D. D. Fong, C. Thompson, A. Munkholm, M. V. Ramana Murty, O. Auciello, G. R. Bai, and G. B. Stephenson, Phys. Rev. Lett. **89**, 1 (2002).

[89] D. D. Fong, G. B. Stephenson, S. K. Streiffer, J. A. Eastman, O. Aucielo, P. H. Fuoss, and C. Thompson, Science **304**, 1650 (2004).

[90] R. Takahashi, Ø. Dahl, E. Eberg, J. K. Grepstad, and T. Tybell, J. Appl. Phys. **104**, 064109 (2008).

[91] I. Kornev, H. Fu, and L. Bellaiche, Phys. Rev. Lett. **93**, 196104 (2004).

[92] C.-G. Duan, R. F. Sabirianov, W.-N. Mei, S. S. Jaswal, and E. Y. Tsymbal, Nano Lett. **6**, 483 (2006).

[93] P. Aguado-Puente and J. Junquera, Phys. Rev. Lett. **100**, 177601 (2008).

[94] P. Hohenberg and W. Kohn, Phys. Rev. **136**, B864 (1964).

[95] W. Kohn and L. J. Sham, Phys. Rev. **140**, A1133 (1965).

[96] J. P. Perdew, K. Burke, and M. Ernzerhof, Phys. Rev. Lett. **77**, 3865 (1996).

[97] S. L. Dudarev, G. A. Botton, S. Y. Savrasov, C. J. Humphreys, and A. P. Sutton, Phys. Rev. B **57**, 1505 (1998).

[98] S. Grimme, Wiley Interdiscip. Rev. Comput. Mol. Sci. **1**, 211 (2011).

[99] S. Grimme, J. Antony, S. Ehrlich, and H. Krieg, J. Chem. Phys. **132**, 154104 (2010).

[100] G. Kresse and J. Furthmüller, Phys. Rev. B **54**, 11169 (1996).

[101] G. Kresse and J. Furthmüller, Comput. Mater. Sci. **6**, 15 (1996).

[102] J. D. Pack and H. J. Monkhorst, Phys. Rev. B **13**, 5188 (1977).

[103] P. E. Blöchl, Phys. Rev. B **50**, 17953 (1994).

[104] G. Kresse and D. Joubert, Phys. Rev. B **59**, 1758 (1999).

[105] M. Fechner, S. Ostanin, and I. Mertig, Phys. Rev. B **77**, 094112 (2008).

[106] B. Meyer and D. Vanderbilt, Phys. Rev. B **63**, 205426 (2001).

[107] M. Sepliarsky, M. G. Stachiotti, and R. L. Migoni, Phys. Rev. Lett. **96**, 1 (2006).

[108] T. Shimada, S. Tomoda, and T. Kitamura, Phys. Rev. B **81**, 144116 (2010).

[109] N. A. Spaldin, Science **304**, 1606 (2004).

[110] W. Zhong, R. D. King-Smith, and D. Vanderbilt, Phys. Rev. Lett. **72**, 3618 (1994).

[111] P. Ghosez, X. Gonze, and J. P. Michenaud, Ferroelectrics **164**, 113 (1995).

[112] SPECS, *PHOIBOS 150 N. Near Ambient Press. Hemispherical Energy Anal.*, Tech. Rep. (2010).

[113] N. Iles, K. Driss Khodja, A. Kellou, and P. Aubert, Comput. Mater. Sci. **87**, 123 (2014).

[114] D. I. Bilc, R. Orlando, R. Shaltaf, G.-M. Rignanese, J. Íñiguez, and P. Ghosez, Phys. Rev. B **77**, 165107 (2008).

[115] E. S. Goh, L. H. Ong, T. L. Yoon, and K. H. Chew, Comput. Mater. Sci. **117**, 306 (2016).

[116] R. A. Evarestov and A. V. Bandura, J. Comput. Chem. **33**, 1123 (2012).

[117] G. H. Kwei, A. C. Lawson, S. J. Billinge, and S. W. Cheong, J. Phys. Chem. **97**, 2368 (1993).

[118] Z. Wu, R. E. Cohen, and D. J. Singh, Phys. Rev. B **70**, 104112 (2004).

[119] S. H. Wemple, Phys. Rev. B **2**, 2679 (1970).

[120] M. V. Berry, Proc. R. Soc. A Math. Phys. Eng. Sci. **392**, 45 (1984).

[121] K. M. Rabe, C. H. Ahn, and J. M. Triscone, *Physics of Ferroelectrics A Modern Perspective*, Topics in Applied Physics, Vol. 105 (Springer Berlin Heidelberg, 2007).

[122] W. J. Merz, Phys. Rev. **91**, 513 (1953).

[123] H. H. Wieder, Phys. Rev. **99**, 1161 (1955).

[124] P. Gao, Z. Zhang, M. Li, R. Ishikawa, B. Feng, H.-J. Liu, Y.-L. Huang, N. Shibata, X. Ma, S. Chen, J. Zhang, K. Liu, E.-G. Wang, D. Yu, L. Liao, Y.-H. Chu, and Y. Ikuhara, Nat. Commun. **8**, 15549 (2017).

[125] J. Dionot, G. Geneste, C. Mathieu, and N. Barrett, Phys. Rev. B **90**, 014107 (2014).

[126] M. El-Kazzi, *Etude par photoemission (XPS et XPD) d'heterostructures d'oxydes fonction*, Ph.D. thesis, Ecole Centrale de Lyon (2007).

[127] L. T. Hudson, R. L. Kurtz, S. W. Robey, D. Temple, and R. L. Stockbauer, Phys. Rev. B **47**, 10832 (1993).

[128] S. M. Mukhopadhyay and T. C. Chen, J. Mater. Res. **10**, 1502 (1995).

[129] X. L. Li, B. Chen, H. Y. Jing, H. B. Lu, B. R. Zhao, Z. H. Mai, and Q. J. Jia, Appl. Phys. Lett. **87**, 1 (2005).

[130] A. Barbier, C. Mocuta, D. Stanescu, P. Jegou, N. Jedrecy, and H. Magnan, J. Appl. Phys. **112**, 114116 (2012).

[131] M. Rioult, S. Datta, D. Stanescu, S. Stanescu, R. Belkhou, F. Maccherozzi, H. Magnan, and A. Barbier, Appl. Phys. Lett. **107**, 103901 (2015).

[132] G. Geneste and B. Dkhil, Phys. Rev. B **79**, 235420 (2009).

[133] X. Li, B. Wang, T.-Y. Zhang, and Y. Su, J. Phys. Chem. C **118**, 15910 (2014).

[134] J. D. Baniecki, M. Ishii, K. Kurihara, K. Yamanaka, T. Yano, K. Shinozaki, T. Imada, and Y. Kobayashi, J. Appl. Phys. **106**, 054109 (2009).

[135] G. Henkelman, B. P. Uberuaga, and H. Jónsson, J. Chem. Phys. **113**, 9901 (2000).

[136] P. Pulay, Chem. Phys. Lett. **73**, 393 (1980).

[137] P.-M. Deleuze, A. Mahmoud, B. Domenichini, and C. Dupont, Phys. Chem. Chem. Phys. **21**, 4367 (2019).

[138] Y. Tian, L. Wei, Q. Zhang, H. Huang, Y. Zhang, H. Zhou, F. Ma, L. Gu, S. Meng, L.-Q. Chen, C.-W. Nan, and J. Zhang, Nat. Commun. **9**, 3809 (2018).

[139] S. Datta, M. Rioult, D. Stanescu, H. Magnan, and A. Barbier, Thin Solid Films **607**, 7 (2016).

[140] L. Chen, Z. Cheng, W. Xu, X. Meng, G. Yuan, J. Liu, and Z. Liu, Sci. Rep. **6**, 19092 (2016).

[141] Y. Ahn, H. W. Shin, and J. Y. Son, Thin Solid Films **649**, 142 (2018).

[142] M. Kohli and P. Muralt, Ferroelectrics **225**, 155 (1999).

[143] Y. W. So, D. J. Kim, T. W. Noh, J.-G. Yoon, and T. K. Song, Appl. Phys. Lett. **86**, 092905 (2005).

[144] A. B. Kounga, T. Granzow, E. Aulbach, M. Hinterstein, and J. Rödel, J. Appl. Phys. **104**, 024116 (2008).

[145] D. Cao, Z. Wang, Nasori, L. Wen, Y. Mi, and Y. Lei, Angew. Chemie Int. Ed. **53**, 11027 (2014).

[146] B. J. Rodriguez, S. Jesse, A. P. Baddorf, and S. V. Kalinin, Phys. Rev. Lett. **96**, 1 (2006).

[147] J. Linn and W. Swartz Jr, Appl. Surf. Sci. **20**, 154 (1984).

[148] V. Fuenzalida, M. Pilleux, and I. Eisele, Vacuum **55**, 81 (1999).

[149] B. F. Spencer, D. M. Graham, S. J. O. Hardman, E. A. Seddon, M. J. Cliffe, K. L. Syres, A. G. Thomas, S. K. Stubbs, F. Sirotti, M. G. Silly, P. F. Kirkham, A. R. Kumarasinghe, G. J. Hirst, A. J. Moss, S. F. Hill, D. A. Shaw, S. Chattopadhyay, and W. R. Flavell, Phys. Rev. B **88**, 195301 (2013).

[150] C. X. Kronawitter, L. Vayssieres, S. Shen, L. Guo, D. A. Wheeler, J. Z. Zhang, B. R. Antoun, and S. S. Mao, Energy Environ. Sci. **4**, 3889 (2011).

[151] S. C. Warren, K. Voïtchovsky, H. Dotan, C. M. Leroy, M. Cornuz, F. Stellacci, C. Hébert, A. Rothschild, and M. Grätzel, Nat. Mater. **12**, 842 (2013).

[152] K. J. Rietwyk, D. A. Keller, A. Ginsburg, H. Barad, M. Priel, K. Majhi, Z. Yan, S. Tirosh, A. Y. Anderson, L. Ley, and A. Zaban, Adv. Mater. Interfaces **6**, 1802058 (2019).

[153] F. Yang, L. Yang, C. Ai, P. Xie, S. Lin, C.-Z. Wang, and X. Lu, Nanomaterials **8**, 455 (2018).

Abstract

The properties of out-of-plane polarized $BaTiO_3$(001) thin films were investigated from first-principles calculations and photoemission spectroscopy. Firstly, density functional theory calculations (DFT) were used to unravel the nature of the Pt(001)/$BaTiO_3$(001) interface. In particular, the influence of the substrate on the ferroelectric properties of the $BaTiO_3$ overlayer has been studied. Among the results, it can be pointed that platinum tends to increase the ferroelectric domain size of $BaTiO_3$.

Then, the adsorption of water on $BaTiO_3$ was described by means of DFT calculations. The impact of the polarization as well as the influence of the nature of the surface termination on water adsorption were studied. Different adsorption processes depending on the chemical nature of the surface termination were evidenced. Additionally, water was shown to switch the polarization towards the upward direction on the TiO_2 termination while the downward polarization is stabilized in the BaO termination.

Finally, time-resolved photoemission spectroscopy was used to measure the charge dynamics of photogenerated electron-hole pairs in both $BaTiO_3$ and Fe_2O_3. Near ambient pressure conditions allowed to record the charge dynamics in hematite while exposed to water, revealing a significant modification of the band bending induced by water adsorption.

Keywords: *water splitting, ferroelectricity, $BaTiO_3$, heterojunction, DFT, TR-PES, NAP-XPS.*

Résumé

Les propriétés de films minces de $BaTiO_3$(001) polarisés hors-plan ont été étudiées à partir de calculs *ab initio* et par spectroscopie de photoélectrons. Tout d'abord, la théorie de la fonctionnelle de la densité (DFT) a été utilisée pour décrire la nature de l'interface Pt(001)/$BaTiO_3$(001). En particulier, l'influence du substrat sur les propriétés ferroélectriques du film de $BaTiO_3$ a été analysée. Parmi les résultats, il a été montré que le platine tend à accroître la taille des domaines ferroélectriques de $BaTiO_3$.

Ensuite, les mécanismes d'adsorption de l'eau sur $BaTiO_3$ ont été décrits par calculs DFT. L'impact de la polarisation ainsi que l'influence de la terminaison de surface sur l'adsorption de l'eau ont été analysés. Il a pu être montré que les processus d'adsorption dépendent directement de la nature de la terminaison. En outre, il a été observé que l'eau peut induire un renversement de la polarisation dont la direction finale dépend de la terminaison. En effet, l'eau stabilise la polarisation orientée vers le haut sur la terminaison TiO_2 alors qu'elle induit une polarisation orientée vers le bas sur la terminaison BaO.

Enfin, la dynamique de création et de recombinaison des charges photogénérées dans $BaTiO_3$ et Fe_2O_3 a été mesurée par spectroscopie de photoelectrons résolue temporellement. Des mesures dans des conditions de pression proches de l'ambiante ont notamment permis de mesurer la dynamique des charges dans l'hématite lorsque celle-ci est exposée à l'eau, révélant une importante modification de la courbure de bandes du fait de l'adsorption d'eau.

Mots-clés : *photo-électrolyse, ferroélectricité, $BaTiO_3$, hétérojonction, DFT, TR-PES, NAP-XPS.*